Interplay of spin and valley degrees of freedom

Tayfun Gokmen

A Dissertation
Presented to the Faculty
of Princeton University
in Candidacy for the Degree
of Doctor of Philosophy

Recommended for Acceptance
by the Department of
electrical engineering
Adviser: Prof. Mansour Shayegan

June 2010

Abstract

In this thesis, we explore the role of spin and valley degrees of freedom on physical properties of interacting two-dimensional electron systems (2DESs) confined to AlAs quantum wells. In addition to controlling the spin polarization via the application of magnetic field, in this system, we also change the conduction-band valley occupation via engineering the quantum well width and the application of strain.

Our measurements reveal that both spin and valley degrees of freedom play crucial roles in renormalizing the fundamental properties of the 2DES including the effective mass (m^*), the effective Lande g-factor (g^*) and the conduction-band deformation potential (E_2^*). For a partially spin/valley polarized system, m^* is larger than its band value, consistent with previous results on various 2DESs. However, for a fully spin and valley polarized system, m^* is unexpectedly suppressed and falls even below the band mass. Moreover, m^* measurements in the partially polarized regime reveal a marked contrast between the spin and valley degrees of freedom: When electrons occupy two spin subbands, m^* depends on the valley occupation, but not vice versa. Combining m^* data with the measured spin and valley susceptibilities, we find that the effective Lande g-factor strongly depends on valley occupation, but the renormalized conduction-band deformation potential is independent of the spin occupation.

We also study the role of valley degree of freedom and the band mass anisotropy on the properties of composite fermions, the emergent particles at high magnetic fields. Our measurements of the piezoresistance at zero magnetic field and at Landau level filling factors $\nu = 1/2$ and $3/2$ demonstrate that, qualitatively similar to their electron counterparts, the composite fermions in this system also possess a valley degree of freedom and an anisotropic Fermi surface.

Acknowledgments

It is difficult to overstate my gratitude to my advisor, Mansour, for his sound guidance and remarkable patience. I am grateful for his friendship, support and making me feel like at home during my years at Princeton. I will not only remember him as a perfect advisor but also as a good friend and one from the family with the picnics, thanksgiving dinners and soccer games.

Obviously, conducting experiments require collaboration with various people because not only it is impossible to do it alone, but also you need a savior when you are about to blow the lab. For my case she was Medini and she deserves special thanks for being such a good lab mate and friend. Almost all the projects I was involved in, Medini did half of the work. The former members of mashgroup, Oki and Kamran, have my gratitude for teaching me the basics to survive in the lab and the clean room. My heartfelt thanks are extended to the rest of the group members Nathan, Babur, Shashank, Javad, YenTing, Yang and Dobromir for their help at various occasions.

I am also thankful to Eric Palm, Tim Murphy, Ju-Hyun Park, Glover Jones, Scott Mayers and Bobby Pullum for all the help they provided during our measurements at the NHMFL, Florida. My gratitude extends to professors Stephen Lyon and Sigurd Wagner for reading this thesis and giving me useful comments; and to the people in E-Quad for all their contributions. Full thanks also to the National Science Foundation for their financial support.

I was lucky enough to have the support of many people who made my life at Princeton more enjoyable and manageable. Ismail has my gratitude for fixing my car whatever its condition is and for his friendship. I am thankful to all my friends at Sultans, GradFC, Princeton United, and Istanbulspor. I can not imagine how boring my life would have been without those soccer games including the ones on computer. I also want to express my gratitude to my sister (Meltem), parents (Hulya and Muhsin) and uncle (Ihsan). One way or another each one of them gave me courage and support in completing this journey. Not to be forgotten our dog Tommy was of course my star with his cheering memories.

Last but not least I am grateful to my wife, Selcen, for her companionship and love; for being crazy enough to leave her career and family in Turkey and move to USA for me; for her dedication to keep me in good shape with her home-cooked meals, advices and company even to Tallahassee (Magnet Lab) and March Meeting trips. Thanks a lot for taking care of everything so I could have some fun. I dedicate this thesis to her.

to Selcen

Contents

Abstract . . . iii

Acknowledgments . . . iv

Symbols used in this thesis . . . xiv

1 Introduction **1**

1.1 Effective mass renormalization . . . 3

1.2 Metal-insulator transition . . . 4

1.3 Electrons in a magnetic field . . . 7

1.3.1 Integer quantum Hall effect . . . 7

1.3.2 Fractional quantum Hall effect . . . 9

1.3.3 Composite fermions . . . 10

2 AlAs band structure and samples **12**

2.1 AlAs band structure . . . 12

2.2 AlAs quantum wells . . . 14

2.2.1 Controlling valley splitting in wide AlAs quantum wells . . . 16

2.3 Sample preparation and measurement set up . . . 18

3 Effective mass of 2D electrons in wide AlAs quantum wells **20**

3.1 Introduction . . . 20

3.2 Analysis methods 22

3.3 Determination of spin and valley phase diagram 23

3.4 Dependence of effective mass on spin and valley degrees of freedom . 27

3.4.1 Spin and valley phase diagram 27

3.4.2 Temperature dependence of Shubnikov de Haas oscillations . . 29

3.5 Density dependence of effective mass 34

4 Effective mass of 2D electrons in narrow AlAs quantum wells 37

4.1 Introduction 37

4.2 Temperature dependence of Shubnikov de Haas oscillations 38

4.3 Density dependence of effective mass 43

4.4 Comparison with 2D electrons in wide AlAs quantum wells 46

4.5 Discussion and Conclusions 48

5 Contrast between spin and valley degrees of freedom 50

5.1 Effective mass data 51

5.2 Effective g-factor and deformation potential data 53

6 Transference of transport anisotropy to composite fermions 58

6.1 Introduction 59

6.2 Transport along [100] 61

6.2.1 Magnetoresistance data 62

6.2.2 Piezoresistance at $\nu = 1/2$ 62

6.2.3 Piezoresistance at $\nu = 3/2$ 67

6.2.4 Discussion 72

6.3 Transport along [110] 75

6.3.1 Piezoresistance of M424J4 76

6.3.2 Piezoresistance of M415N2 79

6.3.3 Temperature dependence of piezoresistance at $\nu = 3/2$ 81

6.4 Summary 84

7 Summary and Future projects 86

7.1 Summary 86

7.2 Future projects 87

A Temperature dependence of resistance at different spin and valley polarizations 89

B Publications 93

B.1 Publications related to this thesis 93

B.2 Other publications 94

List of Figures

1.1 Sketch of the metal-insulator transition 5

1.2 Transport measurement setup 8

1.3 Schematic of electron and composite fermion Fermi surfaces 10

1.4 Schematic of quantum Hall states at $\nu = 1$ and $\nu = 1/3$ 11

2.1 Band structures of GaAs, Si and AlAs 13

2.2 Schematic of an AlAs quantum well 15

2.3 Fermi surfaces of AlAs valleys 16

2.4 Schematic of a sample on piezo 17

3.1 Spin and valley phase diagram for M424J4 24

3.2 Piezoresistance and magnetoresistance of M424J4 25

3.3 Spin and valley phase diagram of M409Q2 28

3.4 Piezoresistance and magnetoresistance for M409Q2 29

3.5 Temperature dependence of SdH data for s_1v_2 31

3.6 Temperature dependence of SdH data for s_1v_1, s_2v_1 and s_2v_2 33

3.7 Density dependence of m^* of 2DES in wide AlAs QWs 35

4.1 Magnetoresistance of partially spin polarized 2DES in narrow AlAs QWs at high density. 40

4.2 Magnetoresistance of fully spin polarized 2DES in narrow AlAs QWs at high density. 41
4.3 Magnetoresistance of partially spin polarized 2DES in narrow AlAs QWs at low density. 42
4.4 Magnetoresistance of fully spin polarized 2DES in narrow AlAs QWs at low density. 42
4.5 Dingle plots of the partially spin polarized 2DES in narrow AlAs QWs. 44
4.6 Density dependence of m^* of 2DES in narrow AlAs QWs. 45
4.7 Comparison of 2DES in narrow and wide AlAs QWs. 46

5.1 Summary of m^*, g^* and E_2^* 52

6.1 Schematics of 2D electrons and composite fermions in real and reciprocal space 61
6.2 Magnetoresistance of M424J4 63
6.3 Piezoresistance at $\nu = 1/2$ 64
6.4 Piezoresistance at $\nu = 1/2$ for several densities 66
6.5 Piezoresistance at $\nu = 3/2$ for several densities 68
6.6 Piezoresistance at $\nu = 3/2$ at high density 69
6.7 Piezoresistance at $\nu = 3/2$ at low density 71
6.8 Comparison of resistance ratios of electrons and CFs 73
6.9 Piezoresistance of M424J4 at $B = 0$, $\nu = 3/2$ and $\nu = 1/2$ 77
6.10 Magnetoresistance of M415N2 80
6.11 Piezoresistance of M415N2 at $B = 0$ and $\nu = 3/2$ 80
6.12 Temperature dependence of piezoresistance of electrons and CFs . . . 82
6.13 Temperature dependence of piezoresistance of electrons 83

A.1 The temperature dependence of resistance along 110 91

A.2 The temperature dependence of resistance along 100 92

List of Tables

Symbols used in this thesis

Expansion	abbreviation
Two-dimensional electron system	2DES
Metal oxide semiconductor field effect transistor	MOSFET
Molecular beam epitaxy	MBE
2D electron density	n
The interaction strength	r_s
Band effective mass	m_b
Renormalized effective mass	m^*
Metal Insulator Transition	MIT
Longitudinal resistance	R_{xx}, R
Transverse (or Hall) resistance	R_{xy}
Perpendicular magnetic field	B, $B_\perp$
Integer quantum Hall	IQH
Density of states	DOS
Landau level	LL
Cyclotron energy	$\hbar\omega_c$
Zeeman energy	E_Z
Electronic charge	e
Planck's constant	h, $\hbar$
Bohr magneton	μ_B
Landau level filling factor	ν
Fractional quantum Hall	FQH

Composite fermion	CF
CF filling factor	p
Quantum Well	QW
Conduction-band	CB
Valence-band	VB
Band effective Lande g-factor	g_b
Transverse band mass	m_t
Longitudinal band mass	m_l
Piezoelectric actuator	piezo
Valley with major axis along the growth direction	Z or [001] valley
Valley with major axis along the poling direction of the piezo	X or [100] valley
Valley with major axis perpendicular to the poling direction of the piezo	Y or [010] valley
Strain along [100] ([010]) direction	$\epsilon_{[100]}$ ($\epsilon_{[010]}$)
Strain, $\epsilon_{[100]} - \epsilon_{[010]}$	ϵ
Single particle valley splitting energy	E_V
Conduction-band deformation potential	E_2, $E_{2,b}$
Tilt angle	θ
Renormalized spin susceptibility	χ_s^*
Band spin susceptibility	$\chi_{s,b}$
Renormalized effective Lande g-factor	g^*
Temperature	T
Shubnikov de Haas	SdH

Strength of a SdH oscillation	ΔR
Background resistance near a SdH oscillation	R_o
Single-particle (quantum) lifetime	τ_q
Transport scattering time	τ_{tr}
Cyclotron frequency	ω_c
Parallel magnetic field	$B_\parallel$
Total magnetic field	B_{tot}
Fermi energy	E_F
Valley polarization	P_v
Spin polarization	P_s
Valley susceptibility	χ_v
Renormalized conduction-band deformation potential	E_2^*
Fermi surface	FS

Chapter 1

Introduction

Research on two-dimensional electron systems (2DESs) continues to attract both theorists and experimentalists because of the fascinating interplay between physical properties and dimensionality, and its connection to technologically useful devices. In a 2DES, electrons are free to move in two dimensions, but are confined in the third dimension. Most 2DESs are realized in either metal-oxide-semiconductor field effect transistors (MOSFETs) or at interfaces between different semiconductor materials. 2DESs confined to heterostructure interfaces have extremely high low-temperature mobilities thanks to the modulation-doping technique [1]. As the sample quality has improved with advances in semiconductor growth technologies, particularly molecular beam epitaxy (MBE), these ultra clean systems have revealed the effects of electron-electron interaction and have led to the observation of fascinating physical phenomena such as the fractional quantum Hall effect, electron Wigner crystallization, ferromagnetic ground states, etc. [2].

In the quantum mechanical description of a non-interacting, ideal 2DES at zero magnetic field, electrons have an energy dispersion which is quadratic with the in-plane wave vector and, depending on their density (n), electrons fill the lowest energy states up to the Fermi energy. While the Fermi energy is the main energy scale for a non-interacting system (at very low temperatures), the Coulomb energy becomes relevant with the introduction of interaction. The interaction strength is characterized by the parameter $r_s = 1/\sqrt{\pi n} a_B^*$ defined as the average inter-electron spacing measured in units of the effective Bohr radius (a_B^*) or, equivalently, the ratio of the Coulomb energy to the Fermi energy of a single-valley, spin unpolarized 2DES. Thanks to the tunability of the interaction strength over a wide range via simply varying the density, 2DESs provide a particularly fertile ground to study the effects of electron-electron interaction.

In this thesis, we study the electron-electron interaction in a novel system where electrons are confined to quantum wells made of AlAs. For this system, we can reach r_s values up to 20 where the interaction dominates the physics. Bulk AlAs is a multi-valley semiconductor. However, the degeneracy of the valleys are lifted in our heterostructures as we describe in section 2.2. This gives us the freedom to choose the number of valleys occupied and the shape (anisotropy) of the Fermi surface (more precisely, the Fermi contour) at zero magnetic field. We explore the effects of the valley degree of freedom and the shape of the Fermi surface on several interaction-driven phenomena such as effective mass renormalization, metal-insulator transition and the composite fermion Fermi surface.

In the remainder of this Chapter, we introduce several basic concepts that are useful for the discussion and understanding of the results we present in this thesis.

1.1 Effective mass renormalization

The most successful theory that explains the behavior of electrons in solids is the band theory. In a crystalline solid electrons feel a periodic potential. This potential gives rise to ranges of energy that an electron is "forbidden" or "allowed" to have. The range of allowed energies is called a band and each band has certain energy dispersion as a function of the wave vector. Wherever a minimum occurs in the dispersion relation, it can often be approximated by a quadratic curve in the small region around that minimum. Within this so-called effective mass approximation, electrons behave in many respects as if they were free, but with a mass related to the curvature of the energy dispersion around that minimum. This mass is the band "effective" mass (m_b) of an electron in a solid; it is a fundamental property of the solid, and differs from material to material. We also note that the curvature of the energy dispersion might not be the same along different directions, resulting in a direction-dependent effective mass.

The band theory and the effective mass approximation typically do not take the interaction into account. However, as we mentioned above, the strength of the Coulomb interaction can be many times larger than the Fermi energy in 2DESs. For these highly interacting systems, Landau's Fermi liquid theory becomes handy. Fermi liquid is a generic term for a quantum mechanical liquid of fermions that arises under certain physical conditions when the temperature is sufficiently low. The interaction between the particles of the many-body system does not necessarily need to be small for Fermi liquid theory to be valid. The system's dynamics and thermodynamics at low excitation energies and temperatures may be described by substituting the highly interacting electrons with the non-interacting fermions, the so-called quasiparticles, each of which carries the same spin, charge and momentum as the original particles. In a Fermi liquid, thermodynamical quantities such as specific heat, compressibility, spin-susceptibility, etc. show the same qualitative behavior as in the non-interacting electron gas, but their magnitudes are renormalized because of the interaction. Similarly, the effective mass of the quasiparticles is different from the effective mass of the original particles, and therefore this new mass is referred to as interaction renormalized effective mass (m^*). The renormalized values of these physical quantities are of great interest both theoretically and experimentally, since they give information regarding the details of the interaction. A detailed description of Landau's Fermi liquid theory can be found in Ref. [3].

1.2 Metal-insulator transition

Materials can be classified as metal or insulator according to their electrical transport properties. Strictly speaking the distinction between metal and insulator is meaningful only at zero temperature. At zero temperature, metals have a finite DC conductivity (σ), whereas for insulators conductivity is zero. In the microscopic picture of an insulator, the charge carriers have to overcome some energy gap to contribute to conduction, giving an exponentially suppressed conductivity at lower temperatures. However, in metals charge carriers contribute to conduction by scattering to the available states at the Fermi energy without overcoming an energy gap, giving a weak temperature dependence for conductivity. In metals, increasing temperature causes more scattering; therefore conductivity decreases with increasing temperature. Since the absolute zero is not achievable experimentally, the distinction between a metal and an insulator is often made at low but finite temperatures by

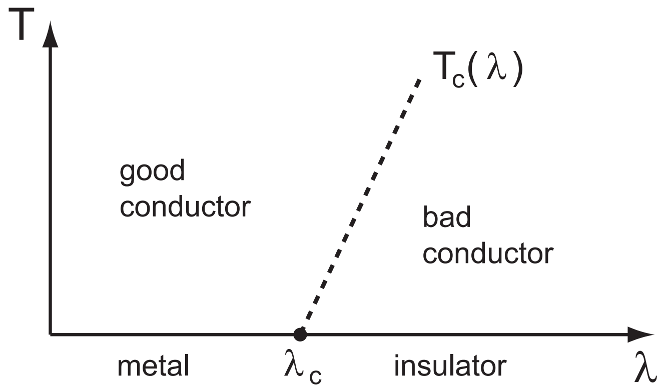

Figure 1.1: Sketch of the metal-insulator transition.

assuming that $\partial\sigma/\partial T > 0$ means a metal and $\partial\sigma/\partial T < 0$ an insulator. We use this as the definition of metal and insulator throughout the thesis.

A system's behavior as a metal or an insulator is a ground state property; the transition between them defines a quantum phase transition and is of fundamental importance. Contrary to classical phase transitions, quantum phase transitions can only be accessed by varying a physical parameter, λ, at zero temperature. In the case of metal-insulator transition (MIT) this λ can be the strength of disorder, electron-electron interaction or any parameter which affects the Hamiltonian of the system, such as magnetic field, pressure, etc. A sketch of the MIT in a temperature vs. λ phase diagram is shown in Fig. 1.1.

Metal-insulator transition is a widely studied topic and, as mentioned above, it can be caused by different stimuli. Although some insulators can be understood in the context of single-electron theory such as band insulators and Anderson insulators, others, such as Mott insulators, are a result of electron-electron interaction. We note that Landau's Fermi-liquid theory which describes the low-energy properties of an interacting Fermi gas breaks down at the metal to Mott insulator transition.

The details of various forms of MIT are outside the scope of this thesis; we refer the interested reader to [4]. Here we briefly describe the MIT in 2DESs driven by disorder.

In 1958 Anderson recognized that, for non-interacting electrons, disorder may lead to electron localization which results in an insulating state [5]. Anderson localization is most easily understood to result from the interference of scattered electron waves in a random potential. Later, in 1979, the scaling theory of localization by Abrahams *et al.* [6] suggested that there are no extended states in 1D and 2D in the presence of disorder. Metallic states may exist only in 3D for sufficiently low disorder systems. However, two is the lower critical dimension for a metallic state and therefore states are only marginally (weakly) localized for low disorder systems. Furthermore, a small magnetic field or spin-orbit coupling can lead to the existence of extended states and thus a transition to a metallic state in 2D. Indeed experiments in high quality Si 2DESs [7] showed that, at high densities, the 2DES exhibits a metallic temperature dependence, and that the system can be driven to an insulating phase by lowering the 2DES density (increasing the disorder). Similar behavior has been reported for several other 2DESs [8; 9; 10; 11; 12; 13; 14; 15; 16; 17]. Although there is no consensus whether there exists a true metallic ground state (in the limit of zero temperature) for a low-disorder 2DES, it is generally believed that the observed metallic behavior is due to the interplay of disorder, interaction and finite temperature effects. Because of the temperature limitations, experimental determination of the true ground state of a 2DES remains a challenge. The theoretical understanding of MIT in 2D remains a challenge as well, because the localization length of a 2D system with disorder can be quite large so that the numerical studies on finite size samples may give misleading results.

1.3 Electrons in a magnetic field

So far we have discussed the behavior of electrons in the absence of magnetic field. In this section, we briefly explain what happens when an external magnetic field is turned on.

In 1879, Edwin Herbert Hall showed that there appears a voltage difference (the Hall voltage, V_{xy}) across a conductor, transverse to an electric current in the conductor and a magnetic field perpendicular to the current. The schematic of a transport measurement done in a Hall bar geometry is illustrated in Fig. 1.2. A current I is sent through the sample and voltages are measured along two different directions, namely along (longitudinal, V_{xx}) and across (transverse, V_{xy}) the current flow. Classically, the longitudinal resistance, calculated as $R_{xx} = V_{xx}/I$, is not effected by the magnetic field. However, the transverse resistance (Hall resistance), $R_{xy} = V_{xy}/I$, shows a linear increase with magnetic field. This observed Hall resistance comes about thanks to the Lorentz force ($\vec{F} = q\vec{v}\times\vec{B}$) which is perpendicular to the directions of both the motion of the charge carriers and the external magnetic field. Such a force accumulates the charge carriers at the edge of the sample resulting in a Hall voltage.

1.3.1 Integer quantum Hall effect

At sufficiently low temperatures, the 2DES shows deviations from this classical Hall effect. Instead of R_{xx} being fixed with B, it shows oscillations. Moreover, R_{xy} shows

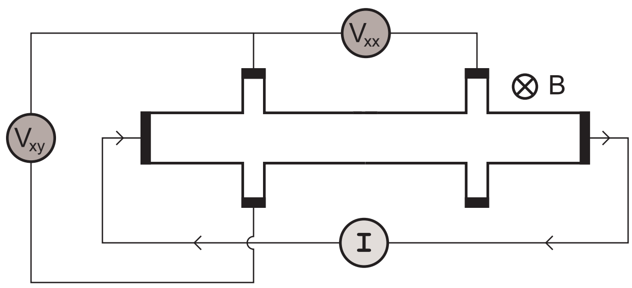

Figure 1.2: Schematic a transport measurement in a Hall bar geometry. Two contacts are used to send in a current I and the longitudinal (V_{xx}) and transverse (V_{xy}) voltages are measured as shown.

deviations from the linear B dependence and, for sufficiently high magnetic fields, it quantizes to values equal to $h/\nu e^2$ where ν is an integer. When R_{xy} is quantized, R_{xx} shows a vanishing value. This is the integer quantum Hall (IQH) effect [18], and is a result of the modification of the energy spectrum of single-particle states in the presence of a perpendicular magnetic field.

The density of states (DOS) of a 2DES is a constant (equal to $m/\pi\hbar^2$) as a function of energy in the absence of a magnetic field. However, when a perpendicular field is turned on, the DOS is quantized into a set of discrete Landau levels (LLs) separated by the cyclotron energy ($\hbar\omega_c = \hbar eB/m$). Because of the electron spin, each LL is further split into two levels, separated by the Zeeman energy ($E_Z = g\mu_B B$). Each of these spin-resolved LLs have a degeneracy of eB/h. Therefore, as the magnetic field is swept away from zero, the Fermi energy crosses these LLs one by one, causing R_{xx} to oscillate. When the number of electrons is just enough to occupy an integer number of these LLs, the Fermi energy rests in an energy gap, causing R_{xx} to vanish exponentially with decreasing temperature. For such a case, although the states are all localized in the bulk, there exist current-carrying edge states localized at the sample boundary but extended around the perimeter of the sample. These one-dimensional edge states result in the quantization of R_{xy} [19]. The number of occupied LLs is called the filling factor. The filling factor is given by $\nu = nh/eB$ and also describes the ratio of the number of electrons to magnetic flux quanta. A detailed description of the IQH effect can be found in Refs. [20] and [21].

1.3.2 Fractional quantum Hall effect

The IQH effect is the manifestation of the single-particle energy spectrum. However, this picture was proven not to be complete with the discovery of the fractional quantum Hall (FQH) effect [22]. An experiment by Tsui *et al.* showed that the quantized Hall resistance with vanishing longitudinal resistance seen at integer filling factors is also observed at fractional fillings. This gap opening at fractional fillings was a surprise since it cannot be explained within the single-particle picture and necessitates the inclusion of electron-electron interaction. Laughlin's [23] ingeniously guessed many-body wave function successfully explained the FQH states at $\nu = 1/(2i + 1)$ (including the first observed FHQ state at $\nu = 1/3$), where i is a positive integer. However, experiments in better quality samples showed that there exists a whole series of these FQH states at $\nu = p/2p + 1$, where p is an integer. Moreover, as new FQH states were discovered, the striking similarity between the IQH states around $B = 0$ and the FQH states around $\nu = 1/2$ became apparent. These experimental findings urged theorists to seek a unified theory that can capture these experimental observations. The composite fermion approach put forward by Jain [24] not only unified most of the observed FQH states, it also explained the connection between IQH and FQH effects.

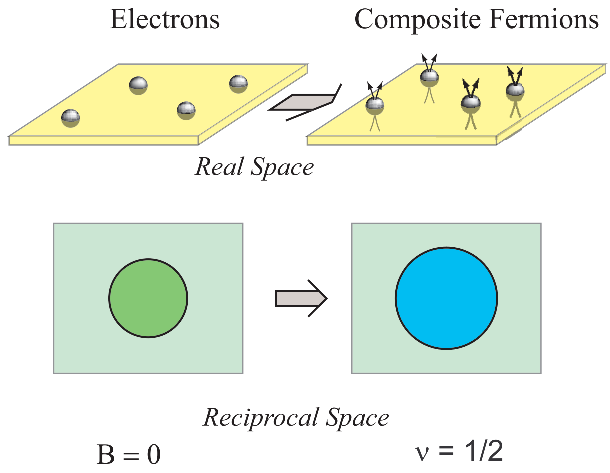

Figure 1.3: Schematics of 2D electrons and composite fermions in real space and their Fermi surfaces.

1.3.3 Composite fermions

Composite fermions (CFs) are formed by attaching an even number of magnetic flux quanta to each electron at high magnetic fields. With this transformation, interacting electrons at high magnetic fields turn into weakly interacting CFs moving in a reduced magnetic field. Indeed, because the attached flux exactly cancels out the external magnetic field at half-filled LLs, the CFs ignore the very large external magnetic field and behave as if they are at zero field. They are therefore predicted to have Fermi liquid properties and, in particular, form a Fermi sea [25; 26] similar to electrons at $B = 0$. A schematic is shown in Fig. 1.3. The existence of the CF Fermi sea has indeed been verified in numerous experiments [27; 28; 29].

As magnetic field is swept away from the value at a half filling, the CFs experience the residual (effective) magnetic and form LLs of their own. In this context, FQH states are actually IQH states of CFs formed at high fields, and a FQH state at $\nu = p/2p + 1$ corresponds to an IQH state of CFs at CF filling factor p. For example,

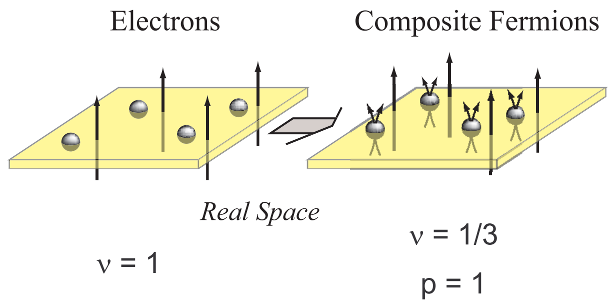

Figure 1.4: Schematics of quantum Hall states at $\nu = 1$ and $\nu = 1/3$ in real space.

at $\nu = 1/3$, there exist three magnetic flux quanta per electron. However, electrons transform into CFs with the attachment of two flux quanta to each electron. After this transformation, there remains only one magnetic flux quanta per CF. This gives an integer filling of one for CFs and makes an analogy with the state at $\nu = 1$. A schematic of states at $\nu = 1$ and $\nu = 1/3$ is shown in Fig. 1.4. For a detailed formulation of the CFs see Ref. [26].

Chapter 2

AlAs band structure and samples

In this Chapter, we describe the electron system used in this thesis. We first present the band structure of bulk AlAs and then the valley occupation in AlAs quantum wells. Finally we give details of our sample preparation techniques.

2.1 AlAs band structure

Since GaAs and Si are among the most studied semiconductors, it is instructive to present the band structure of AlAs in comparison with Si and GaAs. The band structures of these three semiconductors together with their first Brillouin zones are shown in Fig. 2.1. GaAs has a conduction-band minimum (CB) at the Γ-point of the Brillouin zone. Because of the symmetry of the Γ-point, the band effective mass is isotropic with a value of 0.067 (in units of free electron mass). The band g-factor for GaAs is $g_b = -0.44$, which is very different from the free electron value of 2 thanks to the mixing of the valence-band (VB). In contrast to GaAs, AlAs and Si are both indirect band gap materials with the CB minima (valleys) located away from the Γ-point. In Si, the CB minima occur along the Δ-line (line from Γ-point to X-point), giving rise to a six-fold valley degeneracy. Moreover, the effective mass is

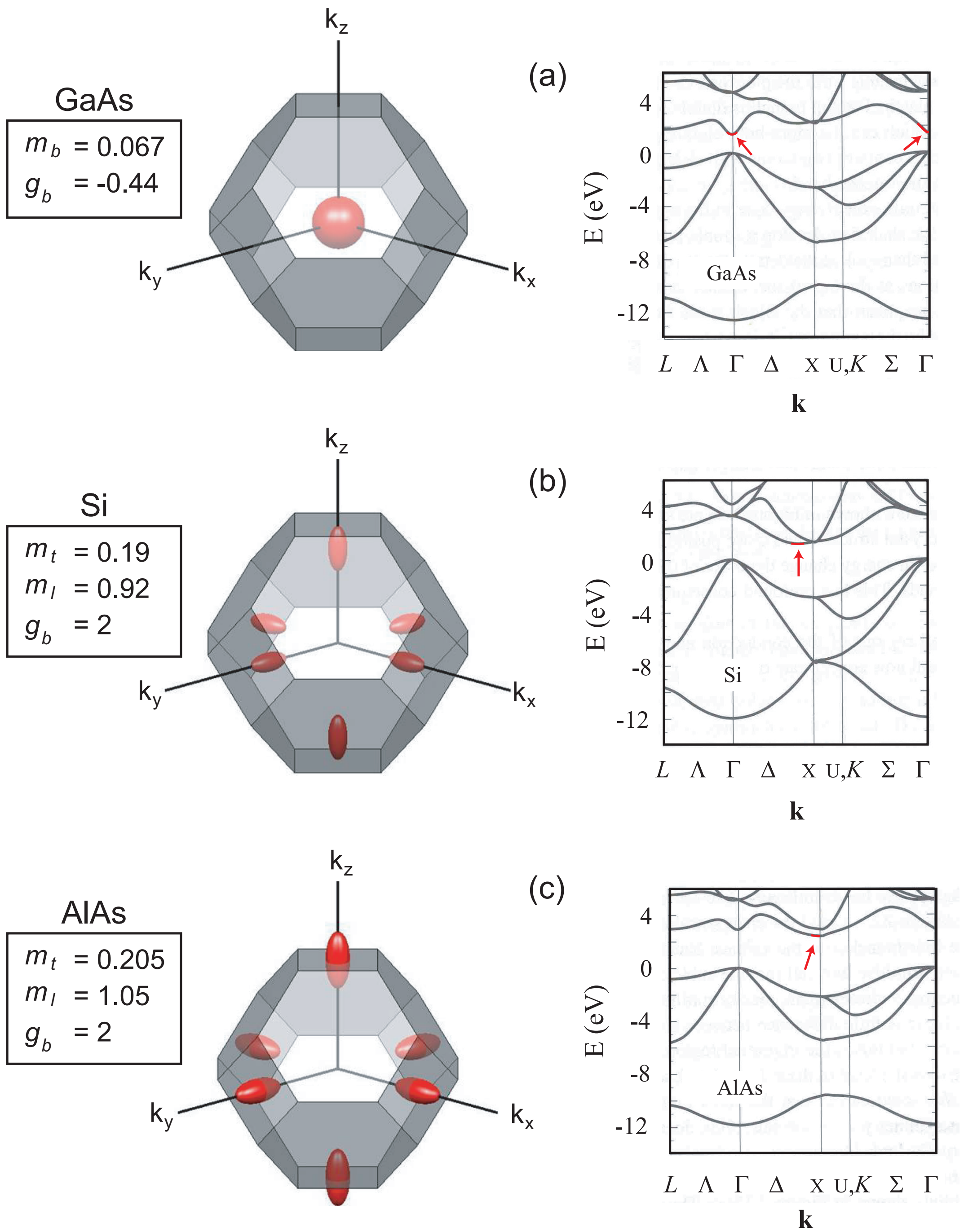

Figure 2.1: Band structures for (a) GaAs, (b) Si, and (c) AlAs taken from Ref. [21] are shown on the right. The lowest energy electron pockets are shown by red arrows. Representations of the electron pockets and the first Brillouin zones are shown on the left.

anisotropic and characterized by transverse and longitudinal masses where $m_l = 0.92$ and $m_t = 0.19$. For AlAs, however, the CB minima are exactly at the X-points. There are only three non-equivalent X-points in the first Brillouin zone giving rise to a three-fold valley degeneracy for AlAs. Similar to Si, AlAs also has an anisotropic band effective mass with $m_l = 1.05$ and $m_t = 0.205$. For both Si and AlAs, the band g-factor is 2 because of the absence of VB mixing.

2.2 AlAs quantum wells

We studied high-mobility 2DESs confined to modulation-doped AlAs layers with varying widths, grown by molecular beam epitaxy on (001) GaAs substrates. In Fig. 2.2(a) we show the typical structure of an AlAs quantum well (QW) flanked by $Al_{0.39}Ga_{0.61}As$ barriers. Si dopants are placed at a distance of 75 nm away from the AlAs layer in the top $Al_{0.39}Ga_{0.61}As$ layer. The structure is finished with a GaAs cap layer. The corresponding band diagram for our sample structure is shown in Fig. 2.2(b). The solid and dashed lines show the positions of the X-point and the Γ-point CB energy minima, respectively. As the band diagram suggests, the 2D electrons are confined in the AlAs QW at the X-point.

As mentioned above, in bulk AlAs there are three anisotropic valleys with their major axes along the [100], [010] or [001] crystal directions. We denote them as [100], [010] and [001] valleys, or equivalently X, Y and Z valleys (see Fig. 2.3(a)). We also refer to the [001] valley as the out-of-plane valley and [100] and [010] valleys as the in-plane valleys. When electrons are confined to an AlAs QW, their motion in the growth ([001] or z) direction freezes and they move only in two dimensions. The projection of the Fermi surfaces of these three valleys onto the plane of the motion

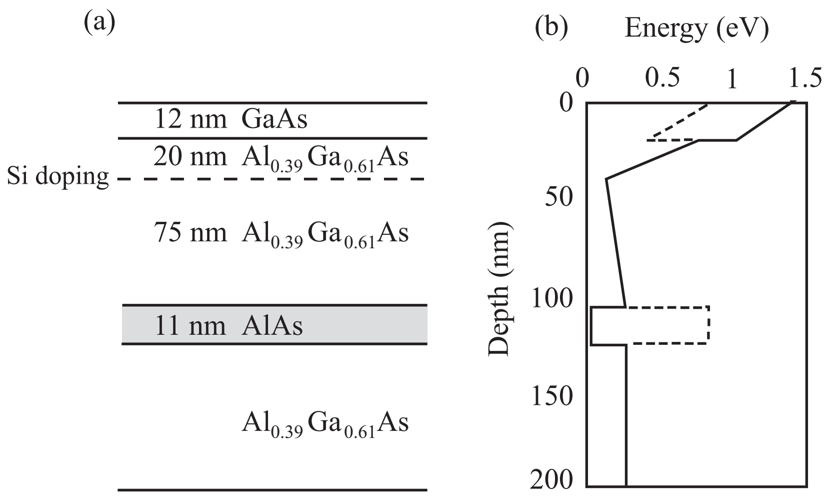

Figure 2.2: (a) Typical structure of an AlAs quantum well. (b) Corresponding band diagram, showing the conduction-band edge at the Γ-point (dashed lines) and the X-point (solid lines). This figure is adapted from Ref. [30].

is shown in Fig. 2.3(b). As seen in Fig. 2.3(b), these valleys have very different properties when electrons are confined to 2D. The out-of-plane valley has an isotropic Fermi surface with a band effective mass $m_b = m_t = 0.205$. However, the two in-plane valleys have anisotropic Fermi contours with anisotropic band masses equal to 0.205 and 1.05, leading to $m_b = \sqrt{m_l m_t} = 0.46$.

The anisotropy of the valleys in AlAs has another interesting consequence. When electrons are confined to a QW they occupy the lowest energy subband. As can be seen in Fig. 2.3(a), the out-of-plane valley has a larger mass along the growth direction compared to the two in-plane valleys, therefore, the confinement energy for the out-of-plane valley is smaller compared to the in-plane valleys. Indeed, electrons confined to narrow AlAs QWs occupy the single out-of-plane valley. However, there exists a competing effect because of the slight mismatch of the lattice constants of AlAs and the GaAs substrate: AlAs feels a residual in-plane biaxial compressive

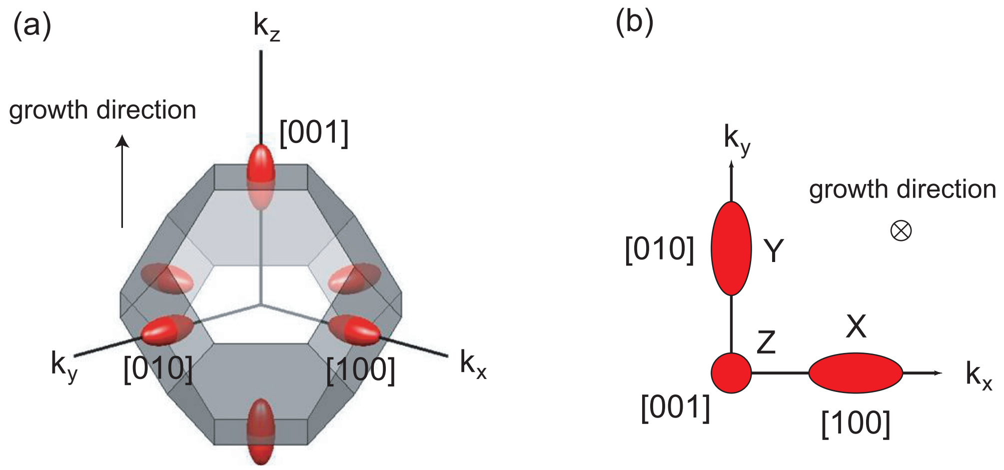

Figure 2.3: (a) Representation of conduction-band carrier pockets and the first Brillouin zone of AlAs. (b) Projection of the carrier pocket Fermi surfaces onto the plane of 2D motion.

strain which lowers the energies of the two in-plane valleys compared to the out-of-plane valley. For wide AlAs QWs this effect dominates and electrons occupy the two in-plane valleys. Experimentally the crossover happens at a well width of about 5.5 nm. Thus AlAs provides us with a unique opportunity to study a single-valley system with an isotropic in-plane Fermi contour in narrow wells (width $<$ 5.5 nm) or a two-valley system with anisotropic in-plane Fermi contours in wide wells (width $>$ 5.5 nm).

2.2.1 Controlling valley splitting in wide AlAs quantum wells

We already mentioned that the built-in biaxial strain lowers the energies of the two in-plane valleys that are occupied in wide AlAs QWs. Furthermore, we can control the occupation of these two in-plane valleys via application of in-plane uniaxial strain. For this purpose, we glue our samples to a piezoelectric actuator (piezo), and apply voltage bias to the piezo to stretch the sample in one direction and compress it in

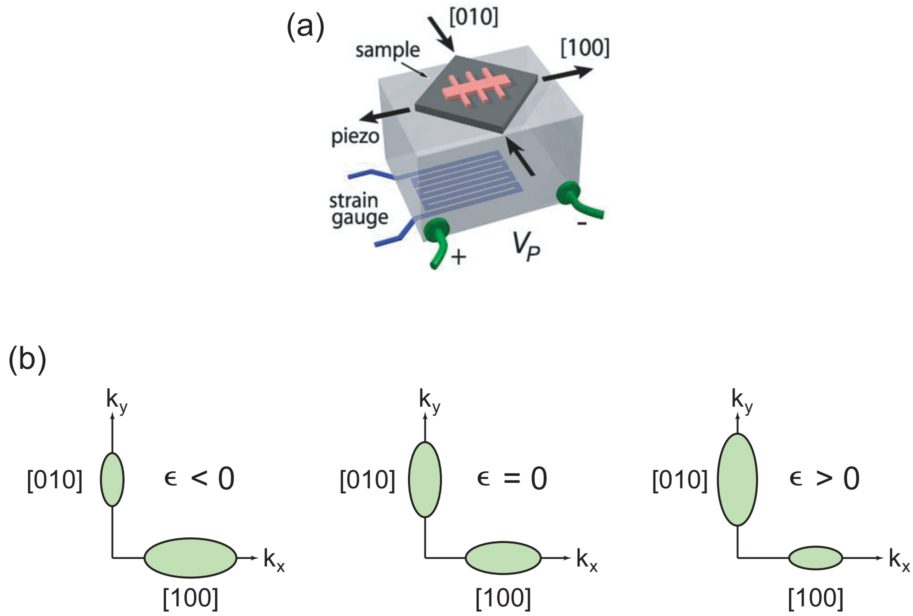

Figure 2.4: (a) Schematic showing our experimental setup to apply controllable in-plane strain *in-situ*. The sample is glued to one face of the piezo and a strain gauge glued to the opposite side is used to measure the applied strain. (b) Schematic showing the distribution of electrons among the [100] and [010] valleys at different strain values.

the perpendicular direction (see Fig. 2.4(a)). This results in a symmetry breaking strain $\epsilon = (\epsilon_{[100]} - \epsilon_{[010]})$, where $\epsilon_{[100]}$ and $\epsilon_{[010]}$ are the strains along the [100] and [010] directions. As illustrated in Fig. 2.4(b), for $\epsilon > 0$ electrons are transferred from the [100] valley to the [010] valley and vice-versa for $\epsilon < 0$; in either case the total density remains essentially fixed with strain. The resulting valley splitting energy is given by $E_V = E_2\epsilon$ where E_2 is the conduction-band deformation potential which in AlAs has a band value of 5.8 eV. We use a metal-foil strain gauge glued to the opposite face of the piezo to measure the applied strain.

2.3 Sample preparation and measurement set up

We start by cleaving a piece with a size of roughly 4 by 4 mm from the MBE wafer. Then, we make ohmic contacts by depositing AuGeNi (200 Å Ge/ 400 Å Au/ 100 Å Ni/ 400 Å Au) and alloying in a reducing environment for 11 minutes at 483 °C. As a next step, we pattern the sample either in a Hall bar or a van der Pauw configuration using photolithographic techniques. After the etching of the sample, we deposit a front gate (100 Å Ti / 200 Å Au) on the sample which allows us to control the 2D electron density. For narrow AlAs QW samples, we put a back gate by simply placing the sample with melted In onto a Si piece that is cut slightly larger than the sample dimensions. As a last step we wire the sample to a dual in-line pin (DIP) header. However, wide AlAs QW samples go through extra processing steps. After the front gate deposition, the samples are thinned to a thickness around 200 μm using either a mechanical lapping or bromine-methanol etch process. After the thinning process, we deposit a back gate (1000 Å Ti / 200 Å Au) and then glue our sample on to a piezo. Following the wiring step, samples are ready for the measurement. The more comprehensive description of our sample preparation steps can be found in Refs. [31] and [32].

We performed magnetoresistance measurements in a ^{3}He system or a dilution refrigerator with base temperatures of 300 mK and 20 mK, respectively. The samples were mounted on a tilting stage to allow the angle, θ, between the normal to the sample and the magnetic field to be varied *in-situ*. We used standard low frequency lock-in techniques for our transport measurements with the frequency ranging from 7 - 17 Hz. We typically send a current of 10 - 40 nA through the sample. We used following systems for the measurements :

- ^{3}He system with 16 T superconducting magnet, Princeton (C)
- Dilution refrigerator with 18 T superconducting magnet, NHMFL Florida (M)
- ^{3}He system with either 31 T or 33 T resistive magnet, NHMFL Florida (H)

For a typical sample, we use a notation such as M424J4-C1 where 'M424' refers to the name of the MBE grown wafer, 'J4' denotes the particular piece of the wafer that is used to make the sample, 'C' corresponds the system used to perform measurements (see the list above), and '1' is the cooldown number.

Chapter 3

Effective mass of 2D electrons in wide AlAs quantum wells

3.1 Introduction

As the density of an interacting two-dimensional electron system (2DES) is reduced, the interaction strength characterized by $r_s = 1/\sqrt{\pi n}a_B^*$ is enhanced. In the Fermi liquid theory, electron-electron interaction renormalizes the 2DES fundamental parameters, such as the effective mass (m^*) and the spin susceptibility ($\chi_s^* \propto g^* m^*$), where g^* is the effective Lande g-factor [33; 34]. In particular, χ_s^* and m^* are expected to be larger than the band values ($\chi_{s,b}$ and m_b) for large r_s [33; 34; 35; 36; 37; 38; 39; 40; 41; 42]. Enhancements of χ_s^* and m^* at large r_s are indeed observed in a number of different 2DESs [43; 44; 45; 46; 47; 48; 49; 50; 51; 52; 53; 54; 55; 56; 57; 58; 59].

In addition to r_s, the role of spin and valley degrees of freedom on χ_s^* and m^* renormalization has been of interest since additional degrees of freedom may change the nature of the interaction. Thanks to the control over spin and valley energies in wide AlAs quantum wells (QWs), this system provides the unique opportunity to realize all four possible spin and valley subband occupations: s_2v_2, s_2v_1, s_1v_2 and s_1v_1, where s and v stand for spin and valley, and 1 and 2 denote the number of occupied spin or valley subbands. The results summarized in this Chapter provide direct and conclusive evidence that the valley and spin degrees of freedom are indeed both important in m^* renormalization. Although m^* shows some variation with spin and valley polarization, if the electrons are only partially valley and/or spin polarized, then their m^* is enhanced with respect to m_b and increases with increasing r_s. But if they are fully valley and spin polarized, then m^* is suppressed even for r_s up to 21.

We studied high-mobility 2DESs confined to wide AlAs QWs. The AlAs wells in these samples have widths of 11 nm (sample M409Q2), 12 nm (samples M420N1 and M424J4), or 15 nm (samples M415N1 and M408ID4). As described in section 2.2, in these wide AlAs QWs, the 2D electrons occupy two energetically degenerate conduction-band valleys with elliptical Fermi contours, characterized by transverse and longitudinal band effective masses, $m_t = 0.205$ and $m_l = 1.05$ (in units of free electron mass). Details of our sample preparation steps are given in section 2.3. We control the valley occupation via applying a symmetry breaking strain and the spin occupation (polarization) through the application of magnetic field. For the density range 0.55 - 4.8 10^{11} cm^{-2}, the low-temperature mobility for the samples are between 9 and 60×10^3 cm^2/Vs when current is passed along the low-mobility (longitudinal) direction of the occupied valley; for current along the high mobility (transverse) direction, the mobility is typically 3 to 5 times larger than the above values.

3.2 Analysis methods

To deduce m^*, we analyzed the temperature (T) dependence of the strength (ΔR) of the Shubnikov de Haas (SdH) oscillations using the standard Dingle expression [60; 61]:

$$\frac{\Delta R}{R_o} = 8exp(\frac{-\pi}{\omega_c \tau_q})\frac{\xi}{sinh(\xi)} \tag{3.1}$$

$$\xi = \frac{2\pi^2 k_B T}{\hbar\omega_c} \tag{3.2}$$

where the factor $\xi/sinh(\xi)$ represents the T-induced damping, and $\omega_c = eB_\perp/m^*$ is the cyclotron frequency, $B_\perp$ is the perpendicular component of the magnetic field, R_o is the non-oscillatory component of the resistance near a SdH oscillation, and τ_q is the single-particle (quantum) lifetime. We analyzed our data using two methods, each based on a different set of assumptions. First, we assumed that both R_o and τ_q are T-independent. This is the usual assumption, commonly made when the T-dependence of R_o is small. For our samples the T-dependence of R_o is indeed weak at high densities. At low densities, however, R_o becomes T-dependent, implying that τ_q can depend on T. According to a theoretical study [62], for short-range scatterers, the relative T-dependent correction to τ_q is half of the relative correction to the transport scattering time $\tau_{tr} \propto 1/R_o$. For long-range scatterers, the T-dependent correction to τ_q is expected to be smaller. In our second analysis method, we included the T-dependence of R_o, and assumed that the relative T-dependence of τ_q is equal to half the relative T-dependence of R_o. We emphasize that in all cases our data can be fit reasonably well to the Dingle expression in the whole temperature and magnetic field range by assuming two constants τ_q and m^*. However, this does not justify that τ_q is independent of T; indeed a given data set can be fit equally well to the Dingle expression with a different, fixed m^*, and a τ_q that has some T-dependence. Since m^* and the T-dependence of τ_q cannot be determined independently, in our second analysis method we use the T-dependence of the background resistance to estimate the T-dependence of $1/\tau_q$ and deduce m^*. Note that these two methods should bound the maximum error in m^* determination introduced by the T-dependence of τ_q.

3.3 Determination of spin and valley phase diagram

Next we discuss the experimental determination of spin and valley subband occupations in parallel magnetic field ($B_{\parallel}$) vs. strain (ϵ) phase diagram. Figure 3.1 highlights the important features of the spin and valley subband occupations. In this figure, the thick, solid lines mark the boundaries between the four possible spin and valley subband occupations for sample M424J4 at $n = 2.6 \times 10^{11}$ cm^{-2}; we denote the occupations by s_2v_2, s_2v_1, s_1v_2 and s_1v_1, where s and v stand for spin and valley, and 1 and 2 denote the number of spin/valley subbands that are occupied.

We determined the boundaries between different spin and valley occupations from measurements of sample resistance (R) vs. either $B_{\parallel}$ or ϵ while the other parameter is kept fixed. Examples of such data are shown in Fig. 3.2 for sample M424J4 with the current passed along the [110] direction. In each set of traces, R increases and shows a kink at a field or strain, B_P or ϵ_P, which marks the onset of full spin or valley polarization, respectively. B_P and ϵ_P are marked by dashed lines in Fig. 3.2. In Fig. 3.1, the B_P values are shown by blue triangles whereas the ϵ_P values are shown by black squares or red circles for positive and negative values of strain respectively.

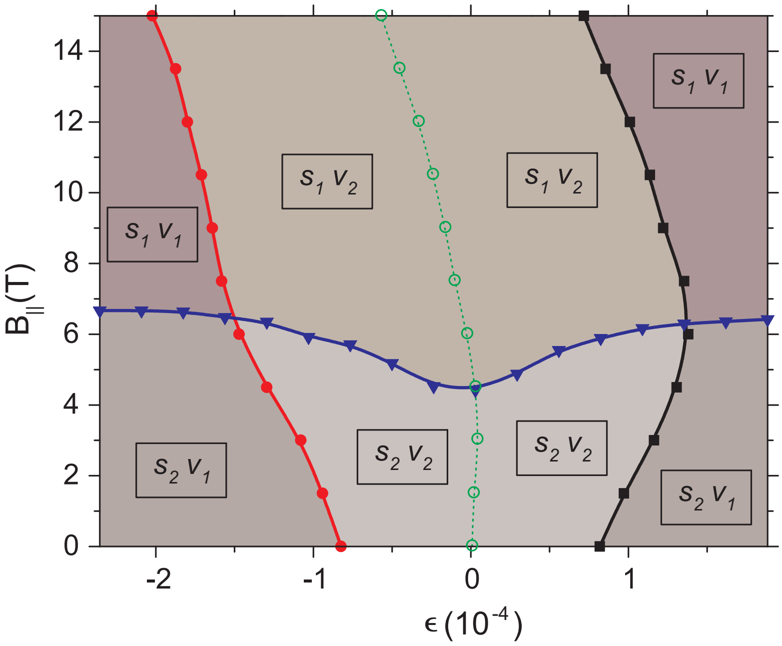

Figure 3.1: The spin (s) and valley (v) occupations for sample M424J4 at density $n = 2.6 \times 10^{11}$ cm^{-2} are shown as a function of parallel field ($B_{\|}$) and strain (ϵ). The indices 1 and 2 indicate, respectively, whether one or two spin (and/or valley) subbands are occupied. The thick, solid lines mark the onset of full spin/valley polarization, and the dotted line indicates the "balanced" condition where the two valleys are equally populated.

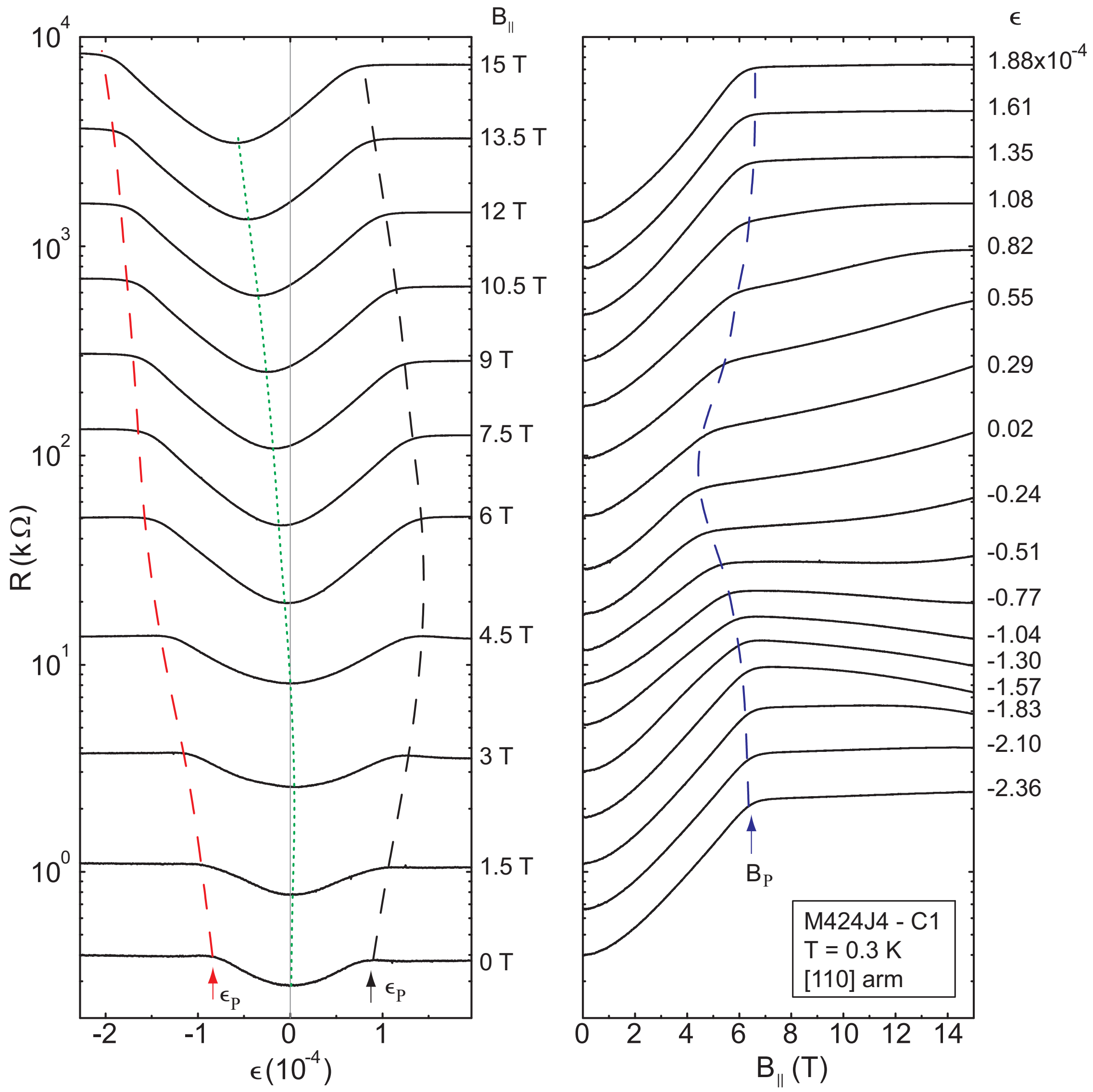

Figure 3.2: Piezoresistance (left panel) and magnetoresistance (right panel) for sample M424J4 - C1 taken at a density $n = 2.6 \times 10^{11}$ cm^{-2} at different magnetic field and strain values as indicated on the right of each trace. The dashed lines mark the onset of full spin or valley polarization, and the dotted line the "balanced" point where the two valleys are equally occupied.

Note in Figs. 3.1 and 3.2 that the boundaries are not simple horizontal or vertical lines. This is because the Fermi energy (E_F) depends on the size of the (partial) occupation of the valleys or spins. Moreover, B_P for v_1 is not simply twice of B_P for v_2 and similarly, ϵ_P for s_1 is not twice of ϵ_P for s_2 either. This is because spin and valley susceptibilities depend on the valley and spin occupation [49; 59; 63]. We note that the spin and valley susceptibilities can be deduced from the values of B_P and ϵ_P and they are indeed consistent with the previous susceptibility measurements performed in similar systems [49; 59; 63].

We also emphasize that in a 2DES with finite layer thickness there is a shift, with $B_{\|}$, of ϵ at which the valleys are equally occupied, or are "balanced", as indicated by open circles (dotted line) going through $\epsilon = 0$ in Fig. 3.1. The balanced point is clear from the piezoresistance traces shown Fig. 3.2 and is marked by the green dotted line. In our experiments, where $B_{\|}$ is along [100], the balanced point shifts to negative values of ϵ at high $B_{\|}$ because, $B_{\|}$ shifts the energy of the [100] valley above the [010] valley [64]. Although we can measure and explain the boundaries shown in Fig. 3.1 accurately, their precise locations are not important for the conclusions of this Chapter. As we describe below, we carefully choose the conditions of our sample ($B_{\|}$, ϵ, and θ) when we perform our m^* measurements for different combinations of spin and valley occupation.

3.4 Dependence of effective mass on spin and valley degrees of freedom

In this section, we present measurements of m^* for sample M409Q2 at a fixed density $n = 3.8 \times 10^{11}$ cm^{-2} for the four possible spin and valley subband occupations: s_2v_2, s_2v_1, s_1v_2 and s_1v_1. Sample M409Q2 is patterned with a 60×60 μm^2 square mesa whose edges are aligned along the [100] and [010] directions, and the current is passed along the [010] direction.

3.4.1 Spin and valley phase diagram

The four possible spin and valley subband occupations of sample M409Q2 at $n = 3.8 \times 10^{11}$ cm^{-2} are shown in the $B_\parallel$ vs. ϵ phase diagram in Fig. 3.3. We determined the boundaries between different subband occupations from measurements of sample resistance (R) vs. either $B_\parallel$ or ϵ as discussed before. Examples of such data are shown in Fig. 3.4 at two temperatures. We note that, in contrast to the data presented in Fig. 3.2, in this case the current is passed along [010], therefore the piezoresistance is not symmetric around $\epsilon = 0$ because of the mass anisotropy of the valleys. The B_P and ϵ_P values are shown in Fig. 3.3 by closed triangles or squares, respectively. The stars show the coordinates where we measured m^* in these four quadrants, and the deduced m^* values are indicated next to the stars. The shift of the balance point with $B_\parallel$ is indicated by the thin, dotted, green line going through $\epsilon = 0$. Finally, the open diamonds and the dashed lines in Fig. 3.3 mark the boundary for the apparent metal-insulator transition observed at this density in sample M409Q2 (see Fig. 3.4

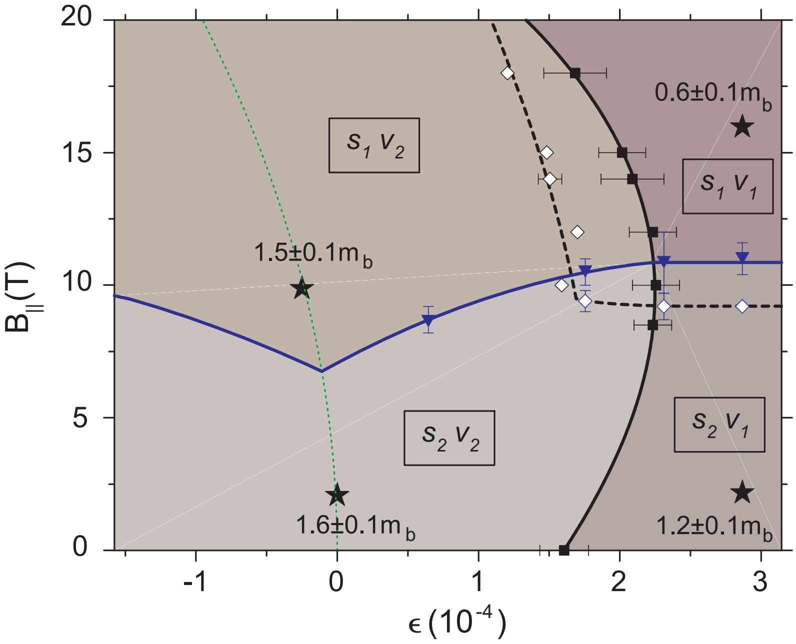

Figure 3.3: The spin (s) and valley (v) occupations for sample M409Q2 at density $n = 3.8 \times 10^{11}$ cm^{-2} are shown as a function of parallel magnetic field ($B_\parallel$) and strain (ϵ); the thick, solid lines mark the boundaries and the indices 1 and 2 indicate, respectively, whether one or two spin (and/or valley) subbands are occupied. Dashed lines mark the boundary of the upper-right region where the sample exhibits an insulating behavior. Stars mark the ($B_\parallel$, ϵ) values at which the indicated effective mass was measured.

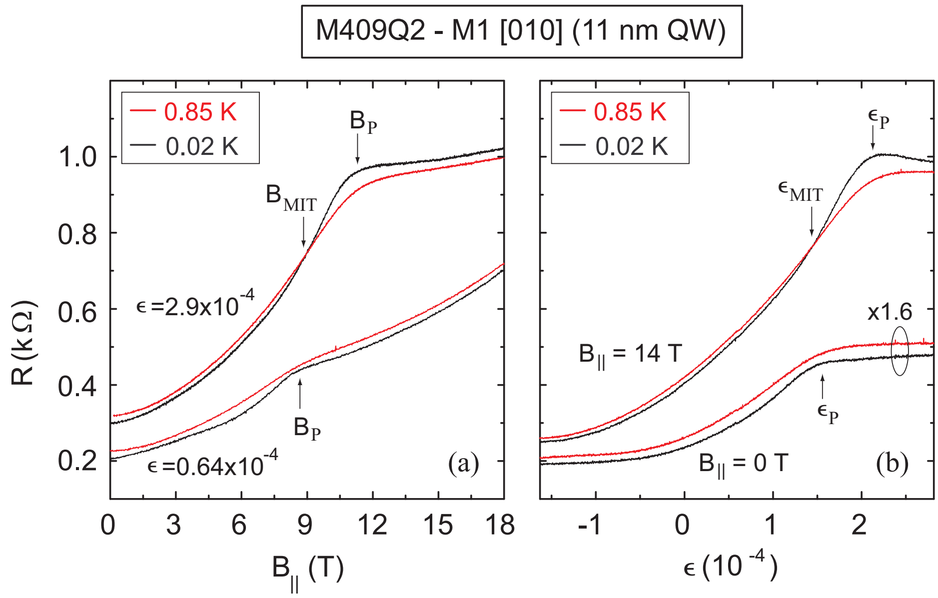

Figure 3.4: Sample resistance is shown as a function of (a) $B_{\|}$ and (b) ϵ at two temperatures for sample M409Q2 at density $n = 3.8 \times 10^{11}$ cm^{-2}. For each pair of traces in (a), ϵ is kept constant while for each pair in (b) $B_{\|}$ is kept fixed at the indicated values.

data). The 2DES shows an insulating behavior only as it becomes sufficiently spin and valley polarized [65].

3.4.2 Temperature dependence of Shubnikov de Haas oscillations

Here we describe our determination of m^* from the T-dependence of the Shubnikov-de Haas (SdH) oscillations, in different quadrants of Fig. 3.3. Figure 3.5 shows the data for the s_1v_2 case which were taken at $\theta = 74.8°$ and $\epsilon = -0.16 \times 10^{-4}$. These values for θ and ϵ were chosen carefully so that the lowest eight Landau levels (LLs) are spin polarized and the two valleys have equal densities at the LL filling factor $\nu = 6$, as shown in Fig. 3.5(b). Figure 3.5(a) shows the SdH oscillation near $\nu = 6$

at several T. To deduce m^*, we analyze the T-dependence of the amplitude of SdH oscillations using the standard Dingle expression described in section 3.2. We first make the common assumption that both R_o and τ_q are T-independent and analyze our data using our first analysis method discussed in section 3.2. We will return to its justification later in this section. Figure 3.5(c) shows that the data points (red circles) fit the Dingle expression (red line) quite well, yielding $m^* = 1.58m_b$, where $m_b = \sqrt{m_l m_t} = 0.46$.

In Fig. 3.5(d) we show an alternative set of data from which we determine m^* for the s_1v_2 case. In contrast to the standard SdH oscillations shown in Fig. 3.5(a), where we vary the magnetic field at constant ϵ, in Fig. 3.5(d) we fix the value of field so that the 2DES remains at $\nu = 6$ and continuously change ϵ (see Refs. [59; 63] for details). With applied ϵ, the LLs for the [100] and [010] valleys cross each other, as the fan diagram in Fig. 3.5(e) indicates, and R exhibits minima as E_F goes through consecutive energy gaps, and maxima as it coincides with the LL crossings. We analyzed the T-dependence of the amplitudes of these resistance oscillations to deduce m^*. In Fig. 3.5(c) we show a plot of $\Delta R/T$ vs. T (blue squares) for the oscillation centered around $\epsilon = -0.16 \times 10^{-4}$; the data fit the Dingle expression quite well (blue line), and yield $m^* = 1.46m_b$ which is close to the value obtained from the field-sweep data of Fig. 3.5(a). In a similar fashion, we analyzed the T-dependence of the other resistance oscillations observed in Fig. 3.5(d); the data fit the Dingle expression well, and provide the m^* values plotted in Fig. 3.5(f). Evidently, m^* is smaller when we "valley polarize" the 2DES: note that the valley polarization (P_v), defined as the difference between the [010] and [100] valley populations divided by

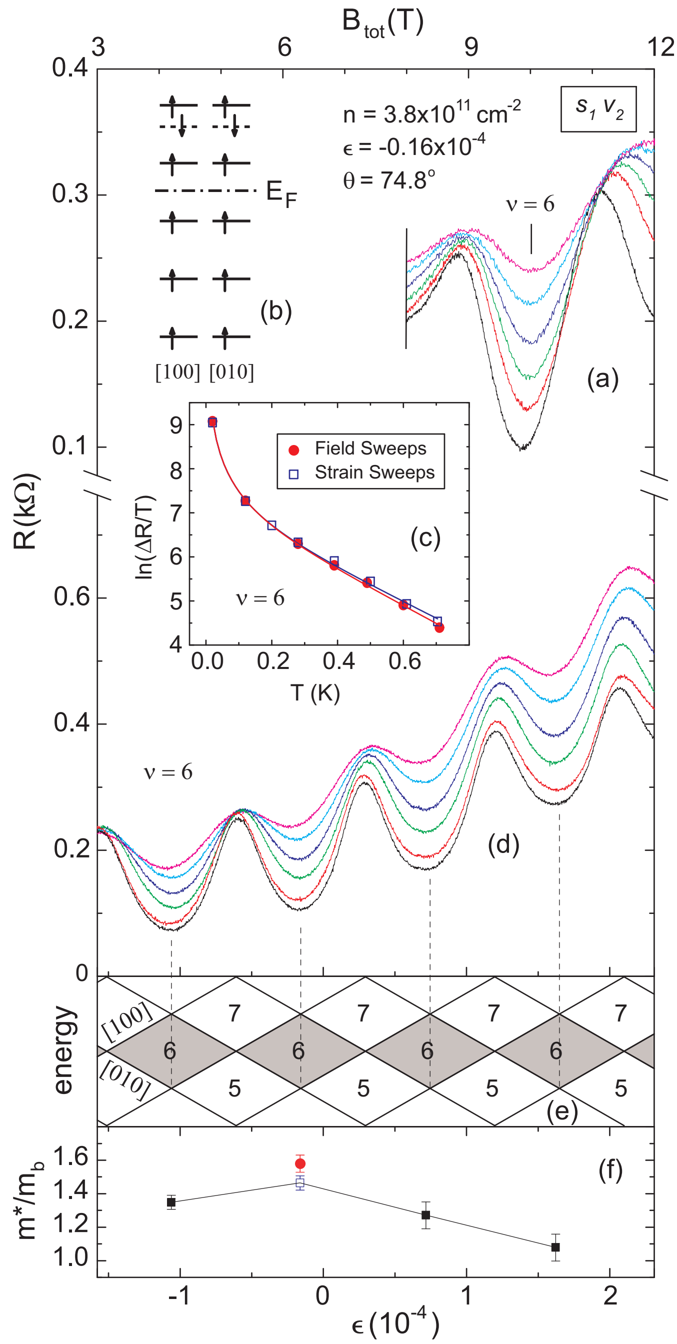

Figure 3.5: Summary of measurements for the $s_1 v_2$ case for sample M409Q2 at density $n = 3.8 \times 10^{11}$ cm^{-2}. (a) and (d) Field and strain traces taken at different temperatures ranging from 0.02 K to 0.7 K (bottom to top). (b) Energy level diagram. (c) Dingle fits at $\nu = 6$. (e) Landau level fan diagram as a function of ϵ. (f) Deduced values of m^* as a function of ϵ.

the total 2DES density, is equal to -0.33, 0, 0.33, and 0.67 for the four data points shown in Fig. 3.5(f) (from left to right).

The data for the s_1v_1 case are shown in Fig. 3.6(a). Here ϵ is large enough so that only the [010] valley is occupied. Moreover, by tilting the sample to a sufficiently large θ we ensure that the lowest seven LLs are spin polarized, as indicated in Fig. 3.6(a) energy level diagram. Note the qualitative similarity of the field traces in Figs. 3.6(a) and 3.4(b): R shows a pronounced increase with field and then saturates above ~ 11 T once the 2DES is completely spin polarized. Since the sample is not completely parallel to the field in Fig. 3.6(a), however, there are SdH oscillations which become well resolved after the full spin polarization; these are the oscillations from which we deduce m^*. The inset to Fig. 3.6(a) shows the T-dependence of the SdH oscillation centered around $\nu = 5$. From the fit to the Dingle expression we obtain m^*=0.62m_b at this $\nu = 5$; data at $\nu = 6$ yield m^*=0.60m_b.

Figure 3.6(b) shows data for the s_2v_1 case. Here ϵ is chosen large enough so that the system is completely valley polarized and θ is adjusted such that the LLs at odd ν are at coincidence. The corresponding LL energy diagram is shown in Fig. 3.6(b) inset. Consistent with this diagram, in Fig. 3.6(b) traces, resistance minima at even ν are strong while the minima at odd ν are either weak or entirely absent (at high ν), or are accompanied by spikes (e.g., at $\nu = 3$) [66]. By fitting the amplitude of the SdH oscillations near $\nu = 8$, 10, and 12 to the Dingle expression, we obtain m^*=1.16, 1.22, and 1.22m_b, respectively (see Fig. 3.6(b) inset as an example). This observation implies that m^* does not depend on the spin polarization (P_s), defined as the difference between the spin up and down populations divided by the total electron density; such

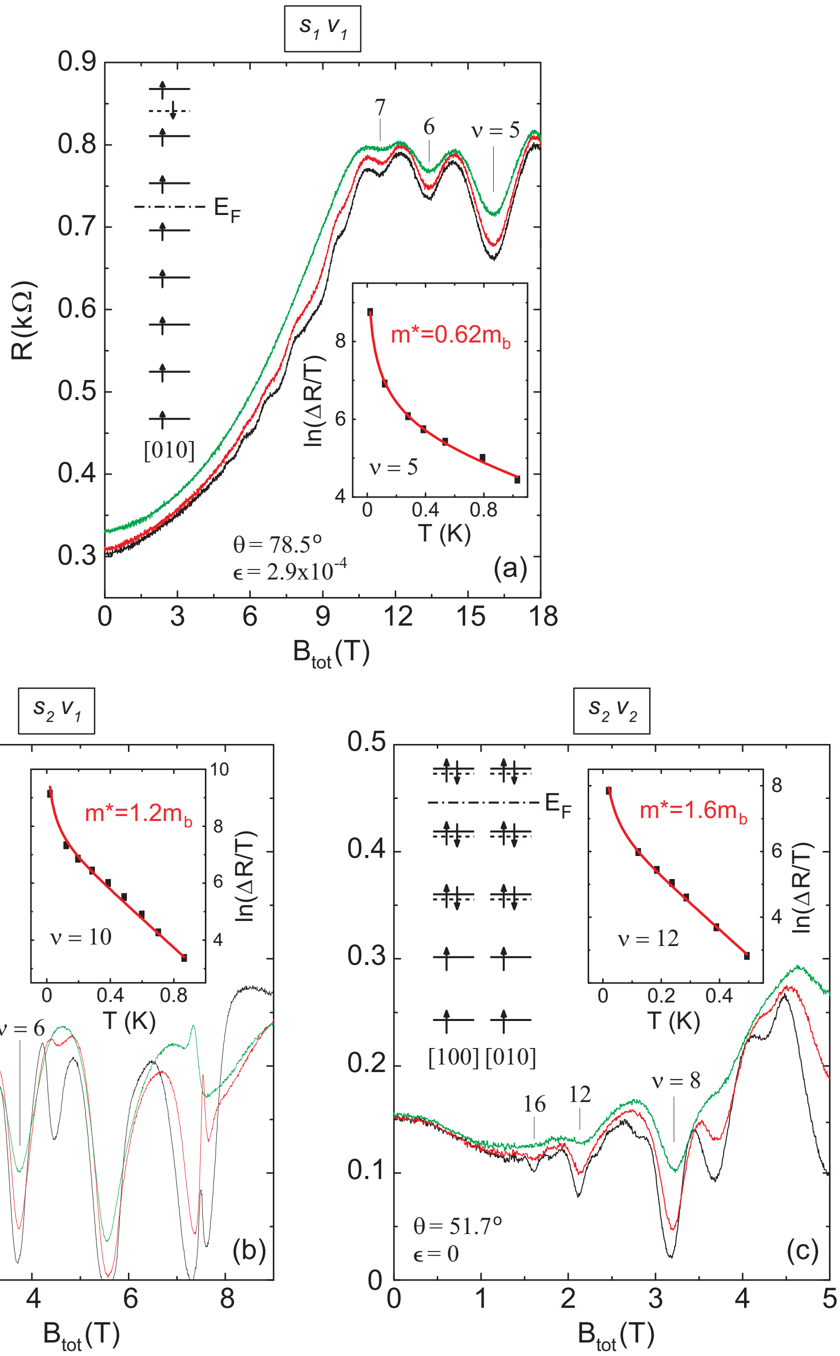

Figure 3.6: Magnetoresistance traces, Dingle fits, and energy level diagrams for s_1v_1, s_2v_1 and s_2v_2 for sample M409Q2 at density $n = 3.8 \times 10^{11}$ cm^{-2}. The black, red and green traces were taken at (a) 0.02, 0.39, 1.03; (b) 0.02, 0.60, 0.87; (c) 0.02, 0.24, 0.39 K.

independence is not surprising since in the range of $8 \leq \nu \leq 12$, P_s changes only from 0.17 to 0.25.

In Fig. 3.6(c), we show data for s_2v_2. Here $\epsilon = 0$ and θ is chosen so that the spin-up and spin-down LLs are at coincidence, as illustrated in the energy diagram in Fig. 3.6(c). The strongest resistance minima are observed at $\nu = 8$, 12, and 16. We obtain $m^* = 1.58m_b$ from the fit of SdH oscillation amplitude around $\nu = 12$ to the Dingle expression, as shown in Fig. 3.6(c) inset.

In our determination of m^* from the SdH oscillations, we have assumed that R_o and τ_q are T independent. It is apparent in Figs. 3.5 and 3.6, however, that R_o has some dependence on T. We also analyzed our data using our second analysis method as described in section 3.2. In our second analysis method we assumed that the relative T-dependence of τ_q is similar to but has half the size of the relative T-dependence of R_o. The deduced m^* from such analysis are about 10% smaller than the values reported above, indicating that the main conclusions of our study remain intact.

3.5 Density dependence of effective mass

We repeat the m^* measurements in these four quadrants as function of density for several samples. Figure 3.7 shows the summary of our m^* data. In Fig. 3.7, v_2 corresponds to equal distribution of electrons in two valleys and therefore valley polarization is zero ($P_v = 0$), whereas the s_2 case corresponds to a spin polarization range of $0.14 \leq P_s \leq 0.33$. Our results provide direct experimental evidence for the dependence of m^* on valley and spin occupations of the 2DES. This is intuitively

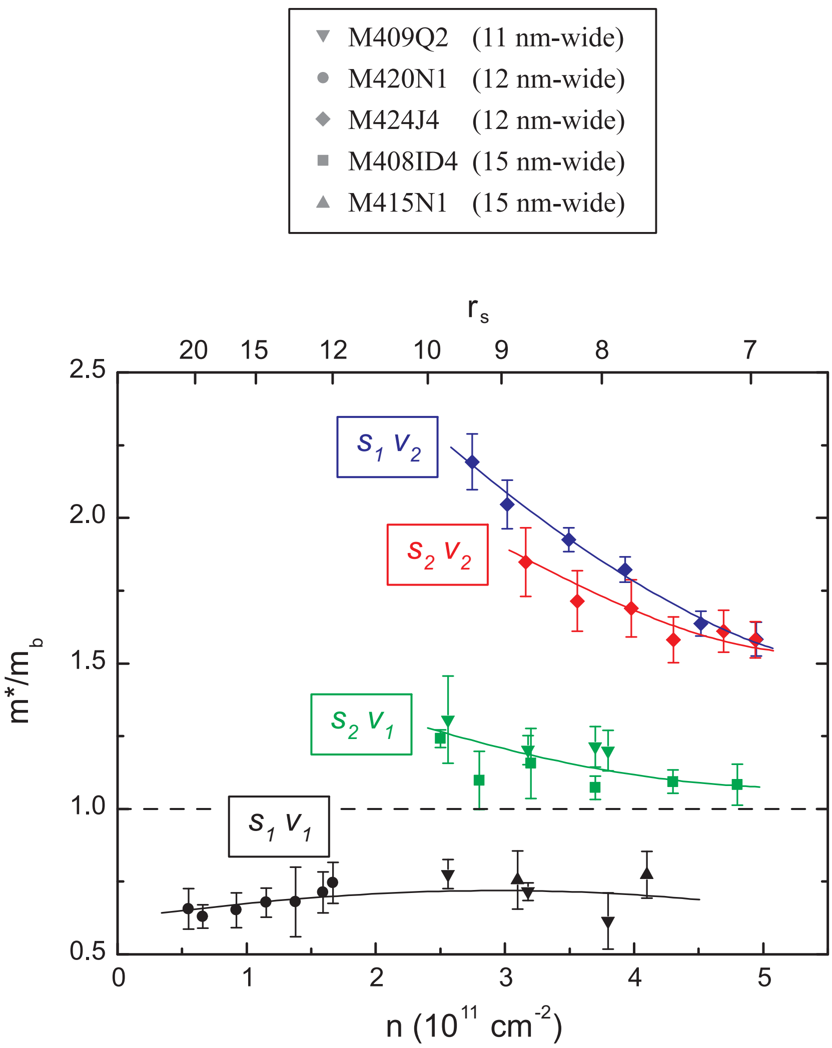

Figure 3.7: Density dependence of effective mass, m^*, normalized to the band value, for 2D electrons confined to wide AlAs quantum wells. Data are shown for four possible spin and valley occupations: s_1v_1, s_2v_1, s_1v_2 and s_2v_2. v_2 corresponds $P_v = 0$, whereas s_2 case corresponds to a spin polarization range of $0.14 \leq P_s \leq 0.33$. The curves through the data points are guides to the eye.

plausible since m^* renormalization in an interacting 2DES partly stems from the exchange interaction which depends on the spin and valley degrees of freedom. Several features of our data are noteworthy.

1. When the 2DES is fully spin and valley polarized, m^* is significantly reduced, to values below m_b even for r_s up to 21, implying that the exchange interaction is notably different when the spin and valley degrees of freedom are *both* frozen out. The suppression of m^* for a fully spin and valley polarized 2DES was a surprise initially and begged for extra experimental evidence and theoretical explanation. We tested the generality of this observed mass suppression in narrow AlAs QWs which we discuss in detail in Chapter 4. In the same Chapter, we also point to two very recent theoretical papers that aim to explain the m^* suppression in a ferromagnetic 2DES.

2. Except for the s_1v_1 case, for all other combinations of spin and valley occupations, m^* is larger than m_b and increases with increasing r_s. This is the trend observed in other 2DESs where either two valleys or spins are occupied [44; 45; 46; 47; 48; 50]. However, an interesting feature of our data is the marked contrast between the spin and valley degrees of freedom: When electrons occupy two spin subbands, m^* depends on the valley occupation, but not vice versa. The data reveal that the spin and valley degrees of freedom are not equivalent in this system. We present further discussion of the discrepancy between the spin and valley degrees of freedom, including the susceptibility data, in Chapter 5.

Chapter 4

Effective mass of 2D electrons in narrow AlAs quantum wells

4.1 Introduction

In Chapter 3, in addition to r_s, the importance of spin and valley degrees of freedom in m^* renormalization was explored in 2DESs confined to wide AlAs QWs. The results summarized in Chapter 3 show that when the 2DES is partially spin-polarized or partially valley-polarized, the measured m^* is larger than m_b, consistent with most previous reports on other 2DESs. However, an unexpected trend is observed as the system becomes fully spin and valley polarized: m^* is suppressed and falls to values near or below m_b even for r_s values up to 21.

To test the generality of this observed mass suppression, in this Chapter we repeat measurements of m^* in the partially and fully spin polarized regime as a function of density in a 2DES where the electrons are confined to a narrow AlAs QW. As we discussed in detail in section 2.2, in a narrow AlAs QW, the electrons occupy a single, out-of-plane valley with an *isotropic* Fermi contour and *isotropic* $m_b = m_t = 0.205$.

This is in contrast to samples studied in Chapter 3 where the electrons are confined to wide AlAs QWs and occupy one or two in-plane valleys with an *anisotropic* Fermi contour and anisotropic band masses equal to 0.205 and 1.05, leading to $m_b = \sqrt{m_l m_t}$ = 0.46. Despite these differences, the m^* measurements in narrow AlAs QWs are consistent with the results of wide AlAs QWs: When the 2DES is partially spin-polarized, m^* is larger than its band value and gradually increases with increasing r_s (decreasing density). But once we fully spin polarize the 2DES by subjecting it to strong magnetic fields, m^* is suppressed down to values near the band mass. Given that the 2DES in narrow AlAs QW is close to an ideal 2DES in the sense that it has a very small layer thickness and an isotropic Fermi contour, it appears that mass suppression for a single-component (fully spin and valley polarized) system is a genuine property of interacting 2DESs.

We performed measurements on a sample (M434R1) where electrons reside in a 4.5 nm-wide AlAs QW. Details of our sample preparation are given in section 2.3. The density of 2D electrons was varied in the range of 1.07 to 4.9 $\times$ 10^{11} cm^{-2}, with low-temperature mobilities μ = 14 to 49$\times 10^3$ cm^2/Vs. Using the AlAs dielectric constant of 10 and the band effective mass $m_b = 0.205$, our density range corresponds to $3.1 < r_s < 6.7$.

4.2 Temperature dependence of Shubnikov de Haas oscillations

To deduce m^*, we analyzed the T-dependence of the strength of the SdH oscillations using the standard Dingle expression [60; 61] given in Eqs. 3.1 and 3.2. We analyzed our data using the two methods described in section 3.2. In the first method, we assumed that both R_o and τ_q are T-independent. In the second method, we included the T-dependence of R_o, and assumed that the relative T-dependence of τ_q is equal to half the relative T-dependence of R_o.

In Figs. 4.1 to 4.4 we present representative data for various spin polarizations. Figure 4.1 shows data for the partially spin polarized case at a relatively high density, $n = 3.93 \times 10^{11}$ cm^{-2}. The angle θ is set carefully so that the opposite spin levels are at coincidence as shown in the left inset of Fig. 4.1. Consistent with this energy level diagram, in the magnetoresistance traces shown in Fig. 4.1, resistance minima at odd ν are strong while the minima at even ν are entirely absent. By fitting the amplitude of the SdH oscillations near $\nu = 11$ to the Dingle expression and assuming T-independent τ_q and R_o, we obtain $m^* = 1.46m_b$ (see Fig. 4.1 right inset). Moreover, as illustrated in the Dingle plot in Fig. 4.5(a), in the whole temperature and magnetic field range the data set can be fit to the Dingle expression by assuming two constants τ_q and m^*. Since the background resistance in this case has a very small temperature dependence, our second analysis method that assumes T-dependent τ_q and R_o yields essentially the same m^*.

In Fig. 4.2 we show data at the density of 2.38×10^{11} cm^{-2}, at a very high tilt angle, $\theta = 80.1°$. At this θ, the magnetoresistance traces initially show a rise with magnetic field because of the loss of screening with increasing spin polarization [67; 68]. The 2DES becomes fully spin polarized above $B_{tot} \cong 11$ T, and the resistance minima at $2 \leq \nu \leq 5$ are clearly observed. Note that at this angle, the lowest five Landau levels are spin polarized as indicated by the energy level diagram shown in Fig. 4.2 left inset. To measure the fully spin polarized m^* we fit the amplitude of the

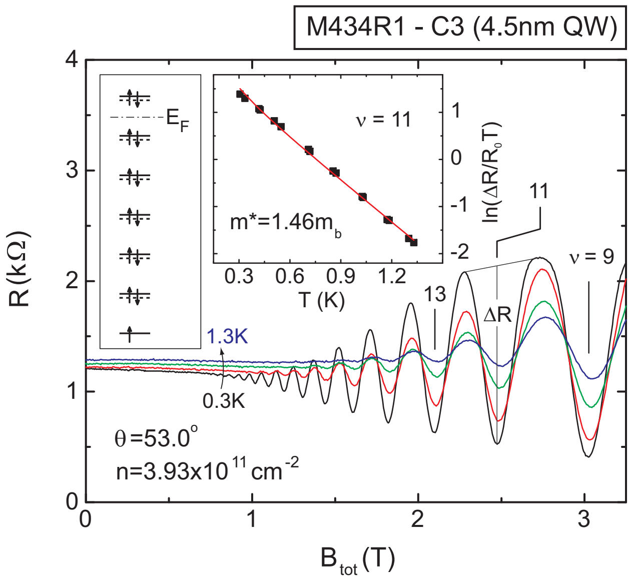

Figure 4.1: Magnetoresistance traces at a density of 3.93×10^{11} cm^{-2} and $\theta = 53.0°$. The traces were taken at $T \cong 0.34$, 0.71, 1.03 and 1.30 K. Insets show the energy level diagram at this tilt angle (left) and the Dingle fit at $\nu = 11$ assuming a constant τ_q and R_o (right).

SdH oscillations near $\nu = 3$ to the Dingle expression by assuming T-independent τ_q and R_o, and we deduce $m^* = 0.97m_b$ (see Fig. 4.2 right inset). As is apparent from the magnetoresistance traces, although at zero field there is a considerable change in resistance with temperature, the background resistance at the SdH oscillation near $\nu = 3$ is small. Therefore including the T-dependence of R_o in the analysis does not make much difference and our first and second analysis methods give essentially identical results.

Next we present data at a lower density ($n = 1.52 \times 10^{11}$ cm^{-2}) where temperature dependence of the background is strong. Figure 4.3 shows data for the partially spin polarized case for this density. Consistent with the energy level diagram in the right inset of Fig. 4.3, θ is set to the coincidence angle so that the resistance minima at odd ν are strong while the minima at even ν are either entirely absent or are accompanied

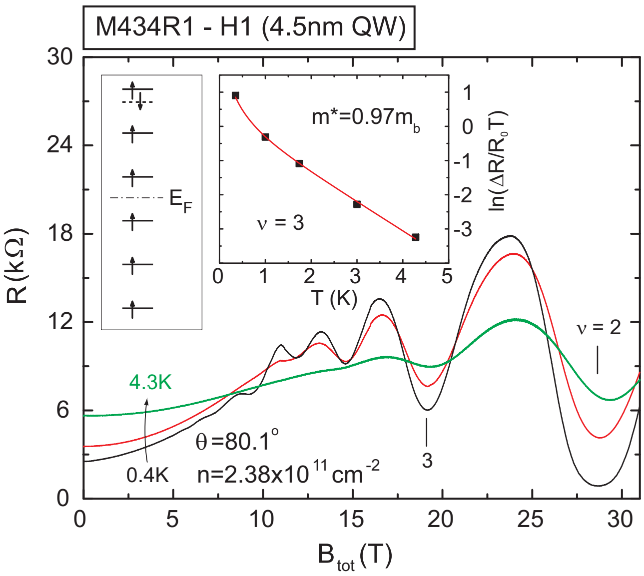

Figure 4.2: Magnetoresistance traces at a density of 2.38×10^{11} cm^{-2} and $\theta = 80.1°$. The traces were taken at $T \cong 0.35$, 1.74 and 4.28 K. Insets show the energy level diagram at this tilt angle (left) and the Dingle fit at $\nu = 3$ assuming a constant τ_q and R_o (right).

by a spike (e.g., at $\nu = 2$) [66]. By fitting the amplitude of the SdH oscillations near $\nu = 5$ to the Dingle expression and assuming T-independent τ_q and R_o, we obtain m^* $= 1.56m_b$ (see Fig. 4.3 left inset). The Dingle plot for this data set is also shown in Fig. 4.5(b). It is apparent from the quality of the fit that single τ_q and m^* can explain the whole data set in the given temperature and magnetic field range. However, as discussed before, the quality of the fit does not justify the assumption of τ_q being T-independent. In addition, as can be seen from the magnetoresistance traces in Fig. 4.3, R_o changes with T by as much as 50% in the indicated temperature range, implying that τ_q can also be T-dependent. Applying our second analysis method, i.e., including the T-dependence of R_o and assuming a T-dependent τ_q that changes by 25% in the same temperature range, we deduce $m^* = 1.44m_b$.

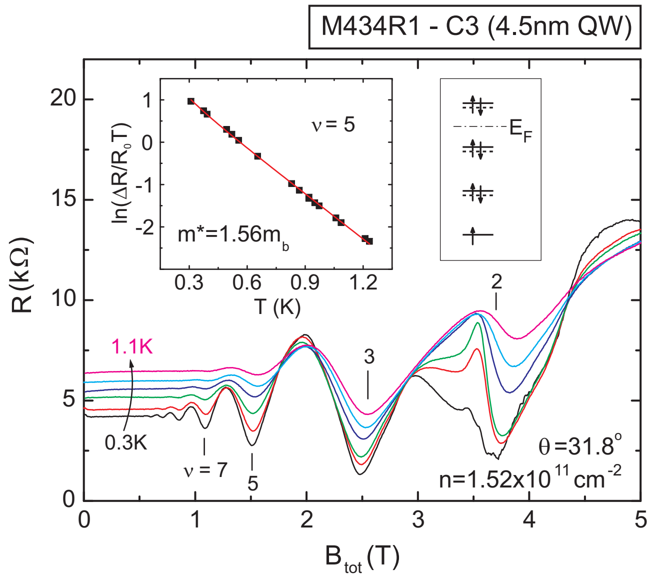

Figure 4.3: Magnetoresistance traces at a density of 1.52×10^{11} cm^{-2} and $\theta = 31.8°$. The traces were taken at $T \cong 0.31$, 0.49, 0.65, 0.83, 0.95 and 1.09 K. Insets show the energy level diagram at this tilt angle (right) and the Dingle fit at $\nu = 5$ using a constant τ_q and R_o (left).

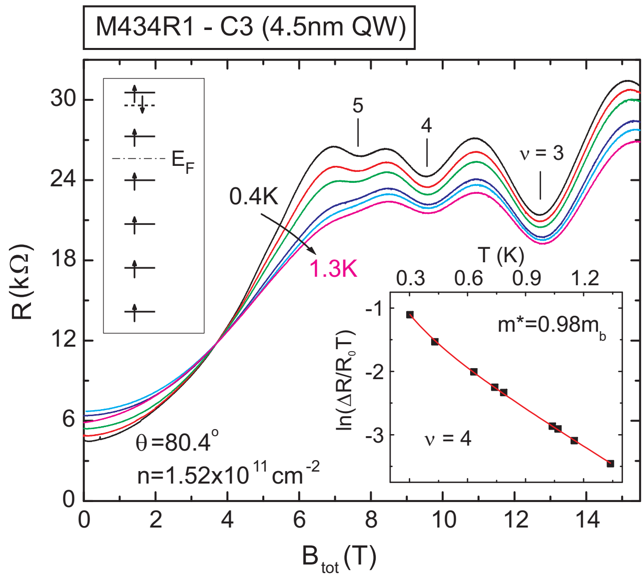

Figure 4.4: Magnetoresistance traces for the same density as in Fig. 4.3 at $\theta = 80.4°$. The traces were taken at $T \cong 0.43$, 0.63, 0.78, 1.07, 1.15 and 1.30 K. Insets show the energy level diagram for this tilt angle (left) and the Dingle fit at $\nu = 4$ using a constant τ_q and R_o (right).

In Fig. 4.4 we show data at the same density as in Fig. 4.3 but at a very high tilt angle, $\theta = 80.4°$. Main features of the data are the same as in Fig. 4.2: Magnetoresistance traces show an initial rise with magnetic field and the 2DES becomes fully spin polarized above $B_{tot} \cong 7$ T. Filling factors $\nu \leq 5$ are in the fully spin polarized regime as indicated by the energy level diagram shown in Fig. 4.4 left inset. To measure the fully spin polarized m^* we fit the amplitude of the SdH oscillations near $\nu = 4$ to the Dingle expression by assuming T-independent τ_q and R_o, and we deduce $m^* = 0.98m_b$ (see Fig. 4.4 right inset). As can be seen from the magnetoresistance traces, the 2DES goes through a metal-insulator transition at $B_{tot} \cong 3.7$ T before the electrons become fully spin polarized [48]. The background resistance around $\nu = 4$ therefore has an insulating behavior. Again using our second method, i.e., including the T-dependence of R_o and assuming a T-dependent τ_q that is half as large as the T-dependence of R_o, we deduce $m^* = 1.11m_b$.

4.3 Density dependence of effective mass

We analyzed data at various ν at several densities. Our results are summarized in Fig. 4.6, where each data point represents m^* averaged over different ν, and the error bar includes the variation of m^* with ν. The results from the first and second analysis methods are shown in black and red in Fig. 4.6, respectively. At high densities where the background is T-independent, the two methods yield essentially identical results. However, as the density of the 2DES is lowered, the T-dependent background becomes stronger and the two methods give slightly different masses. Independently of the method we use, our conclusions remain the same: In the partially spin polarized case (open symbols) m^* is enhanced over m_b and increases with decreasing density, while

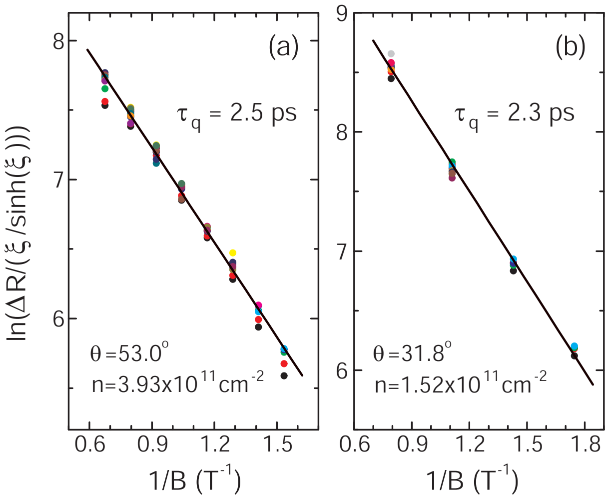

Figure 4.5: Dingle plots of $\Delta R/(\xi/sinh(\xi))$ vs. $1/B$ summarizing data taken on sample M434R1 for the partially spin polarized case for: (a) a density of 3.93×10^{11} cm^{-2} in the range $0.3 \leq T \leq 1.3$ K and $11 \leq \nu \leq 25$; and (b) a density of 1.52×10^{11} cm^{-2} in the range $0.3 \leq T \leq 1.1$ K and $5 \leq \nu \leq 11$.

for the fully spin polarized case (closed symbols) m^* values are clearly suppressed compared to the partially spin polarized case and are very close to m_b. In our study, the "partially-spin-polarized" regime corresponds to spin polarization ranging from $0.04 \leq P_s \leq 0.20$.

We note that the partially spin polarized masses are also reported in Ref. [48]. However those masses are not deduced at the coincidence condition. Setting the coincidence condition is important because when the spin-up and spin-down levels do not overlap, the gap is smaller than the cyclotron energy and one may deduce artificially larger values for m^*.

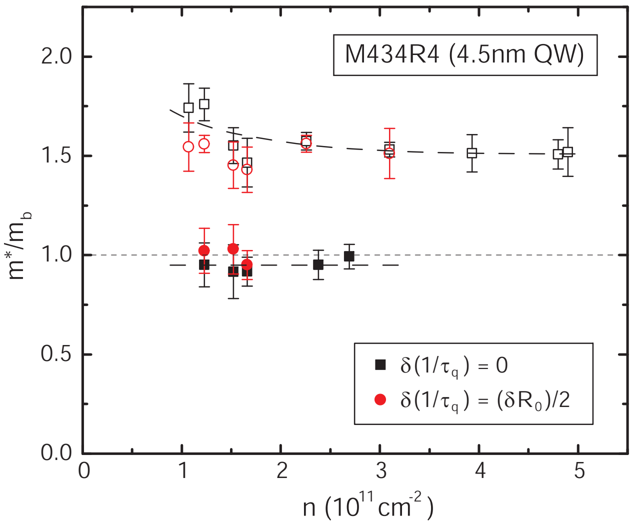

Figure 4.6: Effective mass, normalized to the band mass, measured as a function of density for a 2DES confined to a 4.5 nm-wide AlAs quantum well. Open and closed symbols represent m^* measured in partially and fully spin-polarized 2DESs, respectively. Black and red points correspond to m^* values deduced either assuming a constant quantum lifetime τ_q or that the relative temperature-dependence of τ_q is half the size of the relative temperature-dependence of the background resistance, respectively. Each data point represents m^* averaged over different Landau level filling factors, ν, and the error bars include the variation of m^* with ν. The dashed curves through the data points are guides to the eye.

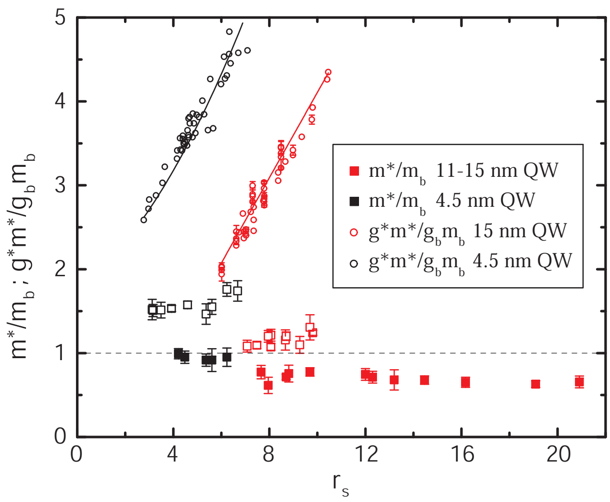

Figure 4.7: Normalized effective mass and spin susceptibilities of both narrow and wide AlAs quantum wells as a function of the interaction strength, r_s. Black and red circles are g^*m^*/g_bm_b of 4.5 nm and 15 nm-wide AlAs quantum wells taken from Refs. [48] and [42], respectively. Open and closed red squares are m^*/m_b for a single valley 2DES confined to 11 to 15 nm-wide AlAs quantum wells in partially and fully spin polarized regime, respectively. Black squares are m^*/m_b data for a 2DES confined to 4.5 nm-wide AlAs quantum well.

4.4 Comparison with 2D electrons in wide AlAs quantum wells

As a summary plot, in Fig. 4.7 we show the normalized effective mass and the spin susceptibilities of both narrow and wide AlAs QWs as a function of interaction strength, r_s. Black and red circles are the normalized spin susceptibilities of 4.5 nm and 15 nm-wide AlAs QWs, taken from Refs. [48] and [42], respectively. Open and closed red squares represent m^*/m_b for partially and fully spin polarized system, respectively, for a single-valley 2DES confined to wide AlAs QWs from Fig. 3.7. Black squares are the measured m^* data for a 2DES confined to a narrow AlAs QW from Fig. 4.6.

In an ideal 2DES, the normalized values of the spin susceptibility and effective mass each should follow a universal curve as a function of r_s [35; 36]. However non-ideal factors such as finite layer thickness, anisotropy of the Fermi contour, and disorder give non-universal corrections. Although for high quality samples the effect of disorder is small [37; 38], finite layer thickness and anisotropy of the Fermi contour modify the interaction significantly [38; 41; 42] and change the spin susceptibility and the effective mass renormalization. Because of the small layer thickness and isotropic Fermi contour of the electrons in narrow AlAs samples, the spin susceptibility follows very closely the predictions of quantum Monte Carlo calculations for an ideal 2D system (not shown) [30; 35; 38; 48]. However, for wide AlAs samples the measured susceptibilities are considerably lower than for narrow AlAs samples because the strength of the Coulomb interaction is reduced by the finite layer thickness effect [38; 41] and the anisotropy of the Fermi contour [42].

It is clear from the data that the partially spin polarized masses for wide AlAs QWs are also smaller than for narrow AlAs QWs even though the r_s values are larger. Similar to the spin susceptibility case [42], the corrections to m^* due to the layer thickness and the anisotropic effective mass are expected to give smaller m^* values in the partially spin polarized case [36; 41], consistent with our data. In addition, we emphasize that the mobility of the electrons in narrow QWs is much lower compared to wide QWs because of the prevalence of the interface roughness scattering. Therefore, it is also possible that the higher disorder in narrow QWs is responsible for m^* being larger [37]. We point out that in the partially polarized case there are also some quantitative differences between our results on narrow AlAs QWs and the previous studies done on Si-MOSFETs [45; 46; 47] and GaAs 2DESs [50]. It has been reported that in GaAs 2DESs m^* has a strong r_s dependence although m^* values are much smaller compared to narrow AlAs QWs for the similar r_s range. It is likely that this discrepancy is because of the larger finite layer thickness and less disorder in 2DESs in GaAs samples. On the other hand, a comparison between results for narrow AlAs QWs and Si-MOSFETs is not valid because of the valley degeneracy of Si-MOSFET samples: as discussed in Chapter 3, the valley degeneracy affects the mass renormalization considerably.

In the fully polarized regime, it is natural to also expect some dependence of m^* on the layer thickness, Fermi contour anisotropy and disorder. However, it is not clear from the data whether m^* are lower for wide AlAs samples because of non-ideal factors or because these masses are measured at larger r_s values. We conclude that the mass suppression is very robust and is observed in a very wide range of r_s values and independent of sample and system parameters such as disorder, layer thickness and Fermi contour anisotropy.

4.5 Discussion and Conclusions

It is intuitively clear that the spin polarization of the 2DES should affect the m^* renormalization since it modifies the exchange interaction. Naively, one might think that for a fully spin polarized system the Fermi energy is doubled so the interaction is weaker compared to the spin unpolarized case, and hence the mass for the spin polarized case would be smaller. Although this argument gives the correct qualitative behavior of m^* for a fixed density, it does not explain why m^* for the fully polarized system stays small (near or below m_b) even at very high r_s values. It is reported in Ref. [39] that m^* very weakly depends on the spin polarization for valley degenerate systems. We emphasize that we observe the mass suppression in a single-valley and fully spin polarized system and therefore this study is not relevant to our data. A more relevant study [40], which deals with a single-valley system, reports a rather strong dependence of m^* on the degree of spin-polarization. Although it is predicted in Ref. [40] that for a fully spin polarized 2DES m^* is smaller compared to the spin unpolarized case, there remain major qualitative discrepancies with our data. For example, m^* for a fully spin polarized system is predicted to increase with increasing r_s and become smaller than m_b only for $r_s < 2$. In contrast, our data suggest that m^* stays very close to m_b even in the range $4 < r_s < 6$. Including the m^* data for wide AlAs QWs, which extends up to $r_s \simeq 21$, the discrepancy becomes even more serious.

Motivated by our experimental data, a recent theoretical work [69] has addressed the m^* renormalization in a ferromagnetic 2DES. Their calculations show that within the random phase approximation, which does not take the multiple scattering processes into account, m^* is always enhanced in the strong coupling limit ($r_s > 3$). However, when the multiple scattering processes are taken into account, indeed, the effective mass is significantly suppressed compared to the band value in the fully polarized case because of the absence of spin fluctuations. Results of another recent theoretical study done by the diffusion quantum Monte Carlo method [70] also confirm the observed mass suppression in a ferromagnetic 2DES.

In summary, our data presented in Chapters 3 and 4 suggest that mass suppression for a single component system is a general property of an interacting 2DES. Indeed, our experimental results have been confirmed by theoretical studies of Refs. [69] and [70].

Chapter 5

Contrast between spin and valley degrees of freedom

In this Chapter, we present a contrast between the spin and valley degrees of freedom revealed in the renormalization of effective mass (m^*), effective Lande g-factor (g^*) and conduction-band deformation potential (E_2^*) in wide AlAs QWs.

Through controlling the valley occupation in wide AlAs QWs, the dependence of spin susceptibility ($\chi_s^* \propto g^* m^*$) on the valley degree of freedom was studied in Refs. [49; 59]. The measurements revealed that χ_s^* is smaller for a two-valley system than it is for a single-valley system. This unexpected result was subsequently explained by theoretical studies [41; 71; 72]. The valley susceptibility ($\chi_v^* \propto E_2^* m^*$) of AlAs 2DESs, defined as the rate of valley polarization with applied strain (in analogy to χ_s^* which is defined as the rate of spin polarization with applied magnetic field), has also been measured [59]. It was found that χ_v^* depends on the spin subband occupation [63] in a similar way that χ_s^* depends on the valley occupation. This observation is consistent with the expectation from theories which treat spin and valley as equivalent degrees of freedom [71; 72].

The m^* measurements presented in Chapter 3, however, reveal that the spin and valley degrees of freedom are not equivalent in wide AlAs QWs. Combining our m^* data with the measured spin and valley susceptibilities, here we deduce values for the renormalized effective Lande g-factor and renormalized conduction-band deformation potential. The discrepancy between the spin and valley degrees of freedom persists in g^* and E_2^* renormalization as well.

Here is a summary of data discussed in this Chapter:

1. As seen in Fig. 3.7, for a system where electrons reside in two spin subbands, m^* for the two-valley case is larger than m^* for the single-valley case. However, when the electrons reside in two valleys, m^* does not depend on the spin occupation. In other words, $m^*_{s_1v_2} > m^*_{s_2v_1}$.

2. As reported before [49; 59; 63], the dependence of $\chi_s^* \propto g^*m^*$ on valley occupation is similar to the dependence of $\chi_v^* \propto E_2^*m^*$ on spin subband occupation, namely, χ_s^* for v_1 is larger than for v_2, and χ_v^* for s_1 is larger than for s_2 (Fig. 5.1). Combining our m^* data with the measurements of g^*m^* and $E_2^*m^*$ done in the same system, we also deduce values for g^* and E_2^* for different valley and spin occupations (Fig. 5.1). Deduced g^* values are smaller for the v_2 case compared to the v_1 case. However, the deduced E_2^* values are independent of the spin occupation, i.e., they are the same for s_2 and s_1.

5.1 Effective mass data

We show the summary of our m^* measurements as a function of density for different valley and spin occupations in Fig 3.7. The unexpected suppression of m^* for a

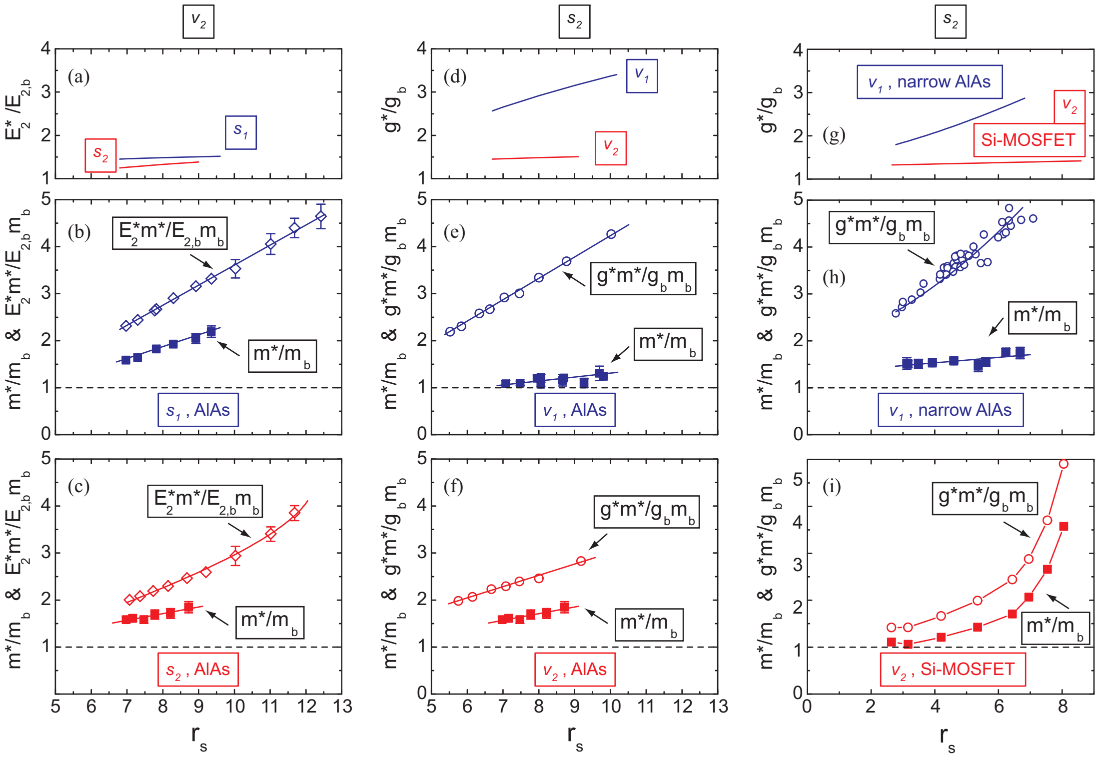

Figure 5.1: Effective mass (m^*, squares), valley susceptibility ($E_2^* m^*$, diamonds), and spin susceptibility ($g^* m^*$, circles) are shown as a function of r_s in the lower six panels. The upper three panels show E_2^* and g^* deduced from the m^* and susceptibility data. The left and central panels contain data for wide AlAs quantum wells for the different combinations of valley and spin occupations as indicated, e.g., in (b) data for $s_1 v_2$ are shown. Note that in wide AlAs quantum wells the electrons occupy one or two in-plane valleys with *anisotropic* Fermi contours. The right panels present data for 2D electrons in Si-MOSFETs (Ref. [46]) where two out-of-plane valleys are occupied, and in narrow AlAs quantum wells (see Chapter 4) where the electrons occupy a single out-of-plane valley; note that these out-of-plane valleys have an *isotropic* Fermi contour.

fully spin and valley polarized 2DES was discussed in detail in Chapters 3 and 4. The enhancement of m^* for all other combinations of spin and valley occupations is consistent with the reports on other 2DESs where either two valley or spins are occupied [44; 45; 46; 47; 48; 50]. In this Chapter, we elaborate the contrast seen in Fig. 3.7 between the data for s_1v_2 and s_2v_1 cases: *m^* is much larger for s_1v_2 compared to s_2v_1*. Moreover, the data reveal that when two valleys are occupied, m^* shows only a slight dependence on the spin occupation, whereas for s_2, m^* for v_1 is much smaller than it is for v_2.

The role of spin polarization on m^* renormalization has been addressed theoretically [39], and it was concluded that m^* is independent of the spin polarization for a valley degenerate (v_2) 2DES. This conclusion is in agreement with our data and also with the data for 2DESs in Si-MOSFETs [47]. If the valley and spin degrees of freedom were identical, one would expect similar m^* values when s and v are interchanged, meaning that m^* should not depend on valley occupation when two spins are occupied. Our data of Fig. 3.7 clearly contradict this expectation: $m^*_{s_2v_1}$ is almost a factor of 2 smaller than $m^*_{s_2v_2}$. Evidently in our 2DES the spin and valley indices are not alike in the determination of m^*.

5.2 Effective g-factor and deformation potential data

Next we discuss the contrast between spin and valley degrees of freedom that is revealed in the measurements of g^* and E_2^*. The values of spin and valley susceptibilities, $\chi_s^* \propto g^*m^*$ and $\chi_v^* \propto E_2^*m^*$, were measured as a function of r_s and at different valley and spin subband occupations via "coincidence" measurements [49; 59; 63]. In such measurements, the valley and spin splitting energies are tuned very carefully so that two Landau levels corresponding to different spins or valleys coincide at the Fermi energy. The coincidence is signaled by a maximum in the resistance at integer filling factors where, in the absence of the coincidence, a minimum is expected as the Fermi energy resides in a gap between two energy levels. From the values of strain and tilt angle at which such coincidences occur, we deduce the Zeeman- and/or the valley-splitting energies normalized to the cyclotron energy. These energies directly give g^*m^* and $E_2^*m^*$. Combining the measured g^*m^* and $E_2^*m^*$ with the m^* data, we deduce values for g^* and E_2^* which we also show in Fig. 5.1 (upper panels).

There are several remarkable features in Fig. 5.1 data. Focusing on Figs. 5.1(b) and (e), or (c) and (f), we note that $E_2^*m^*$ and g^*m^* are increasingly enhanced over their band values as r_s is increased, as expected in an interacting electron picture. The numerical values of $E_2^*m^*$ and g^*m^* for different spin and valley occupations are close despite the fact that they represent the system's response to very different external stimuli: $E_2^*m^*$ measures the rate of valley polarization with strain while g^*m^* is the rate of spin polarization as a function of applied magnetic field. This observation suggests the similarity between spin and valley as two discrete degrees of freedom. However, when we combine the measurements of $E_2^*m^*$ and g^*m^* with the corresponding m^* data and deduce the values of E_2^* and g^* for different spin and valley occupations (Figs. 5.1(a) and (d)), the contrast between spin and valley becomes apparent. For v_2 (Fig. 5.1(a)), E_2^* is enhanced over the band value and shows a slight increase with r_s but does not show much dependence on spin subband occupation. In contrast, for s_2, Fig. 5.1(d) reveals that g^* has a strong dependence on the valley occupation: although g^* is enhanced over the band value and increases with r_s, g^* for v_1 is much larger than it is for v_2. We highlight a noteworthy feature of Fig. 5.1 data: m^*, g^*, and E_2^* reveal a clear contrast between spin and valley degrees of freedom while g^*m^* and $E_2^*m^*$ do not. It appears as if m^*, g^* and E_2^* conspire to make the susceptibilities g^*m^* and $E_2^*m^*$ behave similarly!

Theoretically, if spin and valley are considered only as discrete degrees of freedom, then they are indistinguishable. Why is this not so in our 2DES? In AlAs 2DES the spin and the valley indices are not identical. The two valleys in wide AlAs QWs have *anisotropic* Fermi contours whose major axes are rotated by 90 degrees with respect to each other. Therefore, the interaction between electrons that have the same valley but different spin index might be different from that between electrons that have the same spin but different valley index. To examine this possibility, we describe here experimental data in two other 2DESs, namely those confined to either a narrow AlAs QW or to a Si-MOSFET. In a *narrow* AlAs QW, the electrons occupy a single valley with its major axis pointing out of plane and an in-plane *isotropic* Fermi contour, while in a Si-MOSFET they occupy two such valleys [47].

The data for these two systems are summarized in the right panels of Fig. 5.1. Note that these data correspond to s_2 and should be compared to the data shown in the central panel of Fig. 5.1. Such comparison reveals that overall trends are qualitatively similar. In particular, in the Si-MOSFET case (Fig. 5.1(i)) where we have v_2, enhancements of g^*m^* and m^* track each other so that the deduced g^* appears only slightly enhanced and its enhancement has a very weak dependence on r_s (Fig. 5.1(g)). This is very similar to what is seen in Fig. 5.1(d) for the wide AlAs v_2 case. In the narrow AlAs QW (Fig. 5.1(h)) where we have v_1, on the other hand, the

g^*m^* enhancement is much larger than the m^* enhancement and it grows faster with r_s. The deduced g^* therefore exhibits a significant and r_s dependent enhancement (Fig. 5.1(g)), similar to the v_1 case for the wide AlAs QW (Fig. 5.1(d)). We conclude that the contrast between the valley and spin degrees of freedom is not because of the Fermi contour anisotropy and might have a more intrinsic origin.

There are other non-ideal factors such as finite layer thickness and disorder which can give non-universal corrections to the renormalization of m^* (and susceptibilities) [37; 38; 41]. Finite layer thickness softens the Coulomb interaction but cannot cause a difference between spin and valley degrees of freedom. In our measurements, we apply parallel magnetic field ($B_\parallel$) to fully spin polarize the 2DES or to tune the (Landau) energy levels. In a 2DES with finite electron layer thickness, $B_\parallel$ couples to the orbital motion of the electrons and leads to an increase of m^* [64]. However, because of the very small electron layer thickness in our AlAs samples ($\leq$ 15 nm), we expect that this increase is less than 5% even at $B_\parallel = 15$ T.

As for disorder, its effect of on m^* has been studied theoretically [37], and it has been concluded that m^* is larger when impurity scattering is taken into account compared to a clean system. We speculate that the difference between the valley and spin we observe might come from the differences in scattering mechanisms between states with opposite spins or valleys. A scattering event requires the conservation of total spin and momentum. An electron scattering from one valley to another requires a large momentum transfer because the valleys are located near the edges of the Brillouin zone. However, an electron scattering from one spin to another within the same valley requires a small momentum transfer (on the order of the Fermi wave-vector) and some magnetic impurity to conserve the total spin. It is possible that these scattering mechanisms are different in the presence of interaction and disorder. An understanding of the contrast between spin and valley degrees of freedom in m^*, g^* and E_2^* renormalization awaits future theoretical developments.

Chapter 6

Transference of transport anisotropy to composite fermions

The question of how the properties of the underlying particles affect the behavior of the emergent particles is of paramount interest in physics. The system of composite fermions (CFs), complex electron-flux bound states that experience an effective magnetic field, offers an elegant example where this question can be addressed in various contexts. The CF formulation provides a powerful description of interacting two-dimensional (2D) electrons at high perpendicular magnetic fields [24; 25; 26]. In particular, at a half-filled Landau level (LL), where the effective magnetic field vanishes, the CFs exhibit Fermi-liquid-like properties, similar to their zero-field electron counterparts. Interestingly, however, the Fermi energy and the effective mass of CFs, being determined solely by interactions, should possess no memory whatever of the Fermi energy and the band mass of the electrons. That raises a fundamental question: Does an anisotropy of the electron effective mass and Fermi surface survive composite fermionization? Here we address this question by measuring the resistance of CFs in AlAs QWs where the electrons occupy an elliptical Fermi surface with large eccentricity and anisotropic effective mass.

In this Chapter, we present piezoresistance measurements of CFs at $\nu = 1/2$ and 3/2 in comparison with the piezoresistance of electrons at zero field. In section 6.2, we show transport measurements when the current is passed along the [100] direction (major axis of one of the valleys). Our data reveal that, similar to their electron counterparts, the CFs also exhibit anisotropic transport, suggesting an anisotropy of CF effective mass and Fermi surface. In section 6.3, we summarize the transport data when current is passed along the [110] direction (45° with respect to the major axes of the valleys). We also present the temperature dependence of the CF piezoresistance at $\nu = 3/2$ in the same section. Temperature dependent measurements reveal that the resistance of CFs has a metallic temperature dependence for small values of valley polarization but turns insulating as the CFs are driven to full valley polarization. This behavior is also observed for electrons at zero perpendicular magnetic field. The results presented in this Chapter illustrates the similarity between transport properties of electrons and CFs.

6.1 Introduction

Clean two-dimensional electron systems (2DESs) provide one of most fertile grounds for the observation of many-body phenomena in nature. When the 2D system is cooled to low temperatures and placed in high, perpendicular magnetic fields to minimize the electrons' kinetic energy, it exhibits fascinating and often unexpected phenomena originating from electron-electron interaction. Examples include the fractional quantum Hall effect, electron Wigner crystallization, and the formation of spin textures

(Skyrmions) [2; 20; 26]. Two decades ago the CF picture was put forth, initially to describe the fractional quantum Hall effect [24]. The CFs are formed by attaching an even number of magnetic flux quanta to each electron at high magnetic fields (Fig. 6.1). With this transformation, since the attached flux exactly cancels out the external magnetic field at half-filled LLs, the CFs should ignore the very large external magnetic field and behave as if they are at zero field. Such remarkable behavior has indeed been confirmed in various experiments [20; 26]. One particularly fundamental property of CFs at exactly half-filled LLs is that they form a Fermi sea and therefore possess a Fermi surface (FS). This has also been verified in several experiments [20; 26].

A natural question that arises is: In a 2D system with an anisotropic electron effective mass and FS (at zero magnetic field), do the CFs retain such anisotropy? The answer to this question is not obvious. One might argue that, since the CFs are a manifestation of the electron-electron interaction, their physical properties should only depend on the magnitude of the magnetic field which quantifies this interaction, and not on the electrons' zero field ($B = 0$) properties. On the other hand, the interaction could be anisotropic if the effective mass of electrons is anisotropic. In our study, we measure and compare the piezoresistance of electrons at $B = 0$ and of CFs at LL filling factors $\nu = 1/2$ and $3/2$ in a 2DES confined to an AlAs QW. In this system, the electrons can be re-distributed, via the application of strain, between two conduction-band valleys each of which has an anisotropic FS. The piezoresistance of CFs exhibits anisotropic transport, qualitatively similar to the electrons' at $B = 0$.

We note at the outset that in a system with a parabolic energy vs. wave vector dispersion, such as AlAs electrons at $B = 0$, the anisotropies of the effective

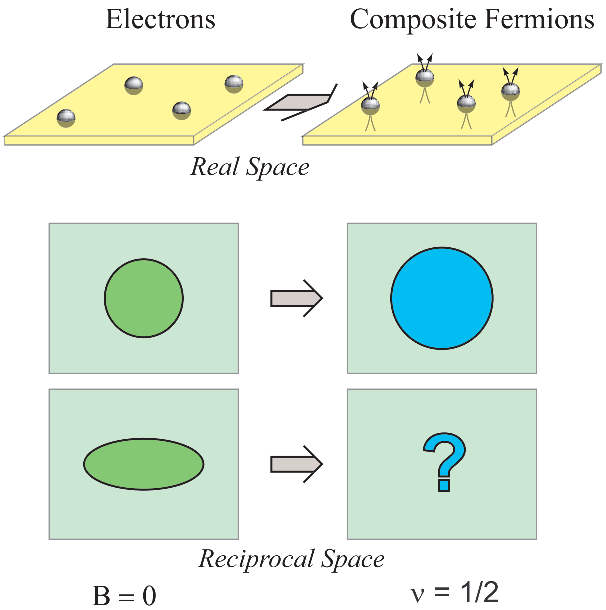

Figure 6.1: Top panel: Schematics of 2D electrons and composite fermions in real space. Lower panels: Schematics of isotropic and anisotropic electron (left) and corresponding composite fermion (right) Fermi surfaces.

mass and the FS are linked. In a simple (Drude) model, the transport anisotropy in such a system is a direct consequence of the effective mass anisotropy and the FS anisotropy which typically leads to an anisotropic scattering time. The applicability of a parabolic dispersion or Drude model to CFs is not clear. We would like to emphasize, however, that our data provide evidence that the transport anisotropy we observe is not merely a consequence of scattering time anisotropy of the CFs, but rather points to an anisotropy of the CF mass and FS.

6.2 Transport along [100]

We made measurements on 2D electrons confined to a 12 nm-wide AlAs QW (sample M424J4). Sample M424J4 had three patterned Hall bar mesas along the [100], [010] and [110] crystal directions. We took data with current along the [100] and [110]; the results summarized in this section are for the [100] arm, and data for the [110] arm are presented in section 6.3. Using a metal gate deposited on the sample's surface we varied the 2D electron density n, between 1.2 and 4.8×10^{11} cm^{-2}. The transport measurements were performed down to a temperature of 300 mK, and up to a magnetic field of 16 T, using low-frequency lock-in techniques.

6.2.1 Magnetoresistance data

In Fig. 6.2(a) we show a resistance (R) vs. magnetic field ($B_\perp$) data at $n = 4.82 \times 10^{11}$ cm^{-2} for a strain of $\epsilon = 1.88 \times 10^{-4}$. In addition to the integer quantum Hall states at low B, well-developed fractional quantum Hall (FQH) states around $\nu = 3/2$ such as $\nu = 5/3$, 4/3, 8/5 and 7/5 can be seen. In Fig. 6.2(b) we show a similar magnetoresistance trace at a lower density, $n = 1.72 \times 10^{11}$ cm^{-2} for $\epsilon = 1.11 \times 10^{-4}$, so that the FQH states around $\nu = 1/2$ are also visible. After determining the density and the positions of $\nu = 1/2$ and 3/2 from magnetoresistance data, we take piezoresistance traces at $\nu = 1/2$, $\nu = 3/2$ and $B = 0$.

6.2.2 Piezoresistance at $\nu = 1/2$

Examples of piezoresistance traces taken at $B = 0$ and at $\nu = 1/2$ are shown in Fig. 6.3. The $B = 0$ data are consistent with the conventional piezoresistance seen in multi-valley semiconductors [73; 74]. The resistance drops for positive values of strain as electrons are transferred to the Y valley whose mobility along the current direction (the [100] direction) is higher because of its smaller effective mass m_t along this direction (Fig. 6.3(f)). For negative values of strain, the resistance rises because

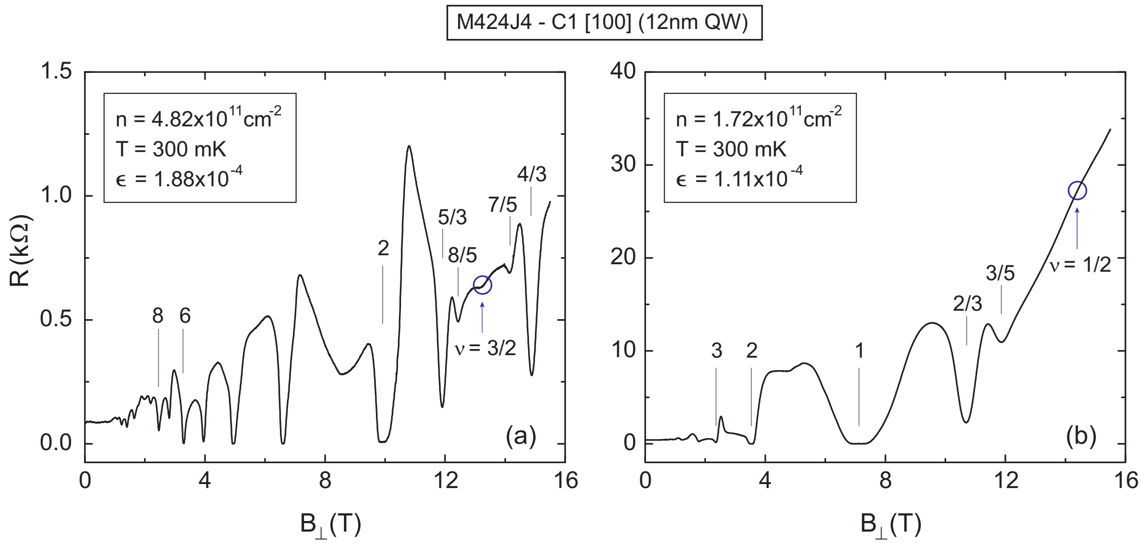

Figure 6.2: Magnetoresistance (R vs. $B_\perp$) traces at (a) $n = 4.82 \times 10^{11}$ cm^{-2} and (b) $n = 1.72 \times 10^{11}$ cm^{-2}.

now the electrons are transferred to the X valley which has a large effective mass along [100] (Fig. 6.3(d)). At large enough values of strain (either positive or negative) the resistance saturates once one of the valleys is completely depleted and inter-valley electron transfer stops. The saturation value of the resistance when all electrons are in X valley is about a factor of 3 larger than the resistance when electrons are in Y valley. This is a direct consequence of the mass and FS anisotropy of the valleys at zero field [30; 75; 76].

Before discussing the $\nu = 1/2$ data shown in Fig. 6.3, we first describe the energy level structure of the 2D system in a perpendicular magnetic field. The magnetic field quantizes the orbital motion of the electrons and forces them to occupy a discrete set of energy levels (LLs) separated by the cyclotron energy, $\hbar\omega_c = \hbar eB/m^*$, where B is the magnetic field and $m^* = \sqrt{m_l m_t}$ is the cyclotron effective mass. In our system, there are four sets of these LLs, one for each spin and valley combination.

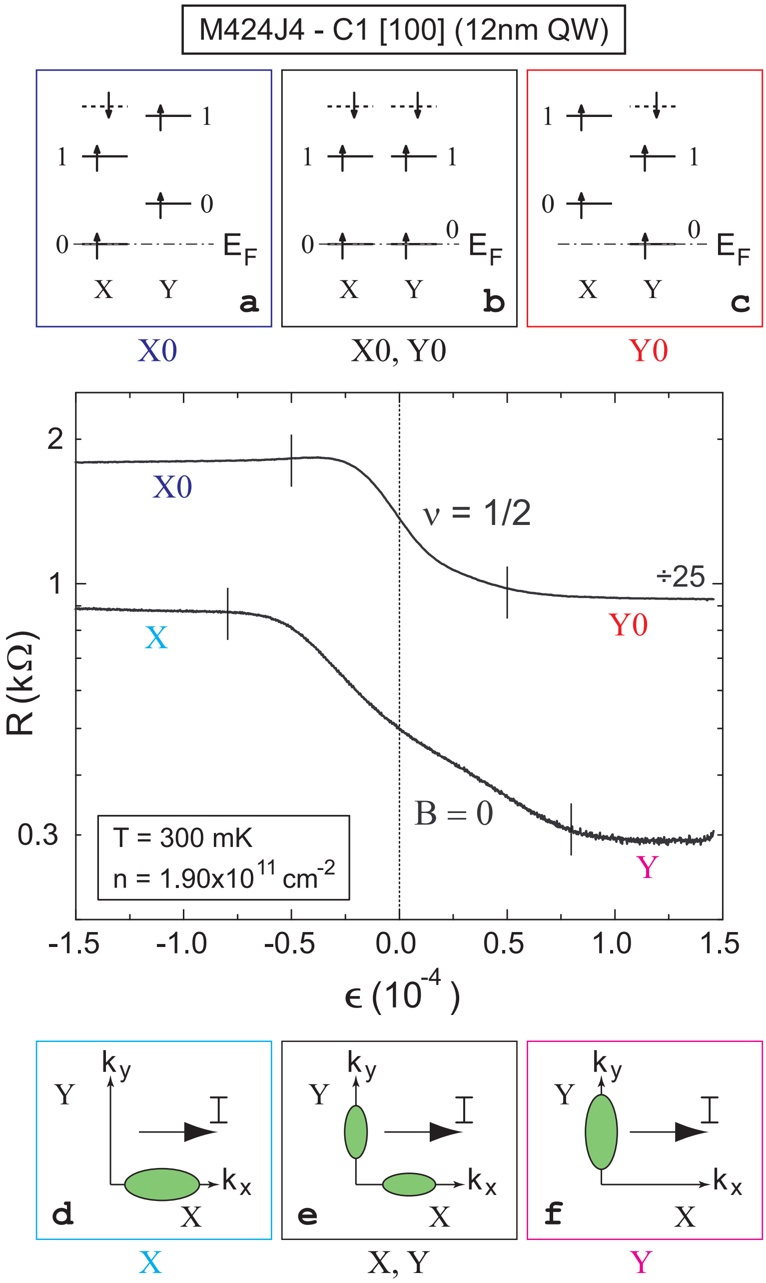

Figure 6.3: Main: The piezoresistance of electrons at $B = 0$ and composite fermions at $\nu = 1/2$ ($B = 15.7$ T) at density $n = 1.9 \times 10^{11}$ cm^{-2}. (a), (b) and (c) Energy level diagrams and the position of the Fermi energy (E_F) for negative, zero, and positive strain at $\nu = 1/2$. (d), (e) and (f) Valley occupations for negative, zero, and positive strain at zero magnetic field.

The energy splitting between oppositely polarized spin levels is given by the Zeeman energy, while the levels corresponding to different valleys are separated by E_V. We label each of the energy levels according to their valley (X or Y), spin ($\uparrow$ or $\downarrow$) and LL index $(0, 1, ..)$. However, for the density range of our study, the parameters for AlAs electrons are such that the Zeeman energy is larger than the cyclotron energy. Therefore, all the LLs that are of concern here ($\nu < 2$) have the same spin.

The piezoresistance trace in Fig. 6.3 taken at $\nu = 1/2$ qualitatively shows a very similar behavior to the $B = 0$ trace. The resistance decreases (increases) towards positive (negative) values of strain and at high enough strains it saturates. For very negative values of strain, the $\nu = 1/2$ CFs form in the lowest LL of the X valley, namely X0 (Fig. 6.3(a)). For very positive values of strain, the CFs are transferred to the lowest LL of the Y valley, i.e., Y0 (Fig. 6.3(c)). If the CF mass and FS were both isotropic, we would expect to observe a symmetric piezoresistance as the resistance should be the same whether the CFs are either in X0 or Y0. The asymmetry of the piezoresistance at $\nu = 1/2$ therefore indicates that the CFs qualitatively retain the anisotropy of $B = 0$ electrons.

The evolution of the piezoresistance at $\nu = 1/2$ as function of density is shown in Fig. 6.4. We note that at low densities the piezoresistance at $\nu = 1/2$ becomes non-monotonic and develops a peak near zero strain. The reason for this peak is most likely the extra resistance caused by inter-valley scattering when two valleys are occupied. This extra resistance is absent when CFs occupy a single valley and therefore, the resistance of CFs formed in either X0 or Y0 for large values of strain is not affected by the inter-valley scattering.

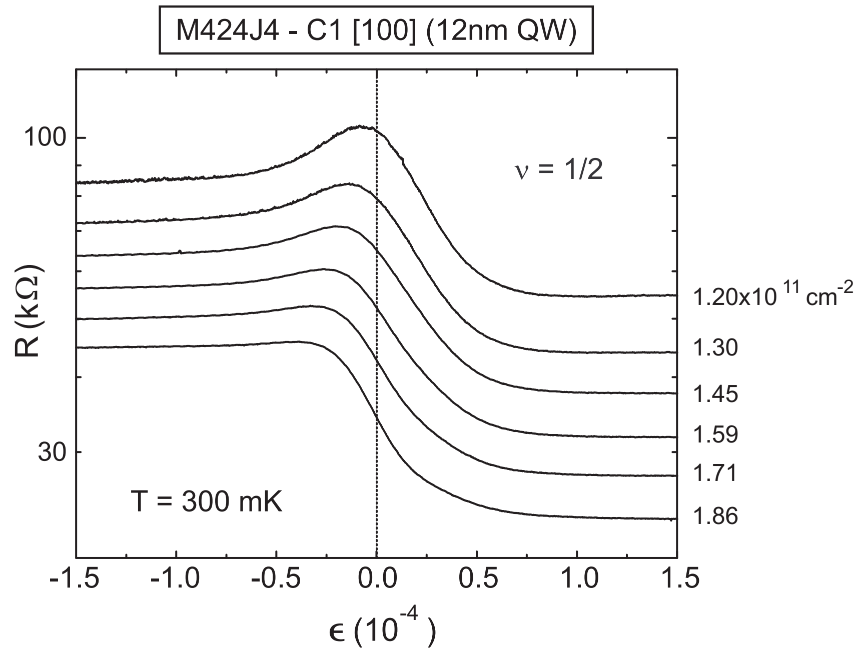

Figure 6.4: The piezoresistance of composite fermions at $\nu = 1/2$ for several densities. The density for each trace is given near it in units of 10^{11} cm^{-2}.

Although the piezoresistance traces at $B = 0$ and $\nu = 1/2$ are qualitatively very similar, there are two important quantitative differences. First, as can be seen in Fig. 6.3, at $\nu = 1/2$ the resistance changes and saturates with strain more quickly compared to $B = 0$. This is because, as reported previously, the (valley splitting) energy required to fully polarize the CFs is smaller than the energy needed to valley polarize the electrons [77; 78; 79]. Second, in the density range of $1.2 - 1.9 \times 10^{11}$ cm^{-2} the resistance value when $\nu = 1/2$ CFs are formed in X0 is only a factor of 1.5 to 2 larger than the resistance value when CFs are formed in Y0. This resistance ratio of CFs (r_{CF}) is about a factor of two smaller than the resistance ratio of electrons (r_e) at $B = 0$. We will return to this difference later in the Chapter.

6.2.3 Piezoresistance at $\nu = 3/2$

The piezoresistance traces measured at $\nu = 3/2$, while more subtle, provide additional, strong evidence for the anisotropy of CF mass and FS. Data taken for a range of densities are shown in Fig. 6.5. The $\nu = 3/2$ data reveal remarkably more features than the $B = 0$ or $\nu = 1/2$ data. Instead of changing monotonically with strain and showing only one transition, the piezoresistance traces at $\nu = 3/2$ exhibit a non-monotonic behavior with strain, suggesting multiple transitions. The other striking feature of the piezoresistance at $\nu = 3/2$ is that for small values of strain (near zero) it shows the opposite trend compared to the $B = 0$ and $\nu = 1/2$ data: The resistance increases with increasing strain, instead of decreasing. As we will discuss below, all of these features can be understood in the context of CFs with an anisotropic mass and FS.

In Fig. 6.5, the $\nu = 3/2$ piezoresistance traces show four regions, highlighted in yellow, where the resistance stays constant for certain ranges of strain which depend on the 2D density. These provide the key to understanding the data. The regions are labeled by X0, Y0, X1, and Y1, indicating the energy level in which the Fermi energy (E_F) resides. Note that the X0 and Y0 regions become narrower and get closer to each other as the density is lowered. Also, given the range of strain accessible in our experiments, we can observe the regions X1 and Y1, where the resistance saturates, only at the lowest densities.

In Fig. 6.6, we focus on the piezoresistance trace at $\nu = 3/2$ at a density of 4.51×10^{11} cm^{-2}. The opposite trend of the piezoresistance near zero strain compared to the $B = 0$ or $\nu = 1/2$ data is obvious. At $B = 0$, positive strain pushes the X valley up in energy and electrons are transferred from the X valley to the Y valley.

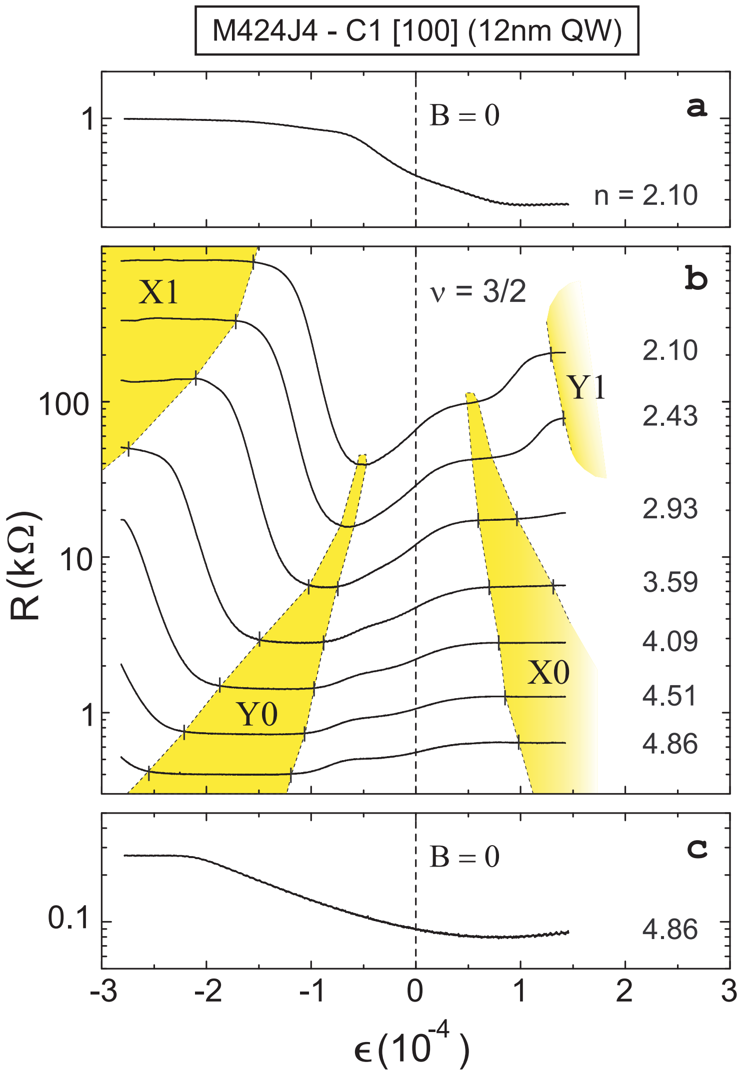

Figure 6.5: (a) and (c) The piezoresistance of electrons at $B = 0$ at densities $n = 2.10$ and 4.86×10^{11} cm^{-2}. (b) The piezoresistance of composite fermions at $\nu = 3/2$ for several densities, given in units of 10^{11} cm^{-2}. The traces were all taken at $T = 300$ mK and are offset vertically for clarity.

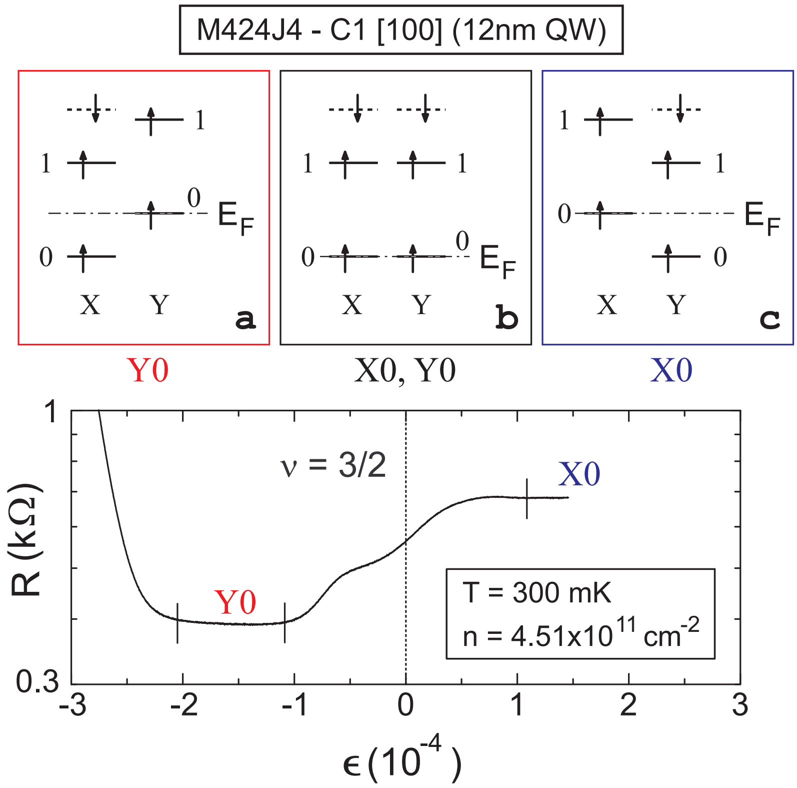

Figure 6.6: Lower panel: The piezoresistance of composite fermions at $\nu = 3/2$ at density $n = 4.51 \times 10^{11}$ cm^{-2}. (a), (b) and (c) Energy level diagrams for negative, zero, and positive strain at $\nu = 3/2$.

Similarly, at $\nu = 1/2$ CFs are transferred from X0 to Y0 with positive strain. But as seen in the energy level diagrams of Figs. 6.6(a) and (c), this situation is reversed for the case of CFs formed at $\nu = 3/2$. At $\nu = 3/2$, for finite values of strain, there is exactly one full LL and one half-filled LL. For small but finite positive values of strain, the LLs of the X valley move up compared to the Y valley, but E_F stays at the X0 level since this is the second lowest energy level (Fig. 6.6(c)). The Y0 level is of course completely full and therefore inert. Thus, although the majority of the electrons are in the Y0 level, it is the minority electrons in the X0 level which are at E_F and should dominate the electrical transport at $\nu = 3/2$. For negative but small values of strain the X0 level becomes fully occupied and inert and E_F follows the Y0 level which contains minority electrons (Fig. 6.6(a)). The opposite trends of the piezoresistance traces at $\nu = 1/2$ and 3/2 (at small magnitudes of strain) can therefore be understood by considering the position of E_F and again assuming an anisotropic CF mass and FS.

Note that if the magnitude of strain is sufficiently small so that the cyclotron energy is larger than the valley splitting energy, but large enough so that the CFs are formed fully in the X0 or Y0 levels, we expect a region of constant resistance as seen and marked by X0 and Y0 in Figs. 6.5 and 6.6 data. Interestingly, the ratio of the resistance values for X0 and Y0 regions for $\nu = 3/2$ traces is between 1.5 and 2.3 in our available density range; this is similar to the ratio r_{CF} seen for the $\nu = 1/2$ traces.

In Fig. 6.7 we demonstrate what happens at lower densities where we can apply sufficient strain to transfer *all* the electrons from one valley to the other. This happens when the valley splitting energy is larger than the cyclotron energy so that all the

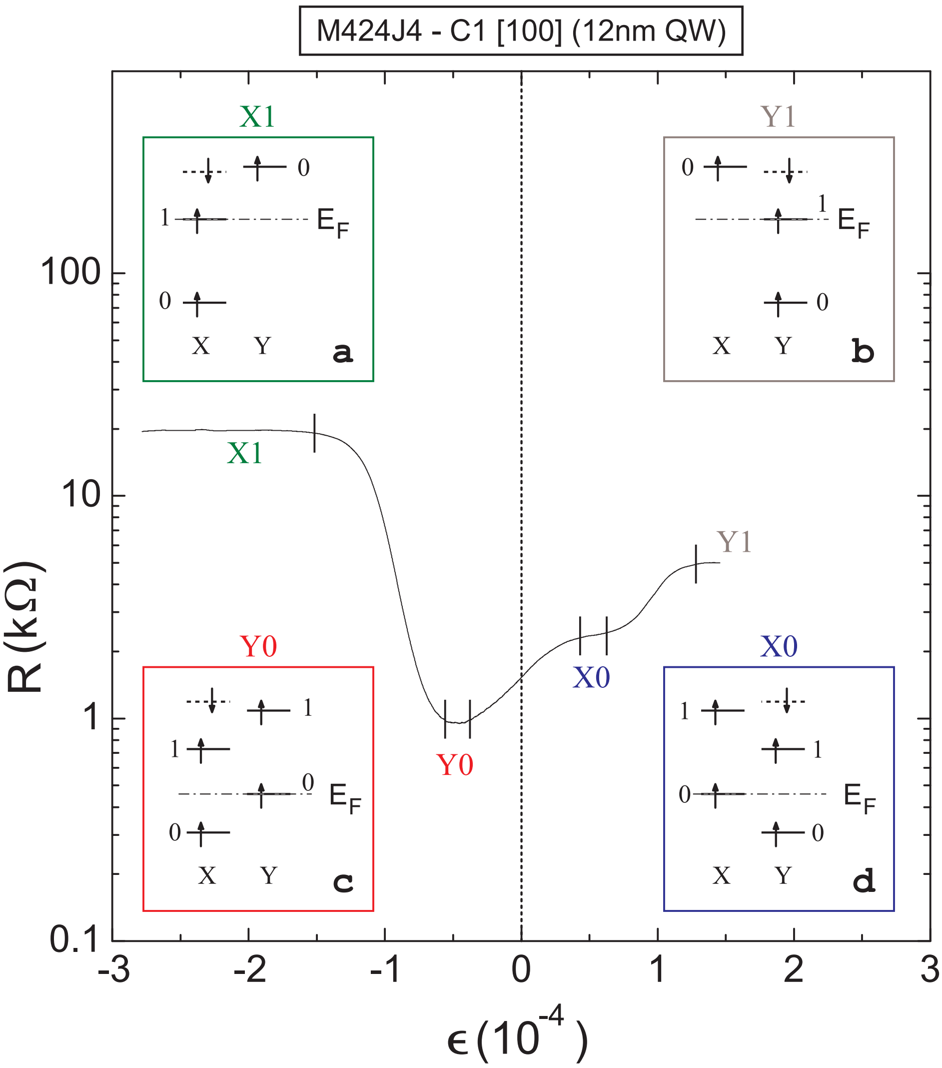

Figure 6.7: The piezoresistance of composite fermions at $\nu = 3/2$ taken at $T = 300$ mK at density $n = 2.10 \times 10^{11}$ cm^{-2}. Insets show the four possible energy level diagrams.

electrons occupy the X valley (i.e., the X0 and X1 levels) or the Y valley (Y0 and Y1). The E_F then lies either at the X1 level for very large negative values of strain (Fig. 6.7(a)), or at the Y1 level for very large positive strains (Fig. 6.7(b)). The piezoresistance trace in Fig. 6.7 and other low-density traces in Fig. 6.5 reveal that, as the electrons become fully valley polarized for either positive or negative strains, the resistance increases. This is likely because of the loss of screening upon full valley and spin polarization [65; 80]. Most remarkable, however, is that the resistance rises much more for negative values of strain compared to positive strains. The saturation value for very large negative strains is in fact higher than the saturation value for positive strains, similar to the $B = 0$ and $\nu = 1/2$ data. These observations provide evidence for the CF transport anisotropy even when the $\nu = 3/2$ CFs are formed in the second LL.

6.2.4 Discussion

As we mentioned before, the piezoresistance at $B = 0$ stems from the anisotropy of the effective mass and FS. The FS anisotropy, however, typically leads to an anisotropic scattering time which can also affect transport. In a simple Drude model, assuming isotropic scattering, the resistance ratio (r_e) is equal to the mass ratio along the two directions (m_l/m_t). In our system for high densities ($n > 2 \times 10^{11}$ cm^{-2}) we measure $r_e \simeq 3$ as shown in Fig. 6.8. In agreement with our results, a value of 2.8 is reported by Dasgupta *et al.* [81] for (110)-oriented AlAs QWs. These values contradict the simple Drude prediction $m_l/m_t = 5.12$, if one assumes a fixed scattering time along both directions. However, this discrepancy can be understood by incorporating a scattering time that is longer along the larger mass direction. This is a reasonable

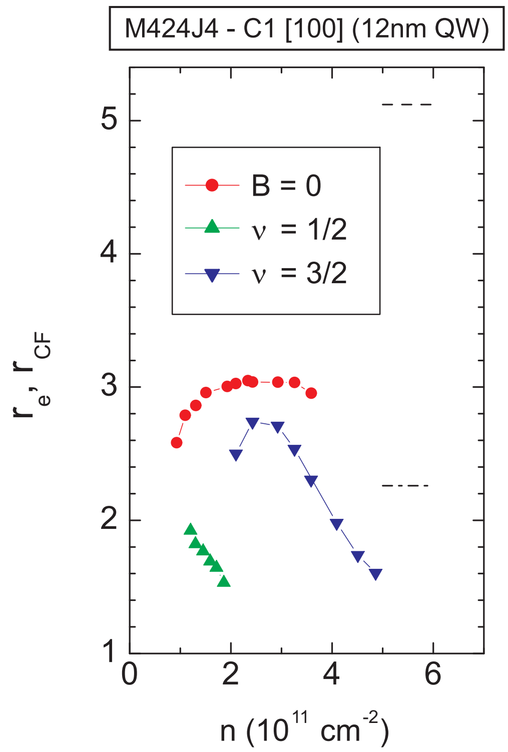

Figure 6.8: Ratio of resistances when electron/CFs are in X valley compared to Y valley while current is passed along [100] direction. Piezoresistance traces from which these ratios were deduced were taken at 300 mK. The predictions of simple Drude model for a mass anisotropy ratio of $m_l/m_t = 5.12$ and $\sqrt{m_l/m_t} = 2.26$ are shown by dashed and dotted-dashed lines, respectively.

assumption since along the large mass direction the Fermi wave vector is larger and hence electrons should scatter less because of their larger momentum [75; 76; 82]. Note that, in the most realistic scenario, the anisotropic scattering time comes about because of the anisotropy of the FS and can only *reduce* r_e below the mass anisotropy ratio.

The interpretation of the resistance ratio r_{CF} for the CFs is less clear. We emphasize that experimentally we measure a sizable r_{CF} but r_{CF} is always smaller than r_e (see Fig. 6.8). In a simple Drude model, this observation implies that either the mass anisotropy ratio for CFs is smaller than for electrons at $B = 0$ or the scattering for CFs is more anisotropic. The mass anisotropy ratio for CFs being smaller than for electrons is plausible. In an ideal, isotropic 2D system, all the physical quantities of CFs are determined by the Coulomb interaction ($\propto 1/\sqrt{x^2 + y^2}$) where x and y are components of the distance between two electrons. Note that, at a fixed filling factor, this interaction is solely quantified by the magnetic length $l_B = \sqrt{\hbar/eB}$ [24; 25; 26]. Now a system with an anisotropic FS at $B = 0$ can be mapped to a system with isotropic FS at $B = 0$ and an anisotropic Coulomb interaction ($\propto 1/\sqrt{x^2\gamma^2 + y^2/\gamma^2}$), where $\gamma = (m_l/m_t)^{1/4}$. Obviously, in such a case the strength of the Coulomb interaction depends not only on l_B but also on the direction and γ. If one assumes that the transport mass of CFs along some direction is determined by the strength of the Coulomb interaction along that direction, then the mass anisotropy ratio of CFs is given by $\gamma^2 = \sqrt{m_l/m_t}$ rather than m_l/m_t, consistent with the observation that $r_{CF} < r_e$.

A theoretical study [83] that takes into account the mass anisotropy of electrons at $B = 0$ predicts that the form of the FS for CFs is identical to the zero field FS but that, despite this anisotropy, the CF effective mass is almost isotropic. It is not obvious what this theory would predict for the resistance of the CFs. If the CF scattering time followed the anisotropy of its FS, however, in a simple Drude model an isotropic CF mass would imply an r_{CF} which has the opposite behavior to what we observe experimentally. On the other hand, our data do not rule out a hypothetical situation where the effective mass is anisotropic but the FS is isotropic.

Can the anisotropic transport we observe for CFs come only from anisotropic scattering? For example, it is known that disorder-induced density variations at $B = 0$

are accompanied by fluctuations in the effective magnetic field of CFs, resulting in more pronounced scattering [25]. If such variations have a preferred crystal direction (e.g., along the strain axis) and their magnitude increases with strain, then they could lead to anisotropic transport of CFs. Our data, however, provide strong evidence against such scenario. First, the piezoresistance we observe at $\nu = 1/2$ and $3/2$ is clearly linked to the valley occupation of CFs and not simply the magnitude of strain: The resistance only changes while the valleys are partially occupied and it saturates once the CFs are fully valley polarized. Second, for small values of strain near zero, the $\nu = 3/2$ piezoresistance shows the opposite trend compared to the $\nu = 1/2$ case. The CF piezoresistance anisotropy we observe therefore cannot result from a fixed anisotropic scattering in a preferred direction, and is most likely related to the effective mass and FS anisotropy of CFs.

6.3 Transport along [110]

So far, we presented piezoresistance of CFs and electrons for sample M424J4 along the [100] arm. In this section, we report piezoresistance data with the current passed along the [110] direction (45° with respect to the major axes of the valleys) so that the antisymmetric piezoresistance due to mass anisotropy [74] is minimized. We studied two samples, M424J4 and M415N2. The measurements on sample M424J4 were performed at 300 mK, and up to a magnetic field of 33 T, whereas the measurements on sample M415N2 were performed down to a temperature of 20 mK, and up to a magnetic field of 18 T.

6.3.1 Piezoresistance of M424J4

The piezoresistance traces for sample M424J4 at $B = 0$, $\nu = 3/2$ and $\nu = 1/2$ are shown in Fig. 6.9. We first discuss the piezoresistance data taken at $B = 0$ and then come back to $\nu = 1/2$ and $\nu = 3/2$.

The $B = 0$ piezoresistance data for a range of densities are shown in Fig. 6.9(a). The piezoresistance data exhibit several distinct features depending on the density. For high densities, the resistance increases as strain is swept away from zero and, at high values of strain the resistance shows a kink following which it either saturates or changes very slowly. The kink positions in the piezoresistance traces mark the onset of full valley polarization of electrons, as documented in section 3.3 and Ref. [65]. The piezoresistance data at low densities, however, show a resistance peak before the saturation.

The piezoresistance at $B = 0$ can be understood by incorporating the anisotropic effective mass of electrons and the role of screening and scattering. A simple Drude model, which adds the conductivities of the two valleys with anisotropic effective masses and assumes a fixed scattering time, predicts an increase in resistance away from zero strain followed by a saturation once the inter-valley electron transfer ceases. The prediction of this model is shown in Fig. 6.9(a) by a dashed line. This curve is only adjusted to match the kink position and the resistance minimum of the $n = 4.09 \times 10^{11}$ cm^{-2} data. This model gives the ratio of the resistances from saturation to balance as $R_e = (r+1)^2/4r = 1.83$, where r is the effective mass ratio with a value of $r = m_l/m_t = 5.12$ in our system.

We point out that there are additional contributions from screening and scattering effects. Screening becomes less effective with increasing valley polarization and can

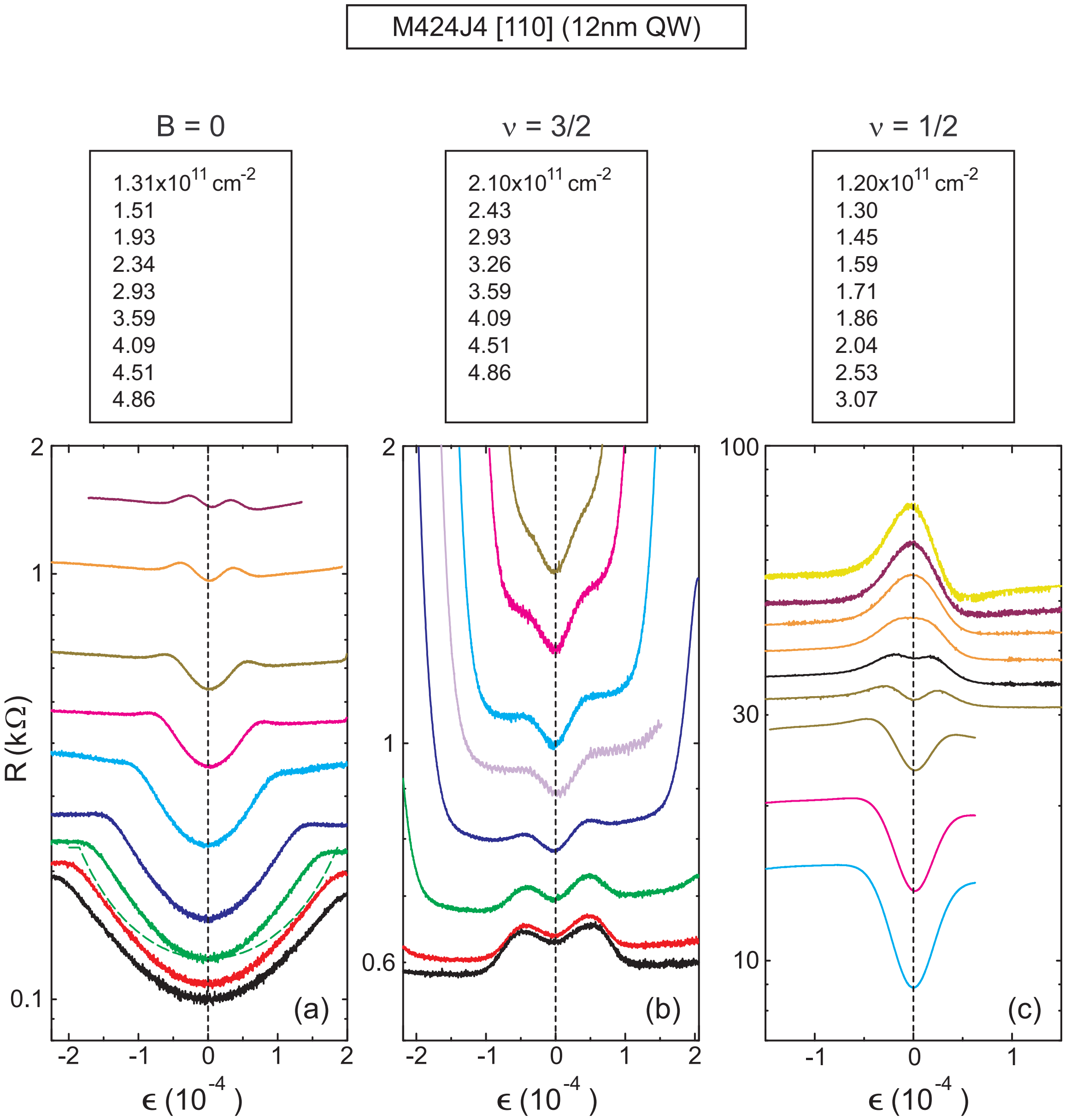

Figure 6.9: (a), (b) and (c) Piezoresistance traces at different densities for electrons at $B = 0$ and CFs at $\nu = 3/2$ and $\nu = 1/2$. The values of density are given above each panel, the top trace corresponds to the lowest density. All traces were taken at $T = 300$ mK. The prediction for the piezoresistance according to a simple (Drude) model is shown by a dashed curve in panel (a).

cause an extra increase in the resistance at larger valley polarizations [65]. This is analogous to the case of spin in many 2DESs where the resistance increases by a factor of up to 5 when the spin polarization changes from zero to one and screening is diminished [48; 52; 84; 85; 86]. In contrast to screening, the inter-valley scattering is more pronounced when two valleys are occupied and results in a larger resistance around balance. It is likely that the contributions from all these three effects exist in the $B = 0$ piezoresistance. At high densities, the data show a faster rise in resistance with strain compared to the simple Drude model and the experimental value of R_e is slightly larger than the value predicted by this model, implying the importance of screening and effective mass anisotropy. However, as the density is lowered, R_e decreases and the piezoresistance exhibits an extra resistance peak before the kink, suggesting an increase in the inter-valley scattering.

The piezoresistance at $\nu = 1/2$ and $3/2$ should also be influenced by the anisotropy of effective mass, screening and scattering effects. As we mentioned before CFs are more susceptible to disorder and the effective mass anisotropy for CFs might be different from the electrons at zero field. Despite these differences, piezoresistance traces for CFs at $\nu = 1/2$ and $3/2$; shown in Fig. 6.9(b) and (c) exhibit qualitatively similar features to the piezoresistance of electrons at $B = 0$.

The piezoresistance of CFs at $\nu = 1/2$ is shown in Fig. 6.9(c) for a range of densities. At high densities, the resistance of CFs increases as strain is swept away from zero and then saturates at high strain values, consistent with the $B = 0$ data at high densities. At intermediate densities, the $\nu = 1/2$ piezoresistance exhibits an extra resistance peak before the kink, similar to the $B = 0$ data at low densities. However, for the lowest densities, the resistance peaks at positive and negative strains merge and a big bump appears in the piezoresistance at $\nu = 1/2$. This resistance bump around zero strain is also observed when current is passed along [100] as shown in Fig. 6.4. This observation suggests that the inter-valley scattering for CF at the lowest densities is more pronounced.

In Fig. 6.9(b), we present the piezoresistance data at $\nu = 3/2$. As discussed before, $\nu = 3/2$ goes through multiple transitions and the dramatic rise in resistance at higher strains is because of the coincidence of electron LLs (X1 and Y1). However, when CFs are transferred only between X0 and Y0 for small values of strain around zero, the $\nu = 3/2$ piezoresistance traces exhibit similar features to the piezoresistance of electrons at $B = 0$ and CFs at $\nu = 1/2$: Resistance rises away from zero and then saturates with or without showing a resistance peak before the saturation.

6.3.2 Piezoresistance of M415N2

The data presented so far were from sample M424J4 at $T = 300$ mK. Now we show data from another sample (M415N2) at a lower temperature, $T = 20$ mK. Figure 6.10 shows a representative magnetoresistance trace at $n = 5.47 \times 10^{11}$ cm^{-2} for $\epsilon = 0$ (balanced valleys) for sample M415N2. In addition to the integer quantum Hall states at low B, well-developed FQH states around $\nu = 3/2$ such as $\nu = 5/3$, 4/3, 8/5 and 7/5 (and also in the second Landau level at $\nu = 8/3$ and 7/3) can be seen.

The piezoresistance traces at $B = 0$ and at $\nu = 3/2$ are shown in Figs. 6.11(a) and (b). Each trace in these figures is normalized to the value of resistance at $\epsilon = 0$ and shifted by 0.3 units vertically for clarity.

The piezoresistance traces at $B = 0$ shown in Fig. 6.11(a) for M415N2 are overall very similar to the data for M424J4 presented in Fig. 6.9(a). In Fig. 6.11(a), for the

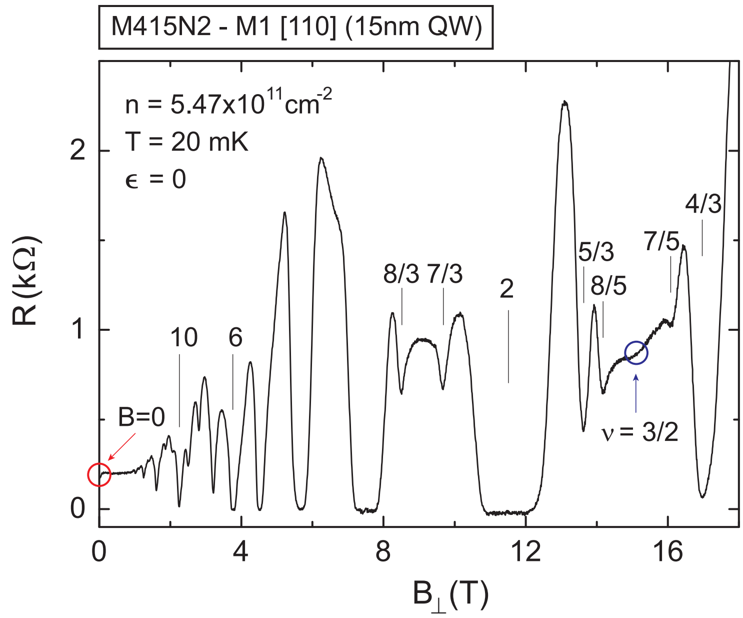

Figure 6.10: Magnetoresistance (R vs. $B_\perp$) trace at zero strain (balanced valleys).

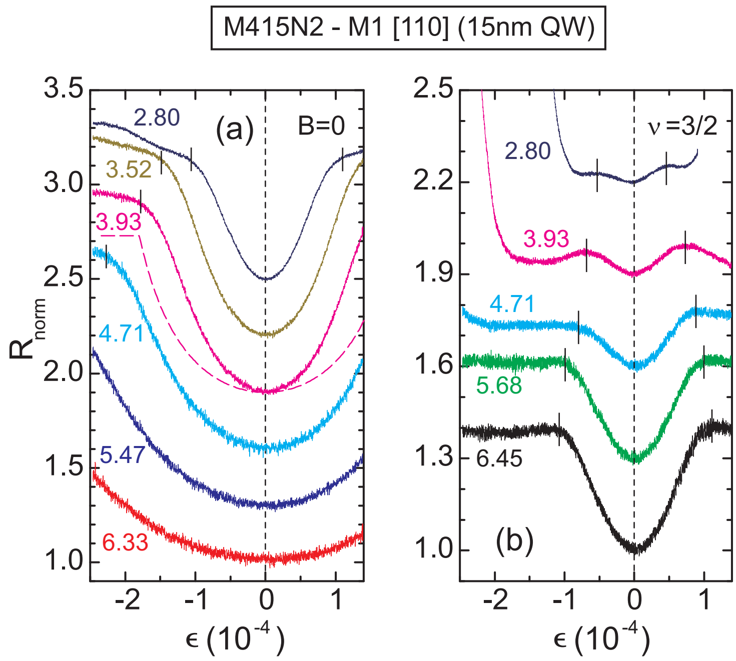

Figure 6.11: (a) and (b) Piezoresistance traces at different densities for electrons and CFs, respectively. The values of density are given in units of 10^{11} cm^{-2}, and the positions of the "kinks" are marked by vertical lines. All traces were taken at T = 20 mK.

$B = 0$ data we also include the prediction of a simple Drude model with a dashed line. This curve is only adjusted to match the kink position and the resistance minimum of the $n = 3.93 \times 10^{11}$ cm^{-2} data. The data show a faster rise in resistance with strain compared to the simple Drude model, suggesting the importance of the screening effects at high densities, in agreement with the data presented in Fig. 6.9(a).

The piezoresistance of CFs at $\nu = 3/2$ is shown in Fig. 6.9(b) for several densities. At high densities, CFs exhibit an increase in resistance as strain is swept away from zero and then the resistance saturates at high strain values. In contrast to the data shown in Fig. 6.9(b), the piezoresistance of sample M415N2 does not show a resistance peak before the saturation at high densities. Furthermore, the value of resistance is smaller for balanced valleys compared to single-valley. These observations suggest that inter-valley scattering is less pronounced for sample M415N2. As we discuss further in the following section, some of these differences may also result from the variation in temperature.

6.3.3 Temperature dependence of piezoresistance at $\nu = 3/2$

In this section we present the temperature dependence of the CF piezoresistance at $\nu = 3/2$. In Figs. 6.12(b) and (c) we show piezoresistance traces for CFs at two densities. The data in Fig. 6.12(b) reveal that, at high densities and for small strains so that the valley polarization is small, CFs exhibit a metallic behavior ($dR/dT > 0$). With increasing strain, however, the CFs turn insulating ($dR/dT < 0$) as they become valley polarized. This observation demonstrates the importance of the discrete degrees of freedom for the MIT of CFs. At lower densities (Fig. 6.12(c)) the metallic behavior around zero strain disappears, and the CFs act insulating in the full strain range,

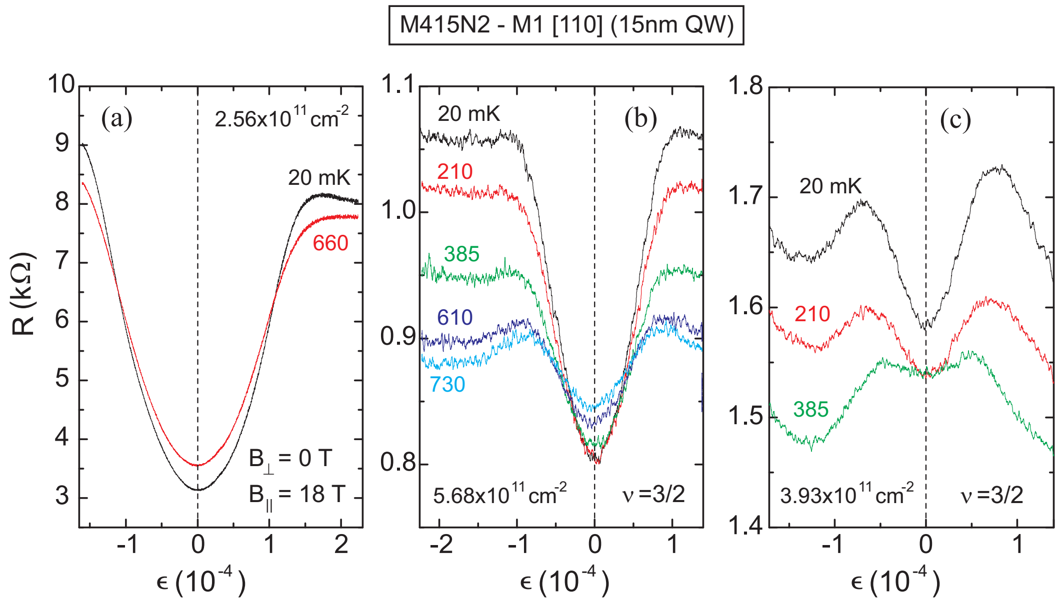

Figure 6.12: (a) Piezoresistance traces at different temperatures for spin polarized electrons. (b) and (c) Piezoresistance traces at different temperatures for CFs at $\nu = 3/2$ for two different densities.

including at $\epsilon = 0$ where they are valley degenerate. We also note that at high temperatures the piezoresistance shows a resistance peak before saturation similar to the data presented in Fig. 6.9(b) for sample M424J4.

As discussed in Chapter 3 and also in Ref. [65], for wide AlAs 2DESs, not only spin but also valley polarization is an important parameter for the apparent MIT, namely, the 2DES exhibits an insulating behavior when both valley and spin polarizations pass beyond some threshold value. Examples of such data are presented in Chapter 3 in Figs. 3.3 and 3.4. We also illustrate this behavior for sample M415N2 in Fig. 6.13. In Fig. 6.13(a) at zero total parallel field, where the 2DES is spin unpolarized, it shows a metallic behavior in the entire strain range. However, when 2DES is fully spin polarized with the application of large parallel magnetic field, increasing the

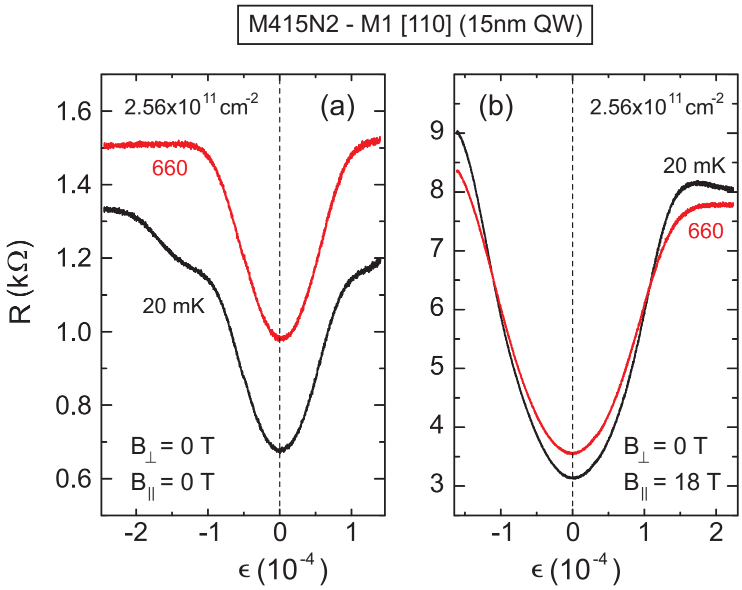

Figure 6.13: Piezoresistance traces at two temperatures for (a) spin unpolarized electrons (b) fully spin polarized electrons. The shift of the balanced point in the presence of parallel magnetic field is corrected for the piezoresistance traces taken at finite parallel magnetic fields.

valley polarization drives the system from a metal to an insulator as shown in 6.13(b) and 6.12(a).

Our $\nu = 3/2$ data in Fig. 6.12(b) show that the CFs qualitatively behave like the electrons. Note that because of the large g-factor, the Zeeman energy in our sample is comparable to and even larger than the cyclotron energy. Therefore, the CFs at $\nu = 3/2$ are fully spin polarized while we control their valley occupation via the application of strain. The electron data of Fig. 6.12(a) and CF data of Fig. 6.12(b) imply that, when the spin degree of freedom is frozen, (high density) electrons and CFs both show a metallic behavior when they have a valley degree of freedom. Increasing the valley polarization drives both systems into an insulating phase.

We observe the metallic behavior in the absence of strain and the valley polarization driven MIT for CFs in the high density range ($n > 3.93 \times 10^{11}$ cm^{-2}). As the density is lowered, the metallic temperature dependence disappears and CFs exhibit an insulating behavior regardless of their valley polarization (Fig. 6.12(c)). This is consistent with the increasing disorder in the system at lower densities, and illustrates the disorder-induced MIT of CFs. We emphasize, however, that the CFs seem to be more sensitive to disorder than electrons: In the absence of strain, the density below which the *electrons* exhibit an insulating phase is $\sim 1 \times 10^{11}$ cm^{-2} while for the $\nu = 3/2$ CFs it is $\sim 4 \times 10^{11}$ cm^{-2}.

6.4 Summary

In this Chapter, we addressed the transport properties of CFs in a two-valley system where each valley has an elliptical Fermi surface. The piezoresistance data along the [100] direction demonstrate that, in a 2D electron system with an anisotropic effective mass and FS at zero magnetic field, the CFs at filling factors 1/2 and 3/2 also exhibit anisotropic transport, consistent with a qualitative transference of the electron mass and FS anisotropy to the CFs. However, better theoretical treatment is clearly needed to describe the CFs in an anisotropic system and in particular quantitatively determine their resistance and mass or FS anisotropy. In addition, the piezoresistance data along the [110] direction also demonstrate that CFs and electrons show qualitatively very similar behaviors. First, the piezoresistances of both CFs and electrons are affected by the effective mass anisotropy, screening and scattering. Second, the temperature dependence of the resistance, and the transition of CFs to an insulating phase with increasing valley polarization or decreasing density, are qualitatively similar to electrons. The results presented in this Chapter illustrates the similarity between transport properties of electrons and CFs.

Chapter 7

Summary and Future projects

7.1 Summary

The first part of this thesis is dedicated to understanding the dependence of fundamental parameters of the 2DES such as the effective mass (m^*), the effective Lande g-factor (g^*) and the conduction-band deformation potential (E_2^*) on spin and valley degrees of freedom. Here are the main results from Chapters 3, 4 and 5:

1. For a single-component (fully spin and valley polarized) system, interactions suppress m^* below m_b in the whole r_s range independent of the system parameters such as layer thickness, disorder and Fermi surface anisotropy. Incidentally, m^* is suppressed when the electron system exhibits an insulating behavior.

2. For a multi-component (partially spin/valley polarized) system, interactions enhance m^* above m_b and m^* increases with increasing r_s, consistent with previous reports on other 2DESs.

3. m^*, g^*, and E_2^* reveal a clear contrast between spin and valley degrees of freedom while g^*m^* and $E_2^*m^*$ do not. It appears as if m^*, g^* and E_2^* conspire to make the susceptibilities g^*m^* and $E_2^*m^*$ behave similarly!

In Chapter 6, we address some of the properties of composite fermions (emergent particles at high magnetic fields) in wide AlAs quantum wells. The main results from Chapter 6 are:

1. In 2DESs confined to wide AlAs quantum wells, the composite fermions possess a valley degree of freedom and show piezoresistance qualitatively very similar to electrons.

2. The composite fermion effective mass and Fermi surface qualitatively follow the anisotropy of the electrons at $B = 0$.

3. Temperature dependent measurements reveal that the resistance of composite fermions has a metallic temperature dependence for small values of valley polarization but turns insulating as they are driven to full valley polarization.

The results highlight the similarity between transport properties of electrons and composite fermions.

7.2 Future projects

In Chapter 6, we presented qualitative evidence that the Fermi surface of composite fermions is anisotropic. To quantify this anisotropy, experiments that directly probe the Fermi surface and its anisotropy would be helpful. For example, measurements of commensurability oscillations in 2D systems with a periodically modulated electron density or an etched anti-dot array, and magnetic focusing experiments with two quantum point contacts arranged at different angles could shed light on this problem. However, there remain significant challenges in performing such experiments. All the experiments proposed above require pattering additional features on the top surface of the sample via electron beam lithography techniques. In addition, etching an anti-dot array requires the usage of an electron cyclotron resonance (ECR) etcher or other types of etchers. These extra processing steps may lower the quality of the samples. For example, in one of our samples (M409Q2) we had three 60×60 μm^2 square mesas patterned with photolithography techniques. Among these three regions two were further patterned with an anti-dot array using electron beam lithography and then etched with an ECR etcher. During these additional processing steps one region was left un-patterned (blank) and protected with PMMA. The data from this blank region for sample M409Q2 are presented in section 3.4. Although the magnetoresistance data for this region showed the integer quantum Hall states at low fields (see Fig. 3.6), the quality was not good enough to show well-developed fractional quantum Hall states at higher fields. It is possible that the etching process might have caused some damage to the protected parts of the sample. However, we note that we have only limited data from a single sample and the fractional quantum Hall states are generally harder to observe. As a final remark, we also mention that etching results in an inhomogeneous strain distribution in the case of anti-dot lattice and gives rise to an anomalous piezoresistance of electrons at zero field and difficult to understand commensurability peaks [87]. Therefore, the most promising experiments should not involve etching but rather a patterned surface gate for density modulation or magnetic focusing. Even for these experiments one has to be mindful of the inhomogeneous strain that may result from the patterned region on the sample surface.

Appendix A

Temperature dependence of resistance at different spin and valley polarizations

It is clear from the data presented in section 3.4.1 that the spin and valley polarizations play a crucial role in the metal insulator transition of electrons. Here we report the temperature dependence of resistance as a function of density for the four different spin and valley polarizations: $(P_s = 0, P_v = 0)$, $(P_s = 0, P_v = 1)$, $(P_s = 1, P_v = 0)$ and $(P_s = 1, P_v = 1)$. These spin and valley polarizations are achieved through the application of parallel magnetic field and strain at zero perpendicular magnetic field. We note that a slightly negative strain is applied to account for the shift in the balanced point for the $(P_s = 1, P_v = 0)$ case (see Figs. 3.1 and 3.2; also Ref. [64]).

In Fig. A.1, we present the results from sample M424J4 with current along the [110] direction. The right and left panels correspond to $P_v = 1$ and $P_v = 0$; and the top and bottom panels correspond to $P_s = 1$ and $P_s = 0$ respectively.

As is clear from Fig. A.1, for the ($P_s = 1, P_v = 1$) case the temperature dependence of resistance shows an insulating behavior in the whole density range, in agreement with the results of section 3.4.1. We note that the insulating behavior becomes weaker at higher densities. However, we emphasize that the measurements are done at a fixed strain value as shown in the figure because of the limited strain range in our measurements. Therefore, for high density traces marked with "question mark", valley polarization may be less than 1. For another sample (M409Q2) we can reach higher strain values and for a density of 3.8×10^{11} cm^{-2}, the ($P_s = 1, P_v = 1$) case still shows as insulating behavior (see Fig. 3.3).

For the ($P_s = 1, P_v = 0$) case, although high densities show metallic temperature dependence, at low enough densities the system turns insulating. The critical density for the MIT is around 0.94×10^{11} cm^{-2}.

For the ($P_s = 0, P_v = 1$) and ($P_s = 0, P_v = 0$) cases, the critical densities are pushed to even lower densities. The data suggest that the critical densities for these two cases are around 0.64×10^{11} cm^{-2} (if not lower). Interestingly, the critical densities are not the same for ($P_s = 1, P_v = 0$) and ($P_s = 0, P_v = 1$); signaling a contrast between spin and valley degrees of freedom.

Our results with the current along the [100] direction are shown in Fig. A.2 and agree both qualitatively and quantitatively with the data along [110].

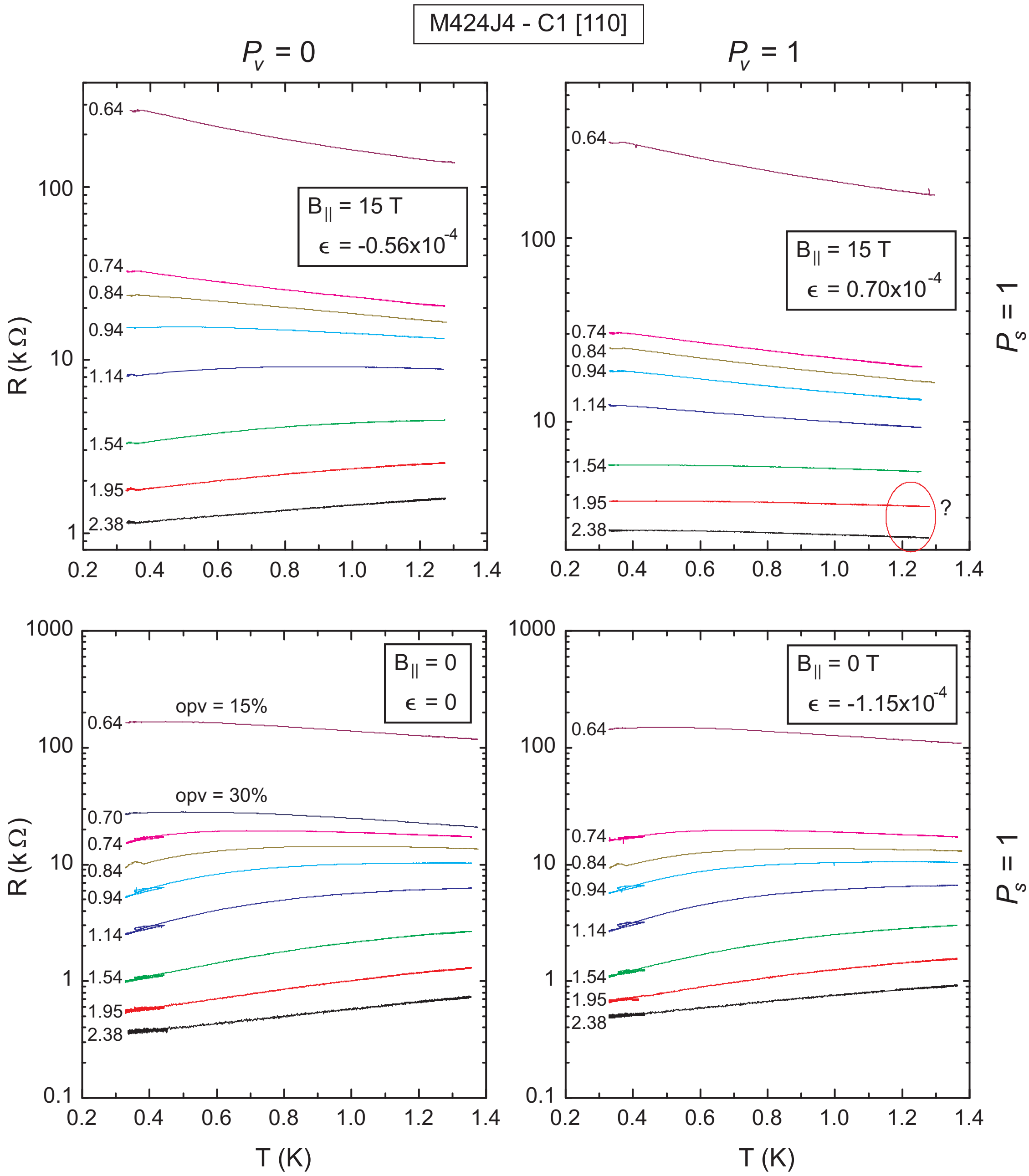

Figure A.1: The temperature dependence of resistance as a function of density for different spin and valley polarizations. The current is passed along the [110] direction. The densities are shown next to each trace in unit of 10^{11} cm^{-2}. For very low densities the out-of-phase value (opv) of resistance becomes noticeable, which is shown next to each trace if it is more than 10%.

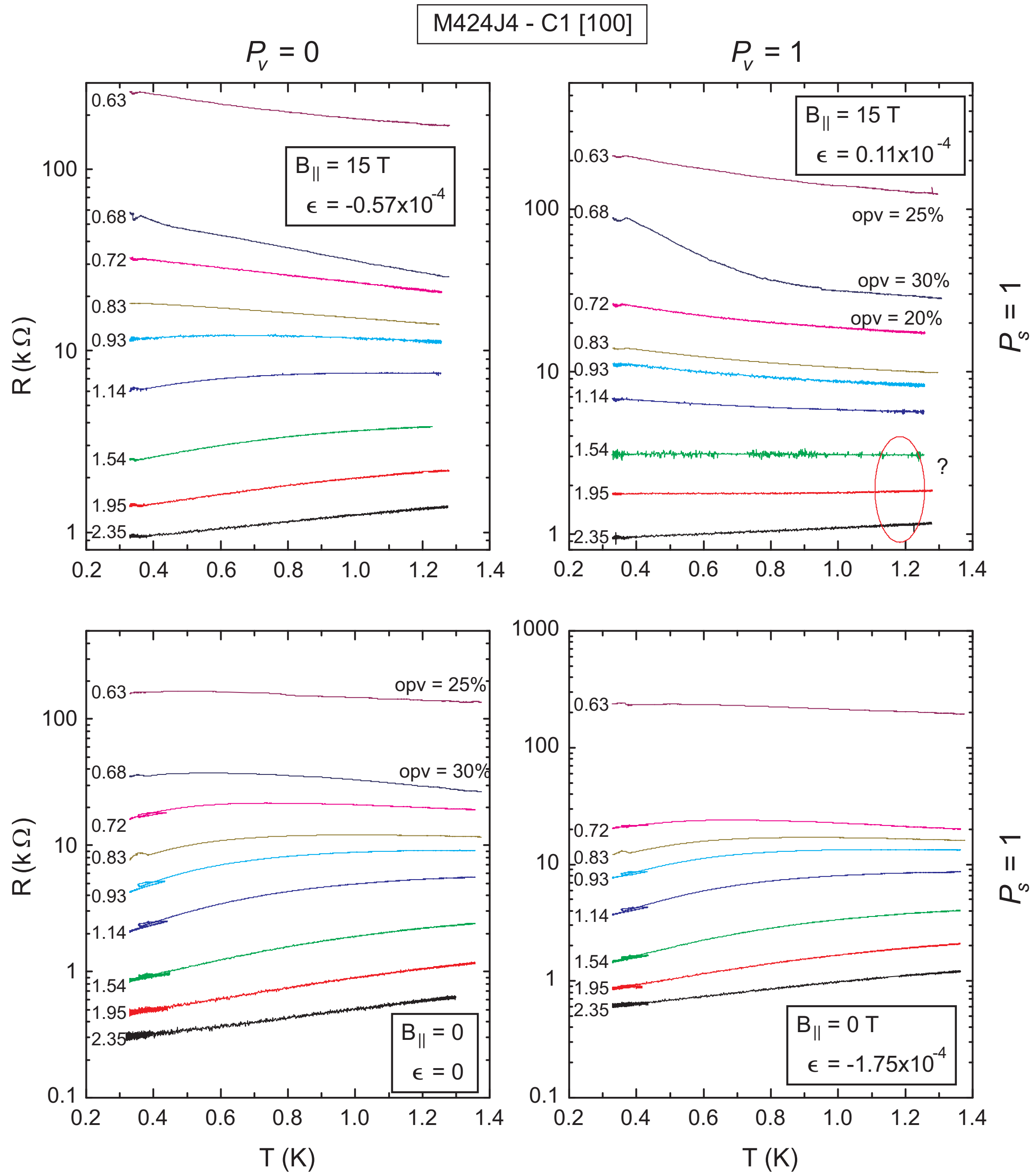

Figure A.2: The temperature dependence of resistance as a function of density for different spin and valley polarizations. The current is passed along the [100] direction. The densities are shown next to each trace in unit of 10^{11} cm^{-2}. For very low densities the out-of-phase value (opv) of resistance becomes noticeable, which is shown next to each trace if it is more than 10%.

Appendix B

Publications

B.1 Publications related to this thesis

1. Medini Padmanabhan, T. Gokmen, N. C. Bishop, and M. Shayegan, "Effective mass suppression in dilute, spin-polarized two-dimensional electron systems," Phys. Rev. Lett. **101**, 026402 (2008).

2. T. Gokmen, Medini Padmanabhan, and M. Shayegan, "Dependence of effective mass on spin and valley degrees of freedom," Phys. Rev. Lett. **101**, 146405 (2008).

3. T. Gokmen, Medini Padmanabhan, K. Vakili, E. Tutuc, and M. Shayegan, "Effective mass suppression upon complete spin-polarization in an isotropic two-dimensional electron system," Phys. Rev. B **79**, 195311 (2009).

4. T. Gokmen, Medini Padmanabhan, and M. Shayegan, "Contrast between spin and valley degrees of freedom," *submitted to Phys. Rev. Lett.*

5. T. Gokmen, Medini Padmanabhan, and M. Shayegan, "Transference of transport anisotropy to composite fermions," *submitted to Nature Physics.*

6. T. Gokmen, Medini Padmanabhan, and M. Shayegan, "Temperature dependence of piezoresistance of composite fermions with a valley degree of freedom," *submitted to Solid State Communications.*

B.2 Other publications

1. T. Gokmen, and M. Shayegan, "Density and strain dependence of $\nu = 1$ energy gap in an AlAs quantum well," *submitted to Phys. Rev. B.*

2. Medini Padmanabhan, T. Gokmen, and M. Shayegan, "Composite fermion valley polarization energies: Evidence for particle-hole asymmetry," *submitted to Phys. Rev. B.*

3. Medini Padmanabhan, T. Gokmen, and M. Shayegan, "Ferromagnetic fractional quantum Hall states in a valley degenerate two-dimensional electron system," Phys. Rev. Lett. **104**, 016805 (2010).

4. J. Shabani, T. Gokmen, Y. T. Chiu, and M. Shayegan, "Evidence for developing fractional quantum Hall states at even denominator 1/2 and 1/4 fillings in asymmetric wide quantum wells," Phys. Rev. Lett. **103**, 256802 (2009).

5. J. Shabani, T. Gokmen, and M. Shayegan, "Correlated states of electrons in wide quantum wells at low fillings: The role of charge distribution symmetry," Phys. Rev. Lett. **103**, 046805 (2009).

6. Medini Padmanabhan, T. Gokmen, and M. Shayegan, "Density dependence of valley polarization energy for composite fermions," Phys. Rev. B **80**, 035423 (2009).

7. Reza Asgari, T. Gokmen, B. Tanatar, Medini Padmanabhan, and M. Shayegan, "Effective mass suppression in a ferromagnetic two-dimensional electron liquid," Phys. Rev. B **79**, 235324 (2009).

8. A. Tsukazaki, A. Ohtomo, M. Kawasaki, S. Akasaka, H. Yuji, K. Tamura, K. Nakahara, T. Tanabe, A. Kamisawa, T. Gokmen, J. Shabani, and M. Shayegan, "Spin susceptibility and effective mass of two-dimensional electrons in $MgxZn_{1-x}$ / ZnO heterotructures," Phys. Rev. B **78**, 233308 (2008).

9. T. Gokmen, Medini Padmanabhan, O. Gunawan, Y. P. Shkolnikov, K. Vakili, E. P. De Poortere, and M. Shayegan , "Parallel magnetic-field tuning of valley splitting in AlAs two-dimensional electrons," Phys. Rev. B **78**, 233306 (2008).

10. Medini Padmanabhan, T. Gokmen, and M. Shayegan, "Enhancement of valley susceptibility upon complete spin-polarization," Phys. Rev. B **78**, 161301 (2008).

11. O. Gunawan, T. Gokmen, E. P. De Poortere, and M. Shayegan, "Characterization of the anomalous giant piezoresistance in AlAs two-dimensional electrons with antidot lattices," Semicond. Sci. Technol. **23**, 085005 (2008).

12. O. Gunawan, T. Gokmen, Y. P. Shkolnikov, E. P. De Poortere, and M. Shayegan, "Anomalous giant piezoresistance in AlAs two-dimensional electrons with antidot lattices," Phys. Rev. Lett. **100**, 036602 (2008).

13. N. C. Bishop, Medini Padmanabhan, O. Gunawan, T. Gokmen, E. P. De Poortere, Y. P. Shkolnikov, E. Tutuc, K. Vakili, and M. Shayegan, "Valley susceptibility of interacting electrons and composite fermions," Physica E **40**, 986 (2008).

14. T. Gokmen, Medini Padmanabhan, E. Tutuc, M. Shayegan, S. De Palo, S. Moroni, and Gaetano Senatore, "Spin susceptibility of interacting two-dimensional electrons with anisotropic effective mass," Phys. Rev. B **76**, 233301 (2007).

15. O. Gunawan, T. Gokmen, K. Vakili, Medini Padmanabhan, E. P. De Poortere, and M. Shayegan , "Spin-valley phase diagram of the two-dimensional metal-insulator transition," Nature Physics **3**, 388 (2007).

16. O. Gunawan, Y. P. Shkolnikov, K. Vakili, T. Gokmen, E. P. De Poortere, and M. Shayegan, "Valley susceptibility of an interacting two-dimensional electron system," Phys. Rev. Lett. **97**, 186404 (2006).

17. K. Vakili, T. Gokmen, O. Gunawan, Y. P. Shkolnikov, E. P. De Poortere, and M. Shayegan, "Dependence of persistent gaps at Landau level crossings on relative spin," Phys. Rev. Lett. **97**, 116803 (2006).

Bibliography

[1] R. Dingle, H. L. Stormer, A. C. Gossard, and W. Wiegmann, "Electron mobilities in modulation-doped semiconductor heterojunction superlattices," Appl. Phys. Lett. **33**, 665 (1978)

[2] See, e.g., M. Shayegan, "Flatland Electrons in High Magnetic Fields," in "High Magnetic Fields: Science and Technology," Vol. 3, edited by Fritz Herlach and Noboru Miura, (World Scientific, Singapore, 2006), pp. 31-60.

[3] Gordon Baym and Christopher Pethick, *Landau Fermi-Liquid Theory* (Wiley, New York, 2007)

[4] Florian Gebhard, *The Mott Metal-Insulator Transition* (Springer-Verlag, Berlin Heidelberg New York, 1997)

[5] P. W. Anderson, "Absence of diffusion in certain random lattices," Phys. Rev. **109**, 1492 (1958)

[6] E. Abrahams, P. W. Anderson, D. C. Licciardello, and T. V. Ramakrishnan, "Scaling theory of localization: Absence of quantum diffusion in two dimensions," Phys. Rev. Lett. **42**, 673 (1979)

[7] S. V. Kravchenko, G. V. Kravchenko, J. E. Furneaux, V. M. Pudalov, and M. D'Iorio, "Possible metal-insulator transition at $B = 0$ in two dimensions," Phys. Rev. B **50**, 8039 (1994)

[8] J. Lam, M. D'Iorio, D. Brown, and H. Lafontaine, "Scaling and the metal-insulator transition in Si/SiGe quantum wells," Phys. Rev. B **56**, R12741 (1997)

[9] P. T. Coleridge, R. L. Williams, Y. Feng, and P. Zawadzki, "Metal-insulator transition at $B = 0$ in p-type SiGe," Phys. Rev. B **56**, R12764 (1997)

[10] G. Landwehr S. S. Murzin, S. I. Dorozhkin and A. C. Gossard, "Effect of hole-hole scattering on the conductivity of the two-component 2D hole gas in GaAs/(AlGa)As heterostructures," JETP Letters **67**, 113 (1998)

[11] Y. Hanein, U. Meirav, D. Shahar, C. C. Li, D. C. Tsui, and Hadas Shtrikman, "The metalliclike conductivity of a two-dimensional hole system," Phys. Rev. Lett. **80**, 1288 (1998)

[12] M. Y. Simmons, A. R. Hamilton, M. Pepper, E. H. Linfield, P. D. Rose, D. A. Ritchie, A. K. Savchenko, and T. G. Griffiths, "Metal-insulator transition at $B = 0$ in a dilute two-dimensional GaAs-AlGaAs hole gas," Phys. Rev. Lett. **80**, 1292 (1998)

[13] S. J. Papadakis and M. Shayegan, "Apparent metallic behavior at $B = 0$ of a two-dimensional electron system in AlAs," Phys. Rev. B **57**, R15068 (1998)

[14] Y. Hanein, D. Shahar, J. Yoon, C. C. Li, D. C. Tsui, and Hadas Shtrikman, "Observation of the metal-insulator transition in two-dimensional n-type GaAs," Phys. Rev. B **58**, R13338 (1998)

[15] Tohru Okamoto, Mitsuaki Ooya, Kunio Hosoya, and Shinji Kawaji, "Spin polarization and metallic behavior in a silicon two-dimensional electron system," Phys. Rev. B **69**, 041202 (2004)

[16] K. Lai, W. Pan, D. C. Tsui, and Ya-Hong Xie, "Observation of the apparent metal-insulator transition of high-mobility two-dimensional electron system in a $Si/Si_{1-x}Ge_x$ heterostructure," Appl. Phys. Lett. **84**, 302 (2004)

[17] K. Lai, W. Pan, D. C. Tsui, S. A. Lyon, M. Mühlberger, and F. Schäffler, "Two-dimensional metal-insulator transition and in-plane magnetoresistance in a high-mobility strained Si quantum well," Phys. Rev. B **72**, 081313 (2005)

[18] K. v. Klitzing, G. Dorda, and M. Pepper, "New method for high-accuracy determination of the fine-structure constant based on quantized Hall resistance," Phys. Rev. Lett. **45**, 494 (1980)

[19] B. I. Halperin, "Quantized Hall conductance, current-carrying edge states, and the existence of extended states in a two-dimensional disordered potential," Phys. Rev. B **25**, 2185 (1982)

[20] *The Quantum Hall Effect*, edited by Richard E. Prange and Steven M. Girvin (Springer-Verlag, New York, 1987)

[21] John H. Davies, *The Physics of Low-dimensional Semiconductors: An Introduction* (Cambridge University Press, U.S.A., 1998)

[22] D. C. Tsui, H. L. Stormer, and A. C. Gossard, "Two-dimensional magnetotransport in the extreme quantum limit," Phys. Rev. Lett. **48**, 1559 (1982)

[23] R. B. Laughlin, "Anomalous quantum Hall effect: An incompressible quantum fluid with fractionally charged excitations," Phys. Rev. Lett. **50**, 1395 (1983)

[24] J. K. Jain, "Composite fermion approach for the fractional quantum Hall effect," Phys. Rev. Lett. **63**, 199 (1989)

[25] B. I. Halperin, Patrick A. Lee, and Nicholas Read, "Theory of the half-filled Landau level," Phys. Rev. B **47**, 7312 (1993)

[26] Jainendra K. Jain, *Composite Fermions* (Cambridge University Press, New York, 2007)

[27] R. L. Willett, R. R. Ruel, K. W. West, and L. N. Pfeiffer, "Experimental demonstration of a Fermi surface at one-half filling of the lowest Landau level," Phys. Rev. Lett. **71**, 3846 (1993)

[28] W. Kang, H. L. Stormer, L. N. Pfeiffer, K. W. Baldwin, and K. W. West, "How real are composite fermions?." Phys. Rev. Lett. **71**, 3850 (1993)

[29] V. J. Goldman, B. Su, and J. K. Jain, "Detection of composite fermions by magnetic focusing," Phys. Rev. Lett. **72**, 2065 (1994)

[30] M. Shayegan, E. P. De Poortere, O. Gunawan, Y. P. Shkolnikov, E. Tutuc, and K. Vakili, "Two-dimensional electrons occupying multiple valleys in AlAs," Phys. Stat. Sol. (b) **243**, 3629 (2006)

[31] Kamran Vakili, *Spin and Valley Ferromagnetism of Interacting, Two-Dimensional Electrons in AlAs Quantum Wells*, Ph.D. thesis, Princeton Univerity (2007)

[32] Y.P. Shkolnikov, *Two-Dimensional Electrons with Valley Degree of Freedom*, Ph.D. thesis, Princeton Univerity (2005)

[33] B. Tanatar and D. M. Ceperley, "Ground state of the two-dimensional electron gas," Phys. Rev. B **39**, 5005 (1989)

[34] Yongkyung Kwon, D. M. Ceperley, and Richard M. Martin, "Quantum Monte Carlo calculation of the Fermi-liquid parameters in the two-dimensional electron gas," Phys. Rev. B **50**, 1684 (1994)

[35] Claudio Attaccalite, Saverio Moroni, Paola Gori-Giorgi, and Giovanni B. Bachelet, "Correlation energy and spin polarization in the 2D electron gas," Phys. Rev. Lett. **88**, 256601 (2002)

[36] R. Asgari and B. Tanatar, "Many-body effective mass and spin susceptibility in a quasi-two-dimensional electron liquid," Phys. Rev. B **74**, 075301 (2006)

[37] R. Asgari, B. Davoudi, and B. Tanatar, "Effective mass enhancement in two-dimensional electron systems: the role of interaction and disorder effects," Solid State Communications **130**, 13 (2004)

[38] S. De Palo, M. Botti, S. Moroni, and Gaetano Senatore, "Effects of thickness on the spin susceptibility of the two-dimensional electron gas," Phys. Rev. Lett. **94**, 226405 (2005)

[39] Suhas Gangadharaiah and Dmitrii L. Maslov, "Spin-independent effective mass in a valley-degenerate electron system," Phys. Rev. Lett. **95**, 186801 (2005)

[40] Ying Zhang and S. Das Sarma, "Spin polarization dependence of carrier effective mass in semiconductor structures: Spintronic effective mass," Phys. Rev. Lett. **95**, 256603 (2005)

[41] Ying Zhang and S. Das Sarma, "Density-dependent spin susceptibility and effective mass in interacting quasi-two-dimensional electron systems," Phys. Rev. B **72**, 075308 (2005)

[42] T. Gokmen, Medini Padmanabhan, E. Tutuc, M. Shayegan, S. De Palo, S. Moroni, and Gaetano Senatore, "Spin susceptibility of interacting two-dimensional electrons with anisotropic effective mass," Phys. Rev. B **76**, 233301 (2007)

[43] J. L. Smith and P. J. Stiles, "Electron-electron interactions continuously variable in the range $2.1 > r_s > 0.9$," Phys. Rev. Lett. **29**, 102 (1972)

[44] W. Pan, D. C. Tsui, and B. L. Draper, "Mass enhancement of two-dimensional electrons in thin-oxide Si-MOSFETs," Phys. Rev. B **59**, 10208 (1999)

[45] V. M. Pudalov, M. E. Gershenson, H. Kojima, N. Butch, E. M. Dizhur, G. Brunthaler, A. Prinz, and G. Bauer, "Low-density spin susceptibility and effective mass of mobile electrons in Si inversion layers," Phys. Rev. Lett. **88**, 196404 (2002)

[46] A. A. Shashkin, S. V. Kravchenko, V. T. Dolgopolov, and T. M. Klapwijk, "Sharp increase of the effective mass near the critical density in a metallic two-dimensional electron system," Phys. Rev. B **66**, 073303 (2002)

[47] A. A. Shashkin, Maryam Rahimi, S. Anissimova, S. V. Kravchenko, V. T. Dolgopolov, and T. M. Klapwijk, "Spin-independent origin of the strongly enhanced effective mass in a dilute 2D electron system," Phys. Rev. Lett. **91**, 046403 (2003)

[48] K. Vakili, Y. P. Shkolnikov, E. Tutuc, E. P. De Poortere, and M. Shayegan, "Spin susceptibility of two-dimensional electrons in narrow AlAs quantum wells," Phys. Rev. Lett. **92**, 226401 (2004)

[49] Y. P. Shkolnikov, K. Vakili, E. P. De Poortere, and M. Shayegan, "Dependence of spin susceptibility of a two-dimensional electron system on the valley degree of freedom," Phys. Rev. Lett. **92**, 246804 (2004)

[50] Y.-W. Tan, J. Zhu, H. L. Stormer, L. N. Pfeiffer, K. W. Baldwin, and K. W. West, "Measurements of the density-dependent many-body electron mass in two-dimensional GaAs/AlGaAs heterostructures," Phys. Rev. Lett. **94**, 016405 (2005)

[51] F. F. Fang and P. J. Stiles, "Effects of a tilted magnetic field on a two-dimensional electron gas," Phys. Rev. **174**, 823 (1968)

[52] Tohru Okamoto, Kunio Hosoya, Shinji Kawaji, and Atsuo Yagi, "Spin degree of freedom in a two-dimensional electron liquid," Phys. Rev. Lett. **82**, 3875 (1999)

[53] S. A. Vitkalov, H. Zheng, K. M. Mertes, M. P. Sarachik, and T. M. Klapwijk, "Scaling of the magnetoconductivity of silicon MOSFETs: Evidence for a quantum phase transition in two dimensions," Phys. Rev. Lett. **87**, 086401 (2001)

[54] A. A. Shashkin, S. V. Kravchenko, V. T. Dolgopolov, and T. M. Klapwijk, “Indication of the ferromagnetic instability in a dilute two-dimensional electron system,” Phys. Rev. Lett. **87**, 086801 (2001)

[55] J. Zhu, H. L. Stormer, L. N. Pfeiffer, K. W. Baldwin, and K. W. West, “Spin susceptibility of an ultra-low-density two-dimensional electron system,” Phys. Rev. Lett. **90**, 056805 (2003)

[56] O. Prus, Y. Yaish, M. Reznikov, U. Sivan, and V. Pudalov, “Thermodynamic spin magnetization of strongly correlated two-dimensional electrons in a silicon inversion layer,” Phys. Rev. B **67**, 205407 (2003)

[57] E. Tutuc, S. Melinte, E. P. De Poortere, M. Shayegan, and R. Winkler, “Role of finite layer thickness in spin polarization of GaAs two-dimensional electrons in strong parallel magnetic fields,” Phys. Rev. B **67**, 241309 (2003)

[58] Y.-W. Tan, J. Zhu, H. L. Stormer, L. N. Pfeiffer, K. W. Baldwin, and K. W. West, “Spin susceptibility of a two-dimensional electron system in GaAs towards the weak interaction region,” Phys. Rev. B **73**, 045334 (2006)

[59] O Gunawan, Y. P. Shkolnikov, K. Vakili, T. Gokmen, E. P. De Poortere, and M. Shayegan, “Valley susceptibility of an interacting two-dimensional electron system,” Phys. Rev. Lett. **97**, 186404 (2006)

[60] R. B. Dingle, “Some magnetic properties of metals. II. The influence of collisions on the magnetic behaviour of large systems,” Proc. R. Soc. A **211**, 517 (1952)

[61] A. Isihara and Smrcka L., “Density and magnetic field dependences of the conductivity of two-dimensional electron systems,” J. Phys. C **19**, 6777 (1986)

[62] Y. Adamov, I. V. Gornyi, and A. D. Mirlin, "Interaction effects on magneto-oscillations in a two-dimensional electron gas," Phys. Rev. B **73**, 045426 (2006)

[63] Medini Padmanabhan, T. Gokmen, and M. Shayegan, "Enhancement of valley susceptibility upon complete spin polarization," Phys. Rev. B **78**, 161301 (2008)

[64] T. Gokmen, Medini Padmanabhan, O. Gunawan, Y. P. Shkolnikov, K. Vakili, E. P. De Poortere, and M. Shayegan, "Parallel magnetic-field tuning of valley splitting in AlAs two-dimensional electrons," Phys. Rev. B **78**, 233306 (2008)

[65] O. Gunawan, T. Gokmen, K. Vakili, M. Padmanabhan, E. P. De Poortere, and M. Shayegan, "Spin-valley phase diagram of the two-dimensional metal-insulator transition," Nature Physics **3**, 388 (2007)

[66] E. P. De Poortere, E. Tutuc, S. J. Papadakis, and M. Shayegan, "Resistance spikes at transitions between quantum Hall ferromagnets," Science **290**, 1546 (2000)

[67] V. T. Dolgopolov and A. Gold, "The effect of parallel magnetic field on the Boltzmann conductivity and the Hall coefficient of a disordered two-dimensional Fermi liquid," JETP Lett. **71**, 27 (2000)

[68] Igor F. Herbut, "The effect of parallel magnetic field on the Boltzmann conductivity and the Hall coefficient of a disordered two-dimensional Fermi liquid," Phys. Rev. B **63**, 113102 (2001)

[69] Reza Asgari, T. Gokmen, B. Tanatar, Medini Padmanabhan, and M. Shayegan, "Effective mass suppression in a ferromagnetic two-dimensional electron liquid," Phys. Rev. B **79**, 235324 (2009)

[70] N. D. Drummond and R. J. Needs, "Quantum Monte Carlo calculation of the energy band and quasiparticle effective mass of the two-dimensional Fermi fluid," Phys. Rev. B **80**, 245104 (2009)

[71] M. Marchi, S. De Palo, S. Moroni, and Gaetano Senatore, "Correlation energy and spin susceptibility of a two-valley two-dimensional electron gas," Phys. Rev. B **80**, 035103 (2009)

[72] S. Das Sarma, E. H. Hwang, and Qi Li, "Valley-dependent many-body effects in two-dimensional semiconductors," Phys. Rev. B **80**, 121303 (2009)

[73] Charles S. Smith, "Piezoresistance effect in germanium and silicon," Phys. Rev. **94**, 42 (1954)

[74] Y. P. Shkolnikov, K. Vakili, E. P. De Poortere, and M. Shayegan, "Giant low-temperature piezoresistance effect in AlAs two-dimensional electrons," Appl. Phys. Lett. **85**, 3766 (2004)

[75] G. Dorda, I. Eisele, and H. Gesch, "Many-valley interactions in n-type silicon inversion layers," Phys. Rev. B **17**, 1785 (1978)

[76] Tsuneya Ando, Alan B. Fowler, and Frank Stern, "Electronic properties of two-dimensional systems," Rev. Mod. Phys. **54**, 437 (1982)

[77] N. C. Bishop, M. Padmanabhan, K. Vakili, Y. P. Shkolnikov, E. P. De Poortere, and M. Shayegan, "Valley polarization and susceptibility of composite fermions around a filling factor $\nu = 3/2$," Phys. Rev. Lett. **98**, 266404 (2007)

[78] Medini Padmanabhan, T. Gokmen, and M. Shayegan, “Density dependence of valley polarization energy for composite fermions,” Phys. Rev. B **80**, 035423 (2009)

[79] Medini Padmanabhan, *Composite Fermions with a Valley Degree of Freedom*, Ph.D. thesis, Princeton Univerity (2010)

[80] K. Vakili, Y. P. Shkolnikov, E. Tutuc, N. C. Bishop, E. P. De Poortere, and M. Shayegan, “Spin-dependent resistivity at transitions between integer quantum Hall states,” Phys. Rev. Lett. **94**, 176402 (2005)

[81] S. Dasgupta, S. Birner, C. Knaak, M. Bichler, A. Fontcuberta i Morral, G. Abstreiter, and M. Grayson, “Single-valley high-mobility (110) AlAs quantum wells with anisotropic mass,” Appl. Phys. Lett. **93**, 132102 (2008)

[82] Yasuhiro Tokura, “Two-dimensional electron transport with anisotropic scattering potentials,” Phys. Rev. B **58**, 7151 (1998)

[83] D. B. Balagurov and Yu. E. Lozovik, “Fermi surface of composite fermions and one-particle excitations at $\nu = 1/2$: Effect of band-mass anisotropy,” Phys. Rev. B **62**, 1481 (2000)

[84] S. Das Sarma and E. H. Hwang, “Low-density spin-polarized transport in two-dimensional semiconductor structures: Temperature-dependent magnetoresistance of Si-MOSFETs in an in-plane applied magnetic field,” Phys. Rev. B **72**, 205303 (2005)

[85] D. Simonian, S. V. Kravchenko, M. P. Sarachik, and V. M. Pudalov, "Magnetic field suppression of the conducting phase in two dimensions," Phys. Rev. Lett. **79**, 2304 (1997)

[86] E. Tutuc, E. P. De Poortere, S. J. Papadakis, and M. Shayegan, "In-plane magnetic field-induced spin polarization and transition to insulating behavior in two-dimensional hole systems," Phys. Rev. Lett. **86**, 2858 (2001)

[87] Oki Gunawan, *Ballistic Transport of AlAs Two-Dimensional Electrons*, Ph.D. thesis, Princeton Univerity (2007)